Università degli Studi di Napoli

FEDERICO II

DOTTORATO DI RICERCA IN

FISICA

32° Ciclo

Coordinatore: Prof. Salvatore Capozziello

Surface micro-structuring with ultrashort laser pulses

Settore Scientifico Disciplinare FIS/01

Dottorando
Elaheh Allahyari

Tutore
Prof. Salvatore Amoruso

Anni 2017/2020

Let us wish for the world peace!

Thesis introduction

The field of laser ablation was born with the invention of laser and it did not take long to be present in a variety of applications. The number of studies in this field grew very fast and it became increasingly more popular for manufacturing, chemical analysis, biology, medicine and so on. For many years the researchers explored the basic scientific understanding of the involved processes, meanwhile improving the instrumentations used and expanding the type of laser sources. With the advent of femtosecond (fs) pulse lasers the interests in laser-solid irradiation and ablation moved towards the use of ultrashort light pulses. Among the various phenomena involved in the interaction of ultrashort laser pulses and solid targets, the appearance of tiny reproducible surface patterns made this field much more popular and of interest also for technological and industrial applications.

This thesis explores the formation of fs laser induced periodic surface structures (LIPSS), their morphological features, possible ways to control them by exploiting the influence of experimental parameters (wavelength, polarization, energy, etc. of the laser pulses) and illustrates few examples of interest for possible applications. The surface morphologies were fabricated experimentally and analyzed by different imaging characterization techniques using as targets silicon and copper plates as well as gold thin film on a silicon substrate.

The thesis starts with a brief introductory chapter (Chapter 1) presenting the history of this innovative field of research, fs laser surface structuring. In addition, the essential models and theories along with experimental approaches used to realize the LIPSS and investigate their formation mechanisms are also summarized.

Chapter 2 illustrates the experimental setups and techniques used to carry out the experiments as well as methods for the measurement of physical parameters such as threshold fluence and spot size of the laser beams exploited in the course of the thesis, namely the Gaussian and the vector vortex beams. In particular, the standard Gaussian beam and the vector vortex more complex spatial intensity profiles are considered. The optical vector vortex beams are generated by using a beam converter based on a q-plate that modifies the original Gaussian beam. The complex spatial structure of the state of polarization and shape of these complex light fs laser beams when fired on

a silicon substrate, in air, allows producing very complex LIPSS patterns and shaped craters, as discussed in Chapter 3. The characteristics of such surfaces and the possibility to fabricate unconventional surfaces are discussed in detail.

So far, the formation mechanisms of LIPSS with sub-wavelength spatial period, named as ripples, are well established. Within the framework of this thesis, I tried to gain more information on the physical processes involved in the generation of LIPSS with supra-wavelength period, named grooves, on a silicon target. In Chapter 4, the influence of experimental parameters like laser pulse repetition rate, laser wavelength and ambient pressure on the surface structures with special emphasis on the grooves is addressed. The results evidence that the appearance of "grooves" is very much dependent on the experimental conditions and provide in some cases (namely, low ambient pressure and high repetition rate) information that can be useful to unveil certain mechanisms involved in supra-wavelength LIPSS formation.

Finally, in Chapter 5, I summarize results of experiments carried out on other materials, e.g. copper plate and gold thin film on silicon substrate, in the course of my thesis work. The main aim here is on the possibility of modifying the response of the material through laser processing. As a first example, texturing of copper surfaces, through scanning of the fs laser beam in ablation regime, brought up very interesting surface features composed of induced ripples and random oriented nanoparticles. The manufactured copper surfaces showed a degree of freedom in controlling the wetting response of the material. The second example concerns the possibility to fabricate two-dimensional THz metasurfaces by means of the mask-free fs laser surface structuring technique. The THz transmission response of the realized samples was measured in a collaborating laboratory and showed a good agreement with simulation addressing the possibility to design and realize such kind of THz optical components. Finally, preliminary experiments were carried out on CdZnTe, a direct and wide band gap ternary semiconductor alloy of possible interest for room-temperature detection of nuclear-radiation and infrared light and for which fs laser surface structuring has been scarcely investigated to date.

To conclude, the observations based on the experiments carried out in the course of this thesis provide valuable and interesting results for supporting this challenging field of research supporting a deeper understanding and a larger control on the laser induced surface structures.

Table of contents

1   Femtosecond laser surface structuring: literature review

Abstract – The history of birth of the original idea for the fabrication of surface structures by means of femtosecond laser pulses is briefly reviewed. The formation of laser induced periodic surface structures (LIPSS) is a common phenomenon that occurs on almost every solid surface after irradiation with polarized laser beams. Their classification and fundamental formation mechanisms are discussed here. Few techniques for their morphology control and some examples of technological applications are given as well.

1.1   Introduction

Laser-based surface micromachining is applied to a wide range of materials playing an important role in a number of applications in biomedicine, photonics, semiconductor processing, etc. [1]. Several direct writing techniques have been proposed [2] to fabricate surfaces including: conventional micromilling processes, electron and ion-beam lithographic methods, laser interference lithography, direct laser interference patterning, and laser ablation. Figure 1.1 shows the capability of various methods in terms of surface structure size and fabrication speed. These techniques gained attentions due to the advantages of being contactless and flexible methods, in addition to having a precise energy deposition [2].

The development of ultrashort laser pulses and their application in laser surface processing offer several advantages compared to the nanosecond ones due to a smaller heat affected zone (HAZ) that allows minimizing the damage, producing cleaner and more precise fine surfaces as well as improve the repeatability of the patterns [3–5]. The ability of femtosecond (fs) laser ablation in surface processing for technological applications was reported firstly by Pronko et al. [4]. In their experimental report an array of nanoholes using a Ti:Sa fs laser was fabricated and later sub-diffraction structures on transition metals were developed [4,6]. In particular, a fs laser beam with a Gaussian profile tightly focused onto the sample to spot size of ≈3 µm at a fluence slightly above the ablation threshold produced nanoholes with a diameter of ≈300 nm and a depth of ≈52 nm on a silver film substrate.
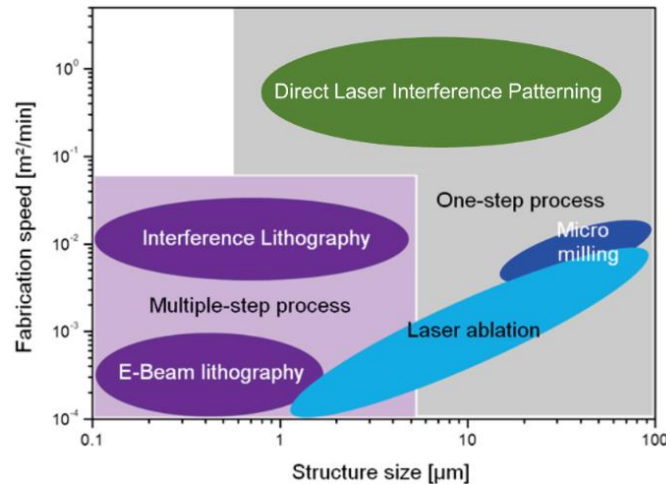
Figure 1.1 Possible direct write methods of surface fabrication as a function of structure size and fabrication speed (reprinted from [2] after permission from Journal of Laser Micro/ Nanoengineering)

The formation of self-organized fs laser induced periodic surface structures (LIPSS) is studied on a variety of materials such as metals [7], semiconductors [8], transparent materials [9], etc. The absorption of the laser pulse energy in the skin-depth layer of the material surface as a result of laser-matter interaction may lead to the formation of laser induced structures. This phenomenon is followed by thermal and possibly hydrodynamical or chemical effects [10,11]. The formation of surface structures is generally ascribed to the spatially modulated material removal (ablation) [11]. The basic physical phenomena responsible for fs laser ablation have been discussed in many papers and books as e.g. refs. [7,12–21], Generally, ablation of materials includes different mechanisms such as phase explosion (explosive boiling), evaporation, spallation, and fragmentation [10,22]. Theoretical approaches applied to fs laser ablation typically involve two-temperature model (TTM), molecular dynamics (MD) simulations, and hydrodynamic (MD) modeling [23,24].

In 1965, Birnbaum et al. for the first time discovered that the surface morphology can be controlled through formation of LIPSS by a Ruby laser [25]. He explained the observed structures as formed because of the diffraction effect and ablation occurring at the maximum of the electric field intensity [9,11]. In 1973, Emmony et al. proposed an interface mechanism in which the irradiated laser light, generated by a CO_2 laser, is scattered on the surface from dust or produced particles by occasional arc [26]. They assumed that the scattering centers formed on the surface generate wave

fronts propagating radially [26]. Further, they observed that the parallel damages have a spacing that depends on the laser wavelength in good agreement with the modified general surface scattering (GSS) model expressed as:

$$d = \lambda/(n_{\text{eff}} \pm \sin\theta) \tag{1}$$

where d is the period of gratings generated by travelling surface electromagnetic waves (SEW) or surface plasmon polaritons (SPPs), λ the wavelength of the irradiation light, $n_{\text{eff}} = \sqrt{\text{Re}[\varepsilon/(\varepsilon + 1)]}$ the real part of the effective refractive index of the air-material with the ε dielectric constant (or vacuum-material, etc.) and θ the angle of incidence of the light on the surface-active medium. It is noteworthy to highlight that SEW and SPPs were later introduced as the seeds of formation of surface structures by Keilmann et al. [27], Sipe et al. [28] and Guosheng et al. [29], independently.

The research group of Sipe demonstrated the first well-established theory of formation mechanism of surface structures within three communications during the years 1983 and 1984 [28,30,31]. In fact, the terminology of "laser induced periodic surface structure-LIPSS" was made known by this group. Their theory discussed that the inhomogeneous energy is deposited on a microscopically rough surface and introduced an "efficacy factor", η. [28]. Moreover, they found that the strong peak of electromagnetic field inducing the periodic surface patterns with specific orientation depends on angle of irradiation and polarization of the beam. Eventually, they proposed a model in which the interface of incident beam with a surface-scattered wave originates the LIPSSs. Figure 1.2 simply sketches how the LIPSSs are formed, neglecting all the feedback mechanisms involved in this figure, the theory is based on the interference of the incident laser beam with the rough surface (the authors labeled it as "selvedge region"). The magnitude of wave vector $\vec{\kappa}$ of the surface is dependent on the laser parameters; wavelength of the laser, angle of incidence and polarization direction of the laser light ($|\kappa| = (2\pi/\lambda)\sin\theta_{\text{inc}}$, the wave vector has a component, κ_i, parallel to the surface plane). Therefore, the refracted beam leads to inhomogeneous absorption of energy with the efficacy factor exhibiting sharp peaks on the surface at which the damage occurs [28].

In a second communication [31], they reported the experimental results on the formation of LIPSSs using a pulsed laser on different materials such as Ge, Si, Al and brass. In this communication, the

periodic patterns with orientation perpendicular to the polarization of incident laser beam were for the first time called as "ripples". Apart from this, they also observed type of periodic structures with the orientation parallel to the laser beam.
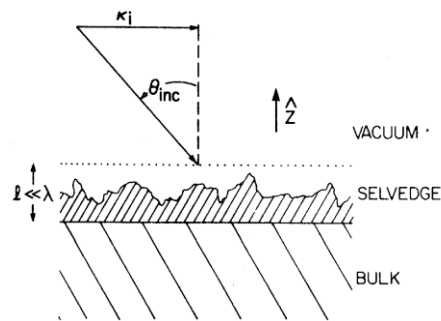
Figure 1.2 The geometry of light incident on a rough surface (reprinted from ref. [28])

Finally, in the third communication [30], they developed the model considering the role of feedback mechanisms on the growth of periodic structures. Additionally, they reported the ripple formation mechanisms at low fluences as resulting from isolated and molten stripes that re-solidify on the solid substrate of Ge, while, at high fluences, the structure results from freezing of capillary waves which are generated on the surface that the laser pulse has melted uniformly.

In this thesis, it is shown that effective surface material processing requires a deep knowledge for selecting the right laser parameters according to the target material [32,33]. Controlling the morphological features of surface structures not only is upon the substrate material [34–36], but also depends on laser parameters such as laser wavelength [37], laser beam polarization [38], spatial intensity profile of the laser pulse fluence [39–41] and number of incident laser pulses [42]. Moreover, redeposition of ablated particles, which depends on the background pressure, may also play a role [38,43].

1.2   Classifications of surface structures

Femtosecond laser assisted structured surfaces are gaining attention due to the simple single step ablation technique both from the point of view of the fundamental formation mechanisms and for their possible technological and industrial applications. Generally, structures with different types of morphology, from nanoscale to microscale, can be generated, which can be classified as [10]:

1) single or array of nano/micro holes [44–46]; Similarly to this, in this thesis we will report on the generation of arrays of holes on a gold thin film for THz applications [34]. (see Section 5.3).

2) nano/micro-scale texturing; this kind of patterns can cover the surface either in the form of ir/regular columnar structures [47,48] or as a carpet of parallel gratings commonly used in applications like modification of optical properties of a material surface in different wavelength ranges [49]. In section 5.2, a copper substrate is treated producing continues parallel scanned channels with the step between scanning lines of 50 µm. This section will show how roughness induced through direct fs laser ablation can influence the water wetting degree of the sample surface [36].

3) controlled irregular nanostructures like nanocavities, nanospheres, nanoprotrusions or nanowires [50,51].

4) nano/ micro-scale LIPSSs, which are the most actively studied surface structures. LIPSSs are important from the point of view of their formation mechanisms, for the capability of varying their characteristic features by simply changing laser irradiation parameters, and for the achievement of a large variety of morphologies that make them interesting in a wide range of applications [33,52]

LIPSS are generally divided in two categories according to the period of the structures (Λ) with respect to the laser wavelength (λ), [11]:

- high spatial frequency LIPSS (HSFL), or sometimes nanoripples: the "non-classical" type with $\Lambda < \lambda/2$ [53,54] (see Fig. 1.3 (a)).
- low spatial frequency LIPSS (LSFL): the classical type with near-wavelength period $\Lambda > \lambda/2$ (see Fig. 1.3 (b)).

LIPSSs can grow either perpendicular or parallel to the laser beam polarization. The structures with sub-wavelength period and orientation normal to the laser beam polarization are known as "ripples" ($\lambda/2 \leq \Lambda_{LSFL} \leq \lambda$), while those with supra-wavelength period and orientation along the laser beam polarization are often named as "grooves" [55]. Typically, LSFL are namely associated to ripples, but in a wider sense one could include also grooves in LSFL on the base of the relation between the LIPSS period and the light wavelength.
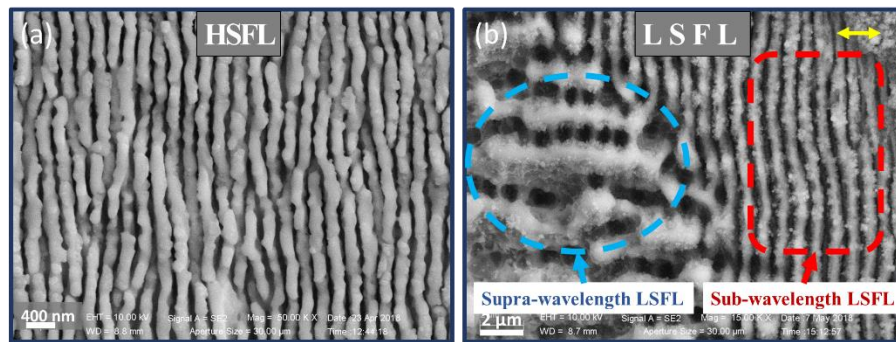
Figure 1.3 SEM images illustrating examples of two types of LIPSS: (a) surface structures formed on CdZnTe sample at an energy of $E = 55\ \mu J$ and $N = 1000$ (≈ 35 fs Ti:Sapphire laser at a central wavelength of 800 nm and a repetition rate of 10 Hz) [35]; (b) Surface texture on Si at $E = 10\ \mu J$ and $N = 200$ pulses (Yb:KGW ≈ 180 fs and λ=1030 nm, repetition rate 10 Hz). The double headed arrow shows the direction of the laser beam polarization for both panels.

In the next section, the formation mechanisms of LIPSS, in particular, LSFL will be discussed. One of the main objectives of the current thesis is to understand the underlying mechanism of LIPSS formation by varying the physical parameters and investigating the changes in the morphology of the structures.

1.3   Development of models on LIPSSs' formation mechanisms

At a suitable condition, usually near the ablation threshold, the irradiation of the solid material with fs laser pulses gives rise to generation of self-organized structures [56]. There are two

important physical processes soon after irradiation until permanent re-solidification of the ablated materials [10,57]. Firstly, the electron and lattice subsystems are thermally out of equilibrium. Second, the periodic structures are formed after the fs laser pulse finishes and the periodically modulated energy is deposited on the surface layer.

Until now, many studies have been reported regarding the formation mechanisms of surface structures [53,55,58–63] These models mainly dealt with two different points of view. Some authors considered non-resonant models like capillary wave excitation [64] and solid surface defects [65]. For example, in 2002, Reif et al. [53] proposed that the ripples present at the bottom of the ablated crater are due to a self-organization structure formation during the surface relaxation. Instead, the other proposals suggest to involve electromagnetic waves to explain properties of LIPSSs [66]. The group of Huang reported an interpulse feedback mechanism in which they considered that the ripples result from the initial direct SPPs-laser interference and the subsequent grating-assisted SPP-laser coupling [67].

To answer the open question about the origin of ripples, Dufft [61], Bonse [58] and co-workers suggested the carrier-dependent LIPSS formation by fs laser pulses within a theoretical approach combining the classical theory of Sipe et al. [28] and the Drude model (1900) linking optical and electrical properties of a material (laser-excited solid) with the behavior of its electrons or holes. Ripples generally appear using laser fluence slightly above the material ablation threshold and irradiation of few pulses. The authors in ref. [58] addressed formation of ripples as due to the excitation of SPPs that were observed on Si surface, even after single shot irradiance of the fs laser pulse.

The irradiation of a surface with fs laser pulse characterized by a high peak intensity (for example, semiconductor or dielectric) results in nonlinear interactions and changes in the optical properties of the material because of carrier excitation. The model of Sipe et al. was introduced as a linearized theory without any consideration of nonlinear effects. Considering the fs laser excitation process, the changes in refractive index of the material after irradiation should be modeled as a complex parameter. The complex refractive index $\tilde{n}^*$ is expressed by the following Equation:

$$\tilde{n}^* = \sqrt{\tilde{\varepsilon} + \Delta\tilde{\varepsilon}_{\text{Drude}} + \Delta\tilde{\varepsilon}_{\text{Kerr}}} \qquad (2)$$

which includes the complex dielectric function $\tilde{\varepsilon}$, the contribution by the carriers generated in conduction band ($\Delta\tilde{\varepsilon}_{\text{Drude}}$) and the Kerr effect ($\Delta\tilde{\varepsilon}_{\text{Kerr}}$) induced by the high intensity laser pulse and can be explained in the frame of Drude model [68]. The complex refractive index later would be the input of efficacy factor η in Sipe theory. The physical explanation behind the Sipe-Drude model is reported by the author interpreting that the high intensity fs laser pulses excite the electron in conduction band of a semiconductor, ZnO, through a multiphoton absorption mechanism. If the generated carrier density is high enough, the material transiently turns to a metallic state. The interference between the incident beam and the scattered surface electromagnetic wave generated by the SPPs makes the surface highly absorbing and coupling to the surface defect caused by the first fs laser pulse forms the ripples [58,61]. It is worthy to note that based on the same mechanism, amorphization (melting the surface without ablation) outside the annular crater can produce the periodic structures [33].

Bringing up more aspects of formation, Tsibidis et al. investigated the dynamics of ripple formation in a more extended theoretical framework [59]. This model shows the crater and subwavelength ripple formation based on a synergy of electron excitation and capillary wave solidification.

Increasing the number of laser pulses leads a surface patterned with other morphologies, namely grooves and spikes, with period greater than the laser wavelength. The above-mentioned models are able to describe in a rather good way the mechanisms underlying the formation of ripples, but they cannot provide the reason of supra-wavelength structures formation. Although these structures are very much controllable, their formation mechanisms are not yet clear enough; however, there are some reports regarding the underlying physical processes involved [55,69]. According to Tsibidis et al. [55], hydrodynamical effects are behind the formation of grooves. In this communication, the authors proposed a hybrid model to predict the grooves formation. This model is based on melt hydrodynamics complemented with electromagnetic interference effects to account for ripples, while Marangoni shear generated convection dominates the mechanism that leads to hydrothermal waves and eventually to microgrooves and microspikes formation [55].

Last but not least, it is important to summarize the feedback process in LIPSS formation. Considering a single shot, the feedback effects includes change of optical properties, surface wave

excitation, transient defect states (e.g. self-trapped excitons), nonlinear effects (e.g. second harmonic generation) or inhomogeneous absorption. Instead, firing a series of laser pulses onto the surface may cause topographical changes via ablation or hydrodynamic melt flows, structural changes (e.g. crystallin or amorphous state), chemical reactions with the ambient environment (e.g. oxidation), incubation effects (e.g. generation of permanent defect states, reduction of the damage thresholds) or self-organization promotion (e.g. surface erosion) [11].

Within the scope of the current thesis, one novel aspect is to extend the knowledge on understanding the real formation mechanisms of grooves; therefore, appropriate experiments are designed with variation of repetition rate, laser wavelength and ambient pressure using silicon as target material. Prior to these experiments, we present results obtained by using complex vortex light beams carrying orbital angular momentum (more details in Chapters 2 and 3) addressing the effect of the state of polarization of the laser beam on the morphologies of the LIPSS generated on the silicon surface. Finally, some examples of other experiments on fs laser surface processing on other materials, such as copper and gold thin film on a silicon substrate, carried out in the frame of the present thesis and potentially interesting for applications, are reported.

References

[1]   N.H. Rizvi, Femtosecond laser micromachining: current status and applications, Riken Rev. 50 (2003) 107–112.

[2]   A. Lasagni, Bringing the Direct Laser Interference Patterning Method to Industry: a One Tool-Complete Solution for Surface Functionalization, J Laser Micro/Nanoengineering. 10 (2015) 340–344. https://doi.org/10.2961/jlmn.2015.03.0019.

[3]   B.N. Chichkov, C. Momma, S. Nolte, F. Alvensleben, A. Tünnermann, Femtosecond, picosecond and nanosecond laser ablation of solids, Appl Phys A Mater Sci Process. 63 (1996) 109–115. https://doi.org/10.1007/BF01567637.

[4]   P.. Pronko, S.. Dutta, J. Squier, J.. Rudd, D. Du, G. Mourou, Machining of sub-micron holes using a femtosecond laser at 800 nm, Opt Commun. 114 (1995) 106–110. https://doi.org/10.1016/0030-4018(94)00585-I.

[5]   C. Momma, S. Nolte, B. Chichkov, von F. Alvensleben, A. Tuennermann, Precise laser ablation with ultra-short pulses, Appl Surf Sci. 109–110 (1997) 15–19. https://doi.org/10.1109/cleoe.1996.562552.

[6]   F. Korte, J. Serbin, J. Koch, A. Egbert, C. Fallnich, A. Ostendorf, B.N. Chichkov, Towards nanostructuring with femtosecond laser pulses, Appl Phys A. 77 (2003) 229–235. https://doi.org/10.1007/s00339-003-2110-z.

[7]   J. Reif, Basic Physics of Femtosecond Laser Ablation, in: M. A., O. P. (Eds.), Laser-Surface Interact New Mater Prod, springer, Berlin, Heidelberg, 2010: pp. 19–41. https://doi.org/10.1007/978-3-642-03307-0_2.

[8]   J. Bonse, S. Baudach, J. Krüger, W. Kautek, M. Lenzner, Femtosecond laser ablation of silicon-modification thresholds and morphology, Appl Phys A. 74 (2002) 19–25. https://doi.org/10.1007/s003390100893.

[9]   A. Papadopoulos, E. Skoulas, G.D. Tsibidis, E. Stratakis, Formation of periodic surface structures on dielectrics after irradiation with laser beams of spatially variant polarisation: a comparative study, Appl Phys A. 124 (2018) 146. https://doi.org/10.1007/s00339-018-1573-x.

[10]   A.Y. Vorobyev, C. Guo, Direct femtosecond laser surface nano/microstructuring and its applications, Laser Photon Rev. 7 (2012) 385–407. https://doi.org/10.1002/lpor.201200017.

[11]   J. Bonse, S. Hohm, S. V. Kirner, A. Rosenfeld, J. Kruger, Laser-Induced Periodic Surface Structures— A Scientific Evergreen, IEEE J Sel Top Quantum Electron. 23 (2017). https://doi.org/10.1109/JSTQE.2016.2614183.

[12]   E.G. Gamaly, A. V Rode, B. Luther-Davies, Ablation of solids by femtosecond lasers: ablation mechanism and ablation thresholds for metals and dielectrics, Phys Plasmas. 9 (2002).

[13]   S.K. Konidala, G. Kamala, S. Koralla, Laser Induced Breakdown Spectroscopy, Res J Pharm Technol. 9 (2016) 91. https://doi.org/10.5958/0974-360X.2016.00015.9.

[14]   S. Amoruso, R. Bruzzese, N. Spinelli, R. Velotta, Characterization of laser-ablation plasmas, J Phys B At Mol Opt Phys. 32 (1999) R131–R172. https://doi.org/10.1088/0953-4075/32/14/201.

[15]   S. Amoruso, G. Ausanio, A.C. Barone, R. Bruzzese, L. Gragnaniello, M. Vitiello, X. Wang, Ultrashort laser ablation of solid matter in vacuum: a comparison between the picosecond and femtosecond regimes, J Phys B At Mol Opt Phys. 38 (2005) L329–L338. https://doi.org/10.1088/0953-4075/38/20/L01.

[16]   E.G. Gamaly, Femtosecond Laser-Matter Interaction, Pan Stanford, Singapore, 2011. https://doi.org/10.1201/9789814267809.

[17]   C. Phipps, ed., Laser Ablation and its Applications, Springer US, Boston, MA, 2007. https://doi.org/10.1007/978-0-387-30453-3.

[18]   S. Nolte, C. Momma, H. Jacobs, A. Tünnermann, B.N. Chichkov, B. Wellegehausen, H. Welling, Ablation of metals by ultrashort laser pulses, J Opt Soc Am B. 14 (1997) 2716.

https://doi.org/10.1364/JOSAB.14.002716.

[19]   K.C. Phillips, H.H. Gandhi, E. Mazur, S.K. Sundaram, Ultrafast laser processing of materials: a review, Adv Opt Photonics. 7 (2015) 684. https://doi.org/10.1364/AOP.7.000684.

[20]   M.S. Brown, C.B. Arnold, Fundamentals of Laser-Material Interaction and Application to Multiscale Surface Modification, in: K. Ugioka, M. Meunier, A. Piqué (Eds.), Laser Precis Microfabr, Springer Berlin Heidelberg, Berlin, Heidelberg, 2010: pp. 91–120. https://doi.org/10.1007/978-3-642-10523-4.

[21]   D. Zhang, L. Guan, Laser Ablation, in: Compr Mater Process, Elsevier, 2014: pp. 125–169. https://doi.org/10.1016/B978-0-08-096532-1.00406-4.

[22]   A. Kiliyanamkandy, PhD thesis, Femtosecond Laser Ablation of Solid Targets using Gaussian and Vortex Beams, Università degli Studi di Napoli Federico II, 2015.

[23]   D. Perez, L.J. Lewis, Molecular-dynamics study of ablation of solids under femtosecond laser pulses, Phys Rev B. 67 (2003) 184102. https://doi.org/10.1103/PhysRevB.67.184102.

[24]   S.I. Anisimov, B.S. Luk'yanchuk, Selected problems of laser ablation theory, Uspekhi Fiz Nauk. 172 (2002) 301. https://doi.org/10.3367/UFNr.0172.200203b.0301.

[25]   M. Birnbaum, Semiconductor surface damage produced by Ruby lasers, J Appl Phys. 36 (1965) 3688–3689. https://doi.org/10.1063/1.1703071.

[26]   D.C. Emmony, R.P. Howson, L.J. Willis, Laser mirror damage in germanium at 10.6 μm, Appl Phys Lett. 23 (1973) 598–600. https://doi.org/10.1063/1.1654761.

[27]   F. Keilmann, Y.H. Bai, Periodic surface structures frozen into CO2 laser-melted quartz, Appl Phys A Solids Surfaces. 29 (1982) 9–18. https://doi.org/10.1007/BF00618110.

[28]   J.E. Sipe, J.F. Young, J.S. Preston, H.M. van Driel, Laser-induced periodic surface structure. I. Theory, Phys Rev 8. 27 (1983). https://doi.org/https://doi.org/10.1117/12.950633.

[29]   Z. Guosheng, P.M. Fauchet, A.E. Siegman, Growth of spontaneous periodic surface structures on solids during laser illumination, Phys Rev B. 26 (1982) 5366–5381. https://doi.org/10.1103/PhysRevB.26.5366.

[30]   J.F. Young, J.E. Sipe, H.M. Van Driel, Laser-induced periodic surface structure. III. Fluence regimes, the role of feedback, and details of the induced topography in germanium, Phys Rev B. 30 (1984) 2001–2015. https://doi.org/10.1103/PhysRevB.30.2001.

[31]   J.E. Sipe, J.F. Young, J.S. Preston, H.M. van Driel, Laser-induced periodic surface structure. I. Theory, Phys Rev B. 27 (1983) 1141–1154. https://doi.org/10.1103/PhysRevB.27.1141.

[32] F. Fraggelakis, G. Mincuzzi, J. Lopez, I. Manek-Hönninger, R. Kling, Texturing metal surface with MHz ultra-short laser pulses, Opt Express. 25 (2017) 18131. https://doi.org/10.1364/OE.25.018131.

[33] J. Bonse, M. Munz, H. Sturm, Structure formation on the surface of indium phosphide irradiated by femtosecond laser pulses Structure formation on the surface of indium phosphide irradiated by femtosecond laser pulses, J Appl Phys. 97 (2005) 013538. https://doi.org/10.1063/1.1827919.

[34] G.P. Papari, J.J.J. Nivas, C. Koral, E. Allahyari, S. Amoruso, Engineering of High Quality Factor THz Metasurfaces by Femtosecond Laser Ablation, Opt Laser Technol. Revision s (2020).

[35] J.J. Nivas, E. Allahyari, A. Vecchione, Q. Hao, S. Amoruso, X. Wang, Laser ablation and structuring of CdZnTe with femtosecond laser pulses, J Mater Sci Technol. Revision s (2020).

[36] E. Allahyari, J. JJ Nivas, S.L. Oscurato, M. Salvatore, G. Ausanio, A. Vecchione, R. Fittipaldi, P. Maddalena, R. Bruzzese, S. Amoruso, Laser surface texturing of copper and variation of the wetting response with the laser pulse fluence, Appl Surf Sci. 470 (2019) 817–824. https://doi.org/10.1016/j.apsusc.2018.11.202.

[37] E. Allahyari, J.J. Nivas, E. Skoulas, R. Bruzzese, G.D. Tsibidis, E. Stratakis, S. Amoruso, On the formation and features of the supra-wavelength grooves generated during femtosecond laser surface structuring of silicon, Manuscr under Prep to Submit J Appl Surf Sci. (2020).

[38] J. JJ Nivas, E. Allahyari, F. Gesuele, P. Maddalena, R. Fittipaldi, A. Vecchione, R. Bruzzese, S. Amoruso, Influence of ambient pressure on surface structures generated by ultrashort laser pulse irradiation, Appl Phys A. 124 (2018) 198. https://doi.org/10.1007/s00339-018-1621-6.

[39] J. JJ Nivas, E. Allahyari, F. Cardano, A. Rubano, R. Fittipaldi, A. Vecchione, D. Paparo, L. Marrucci, R. Bruzzese, S. Amoruso, Surface structures with unconventional patterns and shapes generated by femtosecond structured light fields, Sci Rep. 8 (2018) 13613. https://doi.org/10.1038/s41598-018-31768-w.

[40] E. Allahyari, J. JJ Nivas, F. Cardano, R. Bruzzese, R. Fittipaldi, L. Marrucci, D. Paparo, A. Rubano, A. Vecchione, S. Amoruso, Simple method for the characterization of intense Laguerre-Gauss vector vortex beams, Appl Phys Lett. 112 (2018) 211103. https://doi.org/10.1063/1.5027661.

[41] J. JJ Nivas, E. Allahyari, F. Cardano, A. Rubano, R. Fittipaldi, A. Vecchione, D. Paparo, L. Marrucci, R. Bruzzese, S. Amoruso, Vector vortex beams generated by q-plates as a versatile route to direct fs laser surface structuring, Appl Surf Sci. 471 (2019) 1028–1033. https://doi.org/10.1016/j.apsusc.2018.12.091.

[42] J. JJ Nivas, S. He, Z. Song, A. Rubano, A. Vecchione, D. Paparo, L. Marrucci, R. Bruzzese, S. Amoruso, Femtosecond laser surface structuring of silicon with Gaussian and optical vortex beams, Appl Surf Sci. 418 (2017) 565–571. https://doi.org/10.1016/j.apsusc.2016.10.162.

[43] J. JJ Nivas, F. Gesuele, E. Allahyari, S.L. Oscurato, R. Fittipaldi, A. Vecchione, R. Bruzzese, S. Amoruso, Effects of ambient air pressure on surface structures produced by ultrashort laser pulse irradiation, Opt Lett. 42 (2017) 2710. https://doi.org/10.1364/OL.42.002710.

[44] S.E. Kirkwood, M.T. Taschuk, Y.Y. Tsui, R. Fedosejevs, Nanomilling surfaces using near-threshold femtosecond laser pulses, J Phys Conf Ser. 59 (2007) 591–594. https://doi.org/10.1088/1742-6596/59/1/126.

[45] C.-Y. Zhang, J.-W. Yao, H.-Y. Liu, Q.-F. Dai, L.-J. Wu, S. Lan, V.A. Trofimov, T.M. Lysak, Colorizing silicon surface with regular nanohole arrays induced by femtosecond laser pulses, Opt Lett. 37 (2012) 1106. https://doi.org/10.1364/OL.37.001106.

[46] K. Vestentoft, P. Balling, Formation of an extended nanostructured metal surface by ultra-short laser pulses: single-pulse ablation in the high-fluence limit, Appl Phys A. 84 (2006) 207–213. https://doi.org/10.1007/s00339-006-3602-4.

[47] A.Y. Vorobyev, C. Guo, Femtosecond laser structuring of titanium implants, Appl Surf Sci. 253 (2007) 7272–7280. https://doi.org/10.1016/j.apsusc.2007.03.006.

[48] B.K. Nayak, M.C. Gupta, Self-organized micro/nano structures in metal surfaces by ultrafast laser irradiation, Opt Lasers Eng. 48 (2010) 940–949. https://doi.org/10.1016/j.optlaseng.2010.04.010.

[49] A.Y. Vorobyev, C. Guo, Femtosecond laser blackening of platinum, J Appl Phys. 104 (2008) 053516. https://doi.org/10.1063/1.2975989.

[50] Y. Dai, M. He, H. Bian, B. Lu, X. Yan, G. Ma, Femtosecond laser nanostructuring of silver film, Appl Phys A. 106 (2012) 567–574. https://doi.org/10.1007/s00339-011-6705-5.

[51] E. V Barmina, E. Stratakis, K. Fotakis, G.A. Shafeev, Generation of nanostructures on metals by laser ablation in liquids: new results, Quantum Electron. 40 (2010) 1012–1020. https://doi.org/10.1070/QE2010v040n11ABEH014444.

[52] J. Bonse, S. V. Kirner, S. Höhm, N. Epperlein, D. Spaltmann, A. Rosenfeld, J. Krüger, Applications of laser-induced periodic surface structures (LIPSS), in: U. Klotzbach, K. Washio, R. Kling (Eds.), Laser-Based Micro- Nanoprocessing XI, 2017: p. 100920N. https://doi.org/10.1117/12.2250919.

[53] J. Reif, F. Costache, M. Henyk, S. V. Pandelov, Ripples revisited: non-classical morphology at the bottom of femtosecond laser ablation craters in transparent dielectrics, Appl Surf Sci. 197–198 (2002) 891–895. https://doi.org/10.1016/S0169-4332(02)00450-6.

[54]   D. Zhang, K. Sugioka, Hierarchical microstructures with high spatial frequency laser induced periodic surface structures possessing different orientations created by femtosecond laser ablation of silicon in liquids, Opto-Electronic Adv. 2 (2019) 19000201–19000218. https://doi.org/10.29026/oea.2019.190002.

[55]   G.D. Tsibidis, C. Fotakis, E. Stratakis, From ripples to spikes: A hydrodynamical mechanism to interpret femtosecond laser-induced self-assembled structures, Phys Rev B. 92 (2015) 041405. https://doi.org/10.1103/PhysRevB.92.041405.

[56]   M. Garcia-Lechuga, D. Puerto, Y. Fuentes-Edfuf, J. Solis, J. Siegel, Ultrafast Moving-Spot Microscopy: Birth and Growth of Laser-Induced Periodic Surface Structures, ACS Photonics. 3 (2016) 1961–1967. https://doi.org/10.1021/acsphotonics.6b00514.

[57]   R. Fang, A. Vorobyev, C. Guo, Direct visualization of the complete evolution of femtosecond laser-induced surface structural dynamics of metals, Light Sci Appl. 6 (2017) e16256–e16256. https://doi.org/10.1038/lsa.2016.256.

[58]   J. Bonse, A. Rosenfeld, J. Krüger, On the role of surface plasmon polaritons in the formation of laser-induced periodic surface structures upon irradiation of silicon by femtosecond-laser pulses, J Appl Phys. 106 (2009) 104910. https://doi.org/10.1063/1.3261734.

[59]   G.D. Tsibidis, M. Barberoglou, P.A. Loukakos, E. Stratakis, C. Fotakis, Dynamics of ripple formation on silicon surfaces by ultrashort laser pulses in subablation conditions, Phys Rev B. 86 (2012) 115316. https://doi.org/10.1103/PhysRevB.86.115316.

[60]   J.P. Colombier, P. Combis, F. Bonneau, R. Le Harzic, E. Audouard, Hydrodynamic simulations of metal ablation by femtosecond laser irradiation, Phys Rev B. 71 (2005) 165406. https://doi.org/10.1103/PhysRevB.71.165406.

[61]   D. Dufft, A. Rosenfeld, S.K. Das, R. Grunwald, J. Bonse, Femtosecond laser-induced periodic surface structures revisited: A comparative study on ZnO, J Appl Phys. 105 (2009) 034908. https://doi.org/10.1063/1.3074106.

[62]   E.G. Gamaly, S. Juodkazis, K. Nishimura, H. Misawa, B. Luther-Davies, L. Hallo, P. Nicolai, V.T. Tikhonchuk, Laser-matter interaction in the bulk of a transparent solid: Confined microexplosion and void formation, Phys Rev B. 73 (2006) 214101. https://doi.org/10.1103/PhysRevB.73.214101.

[63]   Y. Fuentes-Edfuf, J.A. Sánchez-Gil, M. Garcia-Pardo, R. Serna, G.D. Tsibidis, V. Giannini, J. Solis, J. Siegel, Tuning the period of femtosecond laser induced surface structures in steel: From angled incidence to quill writing, Appl Surf Sci. 493 (2019) 948–955. https://doi.org/10.1016/j.apsusc.2019.07.106.

[64]   I. Ursu, I.N. Mihăilescu, A.M. Prokhorov, V.I. Konov, V.N. Tokarev, On the role of the periodical structures induced by powerful laser irradiation of metallic surfaces in the energy coupling process, Phys B+C. 132 (1985) 395–402. https://doi.org/10.1016/0378-4363(85)90126-3.

[65] V.I.Emel'yanov, D.V. Babak, Defect-strain instability and formation of periodic ablation structure on semiconductor surface under the action of ultrashort laser pulses, Proc SPIE"High-Power Laser Ablation III". 4065 (2000). https://doi.org/10.1117/12.407311.

[66] J.Z.P. Skolski, G.R.B.E. Römer, J. V. Obona, V. Ocelik, A.J. Huis in 't Veld, J.T.M. De Hosson, Laser-induced periodic surface structures: Fingerprints of light localization, Phys Rev B. 85 (2012) 075320. https://doi.org/10.1103/PhysRevB.85.075320.

[67] M. Huang, F. Zhao, Y. Cheng, N. Xu, Z. Xu, Origin of Laser-Induced Near-Subwavelength Ripples: Interference between Surface Plasmons and Incident Laser, ACS Nano. 3 (2009) 4062–4070. https://doi.org/10.1021/nn900654v.

[68] K. Sokolowski-Tinten, D. von der Linde, Generation of dense electron-hole plasmas in silicon, Phys Rev B. 61 (2000) 2643–2650. https://doi.org/10.1103/PhysRevB.61.2643.

[69] S. He, J.J. Nivas, A. Vecchione, M. Hu, S. Amoruso, On the generation of grooves on crystalline silicon irradiated by femtosecond laser pulses, Opt Express. 24 (2016) 3238. https://doi.org/10.1364/OE.24.003238.

2 Experimental Methods

Abstract – This chapter discusses the procedures illustrating the experimental setups (i.e. laser source, optical components and target materials) used in the target irradiation experiments and the characterization techniques exploited for their analysis as well as for the determination of the various features of the laser induced periodic surface structures.

2.1 Introduction

Fabrication of self-organized surface structures is based on the basic process of laser ablation. Direct femtosecond (fs) laser structuring takes place under certain conditions of the laser beam parameters such as wavelength, pulse duration, power level, beam size, beam polarization and repetition rate. These parameters can be optimized according to the substrate material and target environment [1]. The laser beam spatial intensity profile can significantly change the formation and features of the surface structures. In our experiments we generally used fs laser beams with a Gaussian intensity spatial profile. However, also the interesting capabilities of fs structured light beams for mask free surfaces and volume structuring [2] are highlighted in the present work by means of experiments with vector vortex laser beams. Such beams were obtained through a direct conversion of optical angular momentum by means of an optical component known as q-plate [3].

In this chapter, the experimental methods including the definition of beam parameters, instrumentation such as lasers, optics, targets, electronics and mechanical devices as well as the experimental techniques for the morphological characterizations are discussed in detail.

2.2 Laser beam spatial profile

The spatial profile of a laser beam is a characteristic defining the density distribution of the laser power in a plane perpendicular to the propagation direction as a function of distance from the source [4]. According to the shape of laser cavity, the intensity profile is different, however, most

of the lasers oscillate with a Gaussian distribution of electric field in which the spatial distribution of energy follows the non-uniform Gaussian function [5]. Figure 2.1 shows the spatial profiles of a Gaussian beam compared, as an example, to a non-Gaussian (vortex) one captured by a CCD camera in the focal plane [6]. The normalized fluence distributions of Gaussian and vortex beams along the beam diameter are plotted in Figure 2.1 (c). The laser fluence describes the energy delivered per unit surface, which is defined by unit of J/cm^2. The characteristics of the two fluence distributions will be illustrated hereafter. Panels (d-f) (see i.e. Figure 2.1) are few examples of irradiated craters on silicon surface.
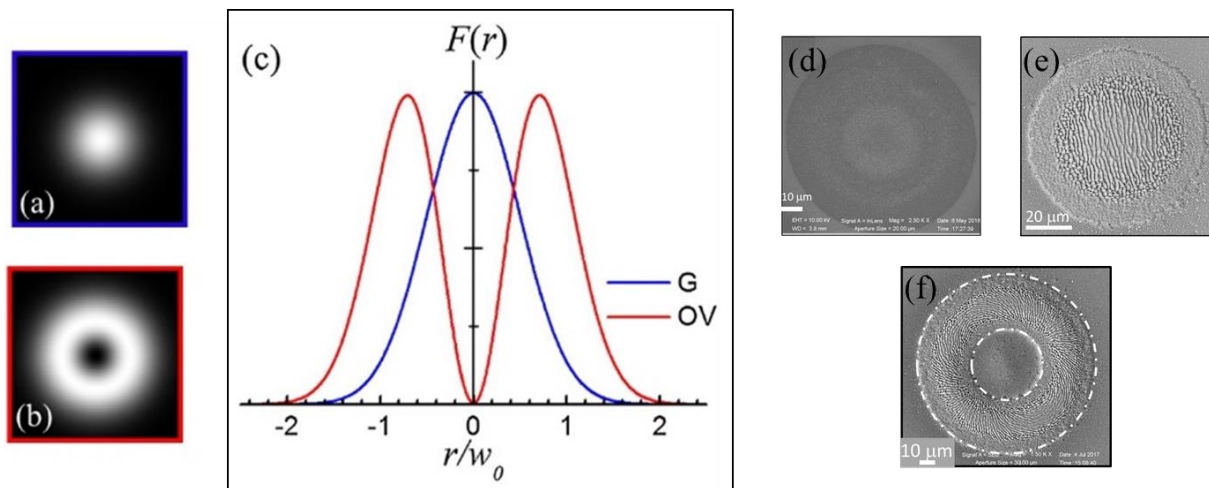

Figure 2.1 Spatial profiles captured by a CCD camera for (a) Gaussian and (b) Vortex beams. (c) Normalized spatial distribution of fluence (F) of the Gaussian and Vortex beams along the diameter as a function of the radius r, in units of beam waist w_0. (panels (a) – (c) are reprinted with permission from Ref. [6]) Panel (d) – (f) show the SEM images on silicon in air. (d) amorphous annulus of Gaussian beam (reprinted from Ref. [7]). (e) ablated crater irradiated by Gaussian beam. (f) ablated crater irradiated by vector vortex beam.

2.2.1   Gaussian beam

A Gaussian intensity profile is a fundamental transverse electromagnetic mode (TEM_{00}). For a Gaussian beam the spatial profile of the normalized pulse fluence $F(r)$ along the diameter of the beam, r, is given by:

$$F(r) = \frac{2E_0}{\pi w_0^2} \exp\left[\frac{-2r^2}{w_0^2}\right] \tag{1}$$

where E_0 is the beam energy and w_0 the waist of the fundamental Gaussian beam[6,8–10].

On the other hand, the maximum fluence value occurring within the Gaussian profile at $r = 0$, named as peak fluence F_p, is:

$$F_p = \frac{2E_0}{\pi w_0^2} \tag{2}$$

The spot size or beam waist of a Gaussian beam is the location along the beam axis where the intensity is $1/e^2$ of its own maximum value. A simple method to measure the spot size of the Gaussian beam is to use the fabricated circular craters produced by amorphization or ablation [5,6,11,12]. In fact, considering that the external radius of the amorphized region or the ablated crater are r_a and r_b and the corresponding values of the fluence is $F_{a,b} = \frac{2E_{a,b}}{\pi w_0^2}$ (threshold fluence), it is possible to draw out the following relations:

$$E_a = E_0 \exp[-2r_a^2/w_0^2] \tag{3}$$

$$E_b = E_0 \exp[-2r_b^2/w_0^2] \tag{4}$$

and get the functional dependence of r_a and r_b as:

$$r_a^2 = \frac{w_0^2}{2} \ln\left(\frac{E_0}{E_a}\right) \tag{5}$$

$$r_b^2 = \frac{w_0^2}{2} \ln\left(\frac{E_0}{E_b}\right) \tag{6}$$

From Equations (5-6), it is clear that the beam spot size can be derived by plotting r^2 versus energy E_0 and estimating the slope of the plot, which is equal to $\frac{w_0^2}{2}$ [5], through a fitting procedure. Then the parameters E_a and E_b can be associated to threshold energies for amorphization and ablation, respectively, and correspond the beam energy inducing the corresponding process at the beam center where the threshold fluence value $F_{a,b}$ occurs.

2.2.2 Vortex beam

The non-Gaussian structured beams are generated when the wavefront of the light beam rotates through the space. Light as an electromagnetic wave has angular momentum [13–15], which is related to twisting of the beam's wavefront around its propagation axis so that this displays a spiraling behavior (see e.g. Figure 2.2). As a consequence, the beam has a zero intensity at its center (see e.g. Figure 2.1(b)). There are two angular momentum of a light beam: spin angular momentum (SAM) and orbital angular momentum (OAM) that are associated to the motion imparted to a particle [16]. If the particle rotates around its own center, SAM is defined (Figure 2.2 (a)). While, OAM is related to rotation of particle around the beam axis (Figure 2.2 (b)) [17,18]. In other words, SAM is associated to optical polarization that can have two values $S_z = \sigma\hbar; \sigma = \pm 1$, $\hbar$ is the Planck constant and z is the axis of beam, $+$ and $-$ correspond to right and left circular polarization, respectively. Instead, OAM is associated with phase structure or optical wavefront of the beam. OAM of each particle can be $L_z = l\hbar$. The eigenvalue l is an integer and it defines the phase variation of an optical beam. Superposition of SAM and OAM gives total angular momentum (TAM), $J = j\hbar$, $j = l + m$ [17,19,20].
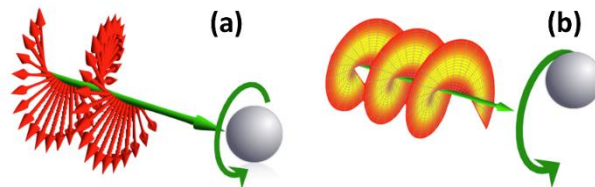
Figure 2.2 (a) SAM and (b) OAM interactions (reprinted after permission through communication with the holder of the original work [21])

Light beams with annular intensity patterns carrying optical phase singularities and non-zero OAM are called optical vortex beams (OVB) [22–25]. Optical phase singularity is defined by the helical phase front of OAM as $exp(il\varphi)$, where φ is the azimuthal angle around the optical axis z, and l is the OAM [26]. Recently fs optical vortex beams are gaining attentions in the micro-fabrication of various structures like cavities in glasses, single-layer graphene disks, polymer tubes, silicon conical structures [12].

The spatial fluence profile of a first order optical vortex beam ($l = \pm1$) along the diameter, which is shown as an example in Figure 2.1 (c), is described as[8]:

$$F(r) = \frac{2^2 E_0}{\pi w_0^4} r^2 \exp\left[\frac{-2r^2}{w_0^2}\right] \tag{7}$$

where r is the radial distance from the center, E_0 the beam energy and w_0 the waist of the fundamental Gaussian beam. The OV beam has a central singularity (Figure 2.1 (c)), and the peak fluence occurs at a distance $r_p = \frac{w_0}{\sqrt{2}}$ and is equal to:

$$F_{peak,OV} = 2e^{-1}\frac{E_0}{\pi w_0^2} \tag{8}$$

Equation (7) is an example of a more general equation describing the spatial distribution that can be expressed by using a Laguerre-Gauss mode fluence distribution for $p = 0$ and $l \neq 0$ described as [8,12]:

$$\frac{F_l(r)}{F_{l,peak}} = c_l\left(\frac{\sqrt{2}r}{w_0}\right)^{2l} e^{-\frac{2r^2}{w_0^2}} \tag{9}$$

where the normalized factor is equal to $c_l = \frac{e^l}{l^l}$ and w_0 is the beam waist. The fluence profile of the fundamental Gaussian beam of Equation (1) is recovered for $l = 0$. Moreover, the peak fluence is located at a radial distance from the propagation axis:

$$r_p = \sqrt{\frac{l}{2}}w_0 \tag{10}$$

and its value is given by:

$$F_{l,peak} = F_l(r_p) = \frac{2e^{-l}l^l}{l!}\frac{E}{\pi w_0^2} \tag{11}$$

Extending the method illustrated in the previous section, the value of beam spot size for the case of optical vortex or vector vortex beams can be directly estimated by measuring the internal and external radii of the annular ablated (amorphized, i.e Figure. 2.1 (c) – (f)) region, for which the pulse fluence equals the threshold fluence, i.e. $F_l(r_{in}) = F_l(r_{ex})$, then

$$\left(\frac{r_{in}}{w_0}\right)^{2l} e^{-\frac{2r_{in}^2}{w_0^2}} = \left(\frac{r_{ex}}{w_0}\right)^{2l} e^{-\frac{2r_{ex}^2}{w_0^2}} \tag{12}$$

The solution of the above equation provides a simple method to estimate the value of the optical vortex beam waist [12]:

$$w_0 = \sqrt{\frac{(r_{ex}^2 - r_{in}^2)}{l \ln\left(\frac{r_{ex}}{r_{in}}\right)}} \qquad (13)$$

There are several methods to generate a light beam carrying OAM, such as spiral phase plates, cylindrical lenses mode converters, computer generated fork holograms (CGH) displayed on spatial light modulators (SLMs), Dove prisms and q-plates [20,27]. In the current work, the q-plate converters are used to perform the experiments. A q-plate is an optical device in which a liquid crystal is enclosed between two parallel glass plates and it is characterized by a parameter, named topological charge of the vortex beam "q" ($l = 2q$) [3].

The generation of vortex beams using a q-plate was introduced by Marrucci et al. in 2006 for the first time [28,29] developing the q-plate by using liquid crystals technology. The q-plate fabrication process is explained by Slussarenko et al. [30] and will not be discussed here. This device is a thin optical element, working in transmission, electrically controllable as an optical retarder whose retardance δ is tunable by means of an external voltage [31]. Briefly, it acts as a spatially variant half-wave plate with a principal axis located at an angle α that rotates with the azimuthal angle φ [32] as:

$$\alpha = q\varphi + \alpha_0 \qquad (14)$$

where α_0 is the initial orientation angle of liquid crystals with the axis x at $\varphi = 0$ [33].

When a light beam travels through a q-plate, the topological charge $l = 2q$ transfers to the phase of the beam [14]. The q-plate retardance is adjustable through an external voltage provided by a signal generator, in our case a square wave with a frequency of 11 kHz was used [34]. Davis et al. [34] illustrated an experimental example of transmission of input intensity between two polarizers (the setup is shown in Figure 2.3) as a function of applied voltage to the q-plate. The results confirm that without any applied voltage, the q-plate acts like it is in the tuned condition with retardance of π. External voltage makes the liquid crystal to change the direction. Increasing the voltage results in decreasing the retardance. The efficiency of q-plate reaches maximum ($\approx$ 100%) when it is tuned to a half-wave retardance ($\varphi = \pi$). Therefore, we applied an appropriate

voltage to get a retardance of π in order to reliably drive the q-plate action and avoid any possible influence of other factors (e.g. temperature) that could affect its operation at a null voltage.

The fraction of SAM to OAM conversion (STOC) of the light passed through a q-plate with topological charge q and optical retardation δ is achievable by the following ratio [35]:

$$\cos \delta = \frac{P_{unconverted} - P_{converted}}{P_{unconverted} + P_{converted}} \tag{15}$$

where P is the output power measured by a power meter after the q-plate whose electrode is connected to the AC voltage.

To obtain the maximum efficiency, the q-plate must be in tuned condition ($\delta = \pi$) which has the maximum conversion of spin to orbital momentum. For this aim, we need to obtain the right value of applied external voltage (V_{pp}) which gives us the maximum power of converted part and the minimum power of unconverted part. A simple setup for alignment and optimization of q-plate is shown in Figure 2.3; if the quarter-wave plate QWP1 is at $+45°$ the power of the converted part is at its maximum and if the quarter-wave plate QWP2 is at $-45°$ the power of unconverted part is minimum.
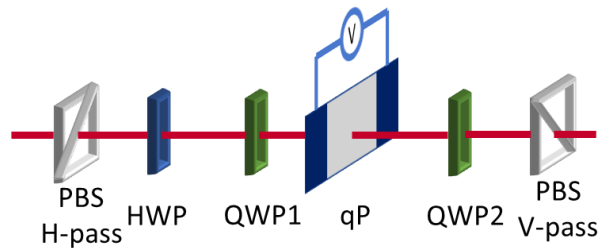
Figure 2.3 The experimental setup for optimization of the tuned condition of the q-plate. PBS stands for polarizing beam splitter – H-pass: horizontal pass, V-pass: vertical pass, HWP: half-wave plate, QWP: quarter-wave plate, qP: q-plate.

2.3   Experimental setup

In this thesis, the periodic surface structures are formed using fs laser pulses. The laser pulses for different experiments have been provided using various laser systems as listed in Table 2-1:

Table 2-1 Summary of the laser systems used for each experiment in this thesis

Thesis chapter		Purpose of experiment	Target material	Laser system
Chapter 3		Structuring with complex light	Silicon (100)	Ti:Sa laser system, ≈35 fs pulses at a central wavelength of 800 nm, repetition rate selected in the range of 10 – 1000 Hz
Chapter 4	Section 4.2	Effect of laser pulse repetition rate	Silicon (100)	Yb:KGW laser system providing ≈180 fs pulses at the wavelength of 1030 nm, the repetition rate was changed from 10 Hz – 200 kHz
	Section 4.3	Effect of laser wavelength	Silicon (100)	Yb:KGW laser source producing pulses of ≈170fs, 1 kHz repetition rate exploiting the fundamental 1026 nm central wavelength and its second harmonic of 513 nm
	Section 4.4	Effect of ambient pressure	Silicon (100)	Nd:glass laser system with pulse duration of ≈900 fs pulses at the wavelength of 1055 nm and the repetition rate of 33 Hz
Chapter 5	Section 5.2	Microscale texturing and wetting response	Copper foil	Ti:Sa laser system, ≈35 fs pulses at a central

			wavelength of 800 nm, repetition rate 1 kHz
Section 5.3	Laser surface patterning for THz-active metasurfaces	Gold thin film (180 nm) on silicon substrate (400 nm)	Ti:Sa laser system, ≈35 fs pulses at a central wavelength of 800 nm, repetition rate selected in the range of 10 – 1000 Hz
Section 5.4	Preliminary structuring on wide band-gap semicunductors	CdZnTe	Ti:Sa laser system, ≈35 fs pulses at a central wavelength of 800 nm, repetition rate 10 Hz

A general experimental setup to fabricate surface structures is sketched in Figure 2.4. To perform the experiments with Gaussian beam profiles, the q-plate was taken off from the set up.
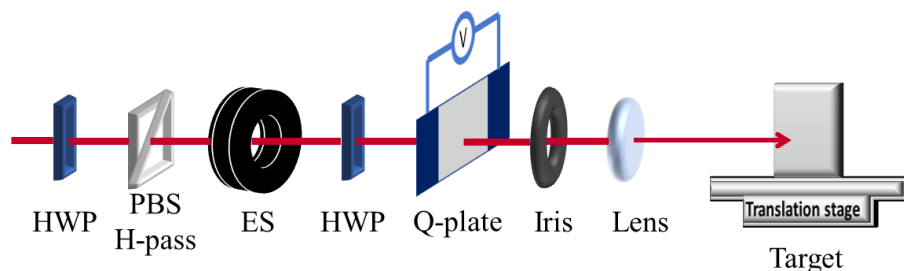

Figure 2.4 General experimental setup for producing LIPSS. The abbreviations stand for, HWP: half-wave plate, PBS: polarizing beam splitter – H-pass: horizontal pass, ES: Electromechanical shutter.

All the mentioned laser systems generate linearly polarized laser pulses with a Gaussian spatial profile. A combination of a half wave-plate and a polarizing beam splitter (PBS) was used to control the energy irradiated on the target. This energy was measured with an optical power meter. An electromechanical shutter provided the selection of the number of laser pulses (N) applied to

the same spot on the surface. The direction of polarization was controlled using a half wave-plate. A q-plate was used to set up the vortex beam. As for the optical vortex beam, the linear Gaussian input beam was converted to an output beam with radial, spiral and azimuthal state of polarization (SoP) according to the alignment of the half wave plate before the q-plate [6]. An iris was used as a spatial filter for selecting the central part of the beam. The beam was focused on the target by a plano-convex lens in order to have the proper spot size and round spot. The targets were placed on a XY translation stage which was controlled by a software. This stage was mounted inside a vacuum chamber for the experiments on the effects of variation of the ambient pressure.

In the previous chapter we already discussed on the formation of the periodic structure and mechanisms involved in the interaction of fs laser pulse with the target material [36]. Bonse et al. investigated that before ablation occurs, the physical process starts by absorption of the energy of the incident laser pulse by free carriers of the material [37]. The threshold fluence, i.e. the minimum value required to induce material removal, depends on the number of pulse N according to an incubation behavior given by [11]:

$$\phi_{th}(N) = \phi_{th}(1)\, N^{\xi-1} \tag{16}$$

where ϕ_{th} is the ablation fluence threshold at N number of pulses. $\phi_{th}(1)$ determines the threshold fluence for a single pulse. ξ is the incubation factor of the material. One can consider Equation 16 to quantify the degree of incubation [38]. The principal explanation of the incubation is not clear yet. However, this effect is initiated from an accumulation of energy on the target surface due to some reasons such as incomplete transferring of the laser energy to the ablated material [37–39].

The substrate can be selected among a variety of materials like semiconductors, metals, glasses, dielectrics, polymers, etc. For the experiments of this thesis, the targets were mainly intrinsic (resistivity > 200 Ω cm) single-crystalline silicon, Si (100) plates (dielectric constant $\varepsilon_{Si} = 13.64 + 0.048i$ at 800 nm). Silicon was selected because of its importance in industry and science. Other samples such as copper and gold thin film on silicon substrate were used as well in some experiments (see Table 2-1).

2.4   Characterization techniques

The characterization of the morphological features of the irradiated samples was carried out by resorting to different techniques including optical microscopy (OM), scanning electron microscopy (SEM), atomic force microscopy (AFM) and 2D or 3D profilometry, depending on any specific experiment. The analysis of the images was carried out using open source softwares as ImageJ [40] and Gwyddion [41]. In addition, further techniques such as Micro-Raman spectroscopy and Energy-dispersive X-ray spectroscopy (EDX) were available and used to collect more information on phase study and elemental analysis when appropriate (see Table 2-2).

Table 2-2 characterization techniques used in this thesis

Technique	Instrument	Observation	Specifications
surface analysis	Optical Microscopy	Low resolution (up to 50x) imaging	Zeiss Axio Scope A1
	Field Emission Scanning Electron Microscope (FESEM)	Morphology	Zeiss ΣIGMA Images are acquired by secondary electrons (SE) with an Everhart-Thornley (ET-SE) type detector.
	Atomic Force Microscopy (AFM)	Morphology and topography	Alpha300 RS (WITec, Ulm, Germany)
			NOVA AFM
	Profilometry	Topography	Dektak XT
spectroscopy	Micro Raman	Chemical composition	Alpha300 RS (WITec, Ulm, Germany)

	Energy-dispersive X-ray spectroscopy (EDX)	Phase study	OXFORD INCA Energy 300
	Time Domain Spectroscopy (TDS)	THz response	Tera-K15, Menlo Systems
Surface-wetting		Water contact angle (CA)	Homemade setup [42]

References

[1] Y. Fuentes-Edfuf, J.A. Sánchez-Gil, M. Garcia-Pardo, R. Serna, G.D. Tsibidis, V. Giannini, J. Solis, J. Siegel, Tuning the period of femtosecond laser induced surface structures in steel: From angled incidence to quill writing, Appl Surf Sci. 493 (2019) 948–955. https://doi.org/10.1016/j.apsusc.2019.07.106.

[2] J. JJ Nivas, E. Allahyari, F. Cardano, A. Rubano, R. Fittipaldi, A. Vecchione, D. Paparo, L. Marrucci, R. Bruzzese, S. Amoruso, Vector vortex beams generated by q-plates as a versatile route to direct fs laser surface structuring, Appl Surf Sci. 471 (2019) 1028–1033. https://doi.org/10.1016/j.apsusc.2018.12.091.

[3] L. Marrucci, The q-plate and its future, J Nanophotonics. 7 (2013) 078598. https://doi.org/10.1117/1.JNP.7.078598.

[4] G. Herziger, H. Weber, R. Poprawe, Laser Systems, Part 1, Springer Berlin Heidelberg, Berlin, Heidelberg, 2007. https://doi.org/10.1007/978-3-540-44821-1.

[5] J.M. Liu, Simple technique for measurements of pulsed Gaussian-beam spot sizes, Opt Lett. 7 (1982) 196. https://doi.org/10.1364/OL.7.000196.

[6] J. JJ Nivas, S. He, Z. Song, A. Rubano, A. Vecchione, D. Paparo, L. Marrucci, R. Bruzzese, S. Amoruso, Femtosecond laser surface structuring of silicon with Gaussian and optical vortex beams, Appl Surf Sci. 418 (2017) 565–571. https://doi.org/10.1016/j.apsusc.2016.10.162.

[7] F. Gesuele, J.J.J. Nivas, R. Fittipaldi, C. Altucci, R. Bruzzese, P. Maddalena, S. Amoruso, Multi-imaging analysis of nascent surface structures generated during femtosecond laser irradiation of silicon in high vacuum, Appl Phys A Mater Sci Process. 124 (2018). https://doi.org/10.1007/s00339-018-1633-2.

[8] Q. Zhan, Cylindrical vector beams: from mathematical concepts to applications, Adv Opt

Photonics. 1 (2009) 1. https://doi.org/10.1364/AOP.1.000001.

[9]   F.M. Dickey, ed., Laser Beam Shaping, CRC Press, 2018. https://doi.org/10.1201/b17140.

[10]   B.E.A. Saleh, M.C. Teich, Fundamentals of Photonics, John Wiley & Sons, Inc., New York, USA, 1991. https://doi.org/10.1002/0471213748.

[11]   J. Bonse, J.M. Wrobel, J. Krüger, W. Kautek, Ultrashort-pulse laser ablation of indium phosphide in air, Appl Phys A Mater Sci Process. 72 (2001) 89–94. https://doi.org/10.1007/s003390000596.

[12]   E. Allahyari, J. JJ Nivas, F. Cardano, R. Bruzzese, R. Fittipaldi, L. Marrucci, D. Paparo, A. Rubano, A. Vecchione, S. Amoruso, Simple method for the characterization of intense Laguerre-Gauss vector vortex beams, Appl Phys Lett. 112 (2018) 211103. https://doi.org/10.1063/1.5027661.

[13]   K.K. Anoop, A. Rubano, R. Fittipaldi, X. Wang, D. Paparo, A. Vecchione, L. Marrucci, R. Bruzzese, S. Amoruso, Femtosecond laser surface structuring of silicon using optical vortex beams generated by a q-plate, Appl Phys Lett. 104 (2014) 241604. https://doi.org/10.1063/1.4884116.

[14]   E. Karimi, B. Piccirillo, E. Nagali, L. Marrucci, E. Santamato, Efficient generation and sorting of orbital angular momentum eigenmodes of light by thermally tuned q-plates, Appl Phys Lett. 94 (2009) 231124. https://doi.org/10.1063/1.3154549.

[15]   I.G. Mariyenko, J. Strohaber, C.J.G.J. Uiterwaal, Creation of optical vortices in femtosecond pulses, Opt Express. 13 (2005) 7599. https://doi.org/10.1364/OPEX.13.007599.

[16]   J.P. Torres, L. Torner, eds., Twisted Photons, Wiley-VCH Verlag GmbH & Co. KGaA, Weinheim, Germany, 2011. https://doi.org/10.1002/9783527635368.

[17]   L. Marrucci, E. Karimi, S. Slussarenko, B. Piccirillo, E. Santamato, E. Nagali, F. Sciarrino, Spin-to-orbital conversion of the angular momentum of light and its classical and quantum applications, J Opt. 13 (2011) 064001. https://doi.org/10.1088/2040-8978/13/6/064001.

[18]   E. Karimi, B. Piccirillo, L. Marrucci, E. Santamato, Light propagation in a birefringent plate with topological charge, Opt Lett. 34 (2009) 1225. https://doi.org/10.1364/OL.34.001225.

[19]   J. Leach, J. Courtial, K. Skeldon, S.M. Barnett, S. Franke-Arnold, M.J. Padgett, Interferometric Methods to Measure Orbital and Spin, or the Total Angular Momentum of a Single Photon, Phys Rev Lett. 92 (2004) 013601. https://doi.org/10.1103/PhysRevLett.92.013601.

[20]   S. Slussarenko, A. Murauski, T. Du, V. Chigrinov, L. Marrucci, E. Santamato, Tunable liquid crystal q-plates with arbitrary topological charge, Opt Express. 19 (2011) 4085. https://doi.org/10.1364/OE.19.004085.

[21]   E. Karimi, light beam interacting with small particle for two different cases, En.Wikipedia.Org. (2011). https://commons.wikimedia.org/wiki/File:Sam-oam-interaction.png.

[22]   E. Brasselet, N. Murazawa, H. Misawa, S. Juodkazis, Optical Vortices from Liquid Crystal Droplets, Phys Rev Lett. 103 (2009) 103903. https://doi.org/10.1103/PhysRevLett.103.103903.

[23]   S.H. Tao, X.-C. Yuan, J. Lin, X. Peng, H.B. Niu, Fractional optical vortex beam induced rotation of particles, Opt Express. 13 (2005) 7726. https://doi.org/10.1364/OPEX.13.007726.

[24]   F. Cardano, E. Karimi, S. Slussarenko, L. Marrucci, C. de Lisio, E. Santamato, Polarization pattern of vector vortex beams generated by q-plates with different topological charges, Appl Opt. 51 (2012) C1. https://doi.org/10.1364/AO.51.0000C1.

[25]   F. Cardano, E. Karimi, L. Marrucci, C. de Lisio, E. Santamato, Generation and dynamics of optical beams with polarization singularities, Opt Express. 21 (2013) 8815. https://doi.org/10.1364/OE.21.008815.

[26]   P. Senthilkumaran, S. Sato, J. Masajada, Singular Optics, Int J Opt. 2012 (2012) 1–2. https://doi.org/10.1155/2012/741693.

[27]   B. Piccirillo, S. Slussarenko, L. Marrucci, E. Santamato, The orbital angular momentum of light: Genesis and evolution of the concept and of the associated photonic technology, Riv Del Nuovo Cim. 36 (2013) 501–555. https://doi.org/10.1393/ncr/i2013-10094-y.

[28]   L. Marrucci, C. Manzo, D. Paparo, Pancharatnam-Berry phase optical elements for wave front shaping in the visible domain: Switchable helical mode generation, Appl Phys Lett. 88 (2006) 221102. https://doi.org/10.1063/1.2207993.

[29]   L. Marrucci, C. Manzo, D. Paparo, Optical Spin-to-Orbital Angular Momentum Conversion in Inhomogeneous Anisotropic Media, Phys Rev Lett. 96 (2006) 163905. https://doi.org/10.1103/PhysRevLett.96.163905.

[30]   S. Slussarenko, B. Piccirillo, V. Chigrinov, L. Marrucci, E. Santamato, Liquid crystal spatial-mode converters for the orbital angular momentum of light, J Opt (United Kingdom). 15 (2013). https://doi.org/10.1088/2040-8978/15/2/025406.

[31]   M.M. Sánchez-López, J.A. Davis, N. Hashimoto, I. Moreno, E. Hurtado, K. Badham, A. Tanabe, S.W. Delaney, Performance of a q-plate tunable retarder in reflection for the switchable generation of both first- and second-order vector beams, Opt Lett. 41 (2016) 13. https://doi.org/10.1364/OL.41.000013.

[32]   K. Badham, I. Moreno, M.M. Sánchez-López, J.A. Davis, N. Hashimoto, M. Kurihara, J. Albero, D.M. Cottrell, Parallel generation of multiple first-order vector beams with a polarization grating and a q-plate device, Jpn J Appl Phys. 55 (2016) 122202. https://doi.org/10.7567/JJAP.55.122202.

[33]   J. JJ Nivas, E. Allahyari, F. Cardano, A. Rubano, R. Fittipaldi, A. Vecchione, D. Paparo, L. Marrucci, R. Bruzzese, S. Amoruso, Surface structures with unconventional patterns and shapes generated by femtosecond structured light fields, Sci Rep. 8 (2018) 13613. https://doi.org/10.1038/s41598-018-31768-w.

[34]   J.A. Davis, N. Hashimoto, M. Kurihara, E. Hurtado, M. Pierce, M.M. Sánchez-López, K. Badham, I. Moreno, Analysis of a segmented q-plate tunable retarder for the generation of first-order vector beams, Appl Opt. 54 (2015) 9583. https://doi.org/10.1364/AO.54.009583.

[35]   B. Piccirillo, V. D'Ambrosio, S. Slussarenko, L. Marrucci, E. Santamato, Photon spin-to-orbital angular momentum conversion via an electrically tunable q-plate, Appl Phys Lett. 97 (2010) 241104. https://doi.org/10.1063/1.3527083.

[36]   A.Y. Vorobyev, C. Guo, Direct femtosecond laser surface nano/microstructuring and its applications, Laser Photon Rev. 7 (2012) 385–407. https://doi.org/10.1002/lpor.201200017.

[37]   J. Bonse, S. Baudach, J. Krüger, W. Kautek, M. Lenzner, Femtosecond laser ablation of silicon–modification thresholds and morphology, Appl Phys A. 74 (2002) 19–25. https://doi.org/10.1007/s003390100893.

[38]   J. Byskov-Nielsen, J.-M. Savolainen, M.S. Christensen, P. Balling, Ultra-short pulse laser ablation of metals: threshold fluence, incubation coefficient and ablation rates, Appl Phys A. 101 (2010) 97–101. https://doi.org/10.1007/s00339-010-5766-1.

[39]   S. Reich, A. Letzel, B. Gökce, A. Menzel, S. Barcikowski, A. Plech, Incubation Effect of Pre-Irradiation on Bubble Formation and Ablation in Laser Ablation in Liquids, ChemPhysChem. 20 (2019) 1036–1043. https://doi.org/10.1002/cphc.201900075.

[40]   ImageJ: image processing program, (n.d.). https://imagej.nih.gov/ij/.

[41]   Gwyddion: Scanning probe microscopy data visualisation and analysis, (n.d.). http://gwyddion.net/.

[42]   S.L. Oscurato, F. Borbone, P. Maddalena, A. Ambrosio, Light-Driven Wettability Tailoring of Azopolymer Surfaces with Reconfigured Three-Dimensional Posts, ACS Appl Mater Interfaces. 9 (2017) 30133–30142. https://doi.org/10.1021/acsami.7b08025.

3   Structuring with Optical Vector Vortex beams

Abstract – This chapter is dedicated to illustrating surface structuring with optical vector vortex beams with the aim of both gaining further understanding on the formation mechanisms of sub- and supra-wavelength structures and generating unconventional patterns and structures. By using q-plates with different topological charges various vector vortex beams are generated and their characteristics are tuned by controlling the q-plate optical retardation. This chapter shows the advantage and ability of using the state of polarization of vector vortex laser beam as a viable route to the production of complex structures. Moreover, step scan fabrication process for the structuring of large areas with sophisticated patterns is also presented.

3.1   Introduction

In the last decades, the number of research fields trying benefits from the application of structured light beams with tailored intensity, polarization or phase is continuously increasing (e.g., microscopy, quantum optics and information, photonics, optical trapping, data communication, etc.) [1,2]. Manipulation and fabrication of fs LIPSS using complex beams with spatially inhomogeneous state of polarization (SoP) have been already proposed [3–6]. Due to different applications in optics, photonics, materials surface processing, etc. of these types of morphologies spatially shaped vortex beams are increasingly getting attention in laser fabrication of different materials, such as metals, semiconductors, 2D materials, etc. [7,8]. Furthermore, since the orientation of the fine structures follows a direct relation with the laser polarization, this strategy allows one also to get a more direct access to characterization of intense optical vector vortex (VV) beams through the analysis of the produced surface structures [9].

Direct nanostructuring with complex fs optical VV beams on silicon by means of a q-plate was investigated by Anoop et al. [3]. This study mainly focused on controlling the periodic regular structures developed by a fs optical VV beam by varying parameters like number of laser pulses N and laser beam energy E_0 [3,10]. In the letter [3], a VV beam with a topological charge $q =$

$+1/2$, carrying an OAM $l = \pm1$, displaying an intensity distribution with a doughnut shape was used. Successively, JJ Nivas et al. published SEM images of the ablated spots showing that ripples and grooves are directly linked to the polarization of the various VV beam that can be generated by a q-plate with $q = +1/2$ (see Figure 3.1) [10]. These experimental findings demonstrated that VV beams allow selecting suitable patterns without any use of beam shaping or holography for specific material processing applications. The evolution of the surface morphology as a function of N indicates a clear cumulative effect also for the VV beams.
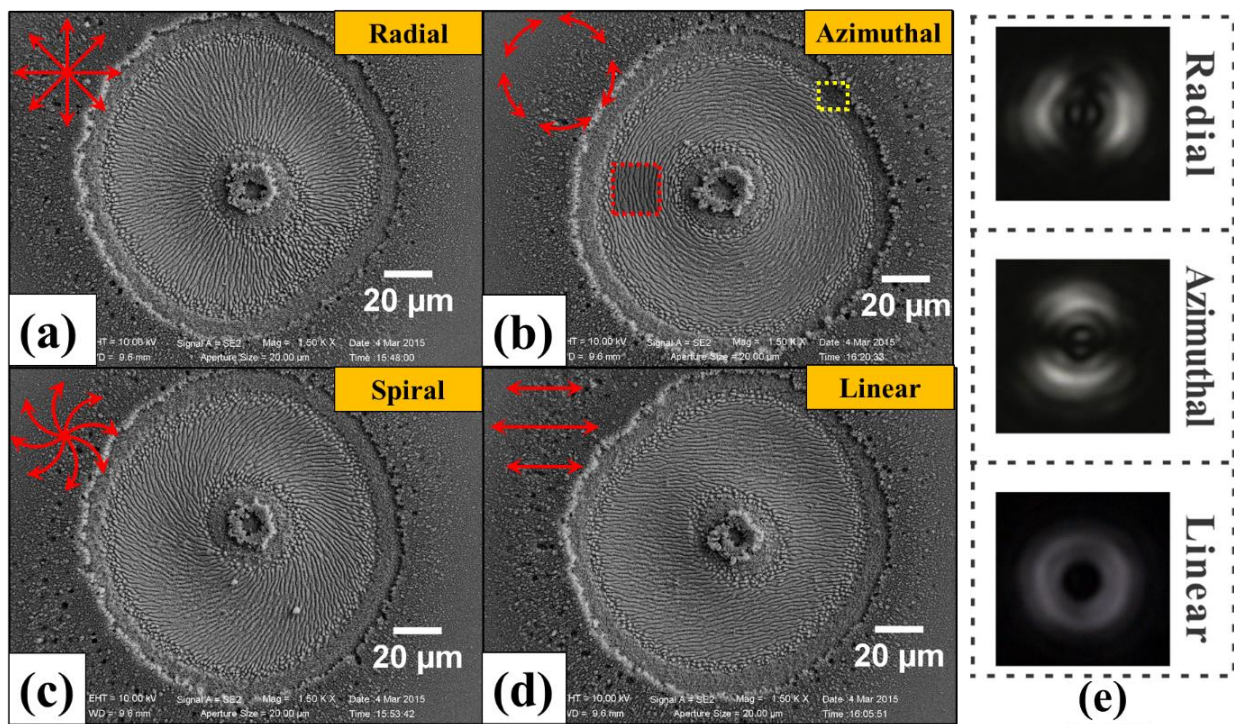

Figure 3.1 Examples of the surface structures developed on a silicon target after an irradiation sequence of $N = 100$ pulses at an energy $E_0 = 48$ μJ with different SoP: (a) radial, (b) azimuthal, (c) spiral and (d) linear. (e) Optical patterns registered after a horizontally-oriented polarizing filter showing the radial, azimuthal and linear SoP of the VV beam. (reproduced from Ref. [10])

So far, in the literature, the use of VV beams generated by the q-plates for direct surface structuring was mainly focused on experiments based on q-plates with topological charge of $+1/2$ [3,7,9–12]. In this thesis, an experimental characterization of the complex surfaces that can be fabricated

by using q-plates with higher order topological charges has been accomplished, as illustrated in the following sections [13,14].

3.2 Applications of optical vector vortex beams with different topological charges

Higher order q-plates are used to generate VV beams from an input fs Gaussian beam. Hence laser ablation of silicon is induced by these structured beams forming complex surface structures due to the complex intensity and polarization distributions associated to the higher topological charges.

In this chapter, the fs laser pulses were provided by a Ti:Sa laser system (800 nm wavelength, ≈35 fs pulse duration, 10 Hz rep. rate). Different optical VV beams were generated by using q-plates with $q = 1, 3/2, 2, 5/2$, with an initial angle $\alpha_0 = -\pi/6$. An external signal generator providing a square-wave at 11 kHz and a variable voltage V_{pp} (peak to peak) was used to tune the optical retardation δ of the q-plate. The target was a crystalline silicon target (intrinsic resistivity > 200 Ωcm), (1 0 0)) and the laser beam was focused onto the Si sample, in air, by a plano-convex lens with a focal length of 75 mm. Furthermore, the simulated polarization and intensity distributions of the VV beams are computed and showed in this chapter.

3.3 Optical retardation δ

Q-plate is a birefringent wave plate based on liquid crystal technology. The local optical axes of the liquid crystal molecules are distributed inhomogeneously in the transvers $x - y$ plane [15]. The orientation of the liquid crystal molecular director can be changed through an external electric field, therefore, δ is uniform point by point along the plate with homogenous thickness [16]. The variation of the peak-to-peak voltage intensity controls the efficiency of the spin-to-orbital angular momentum conversion by means of the optical retardation δ of the q-plate according Equation 15 of Chapter 2 [17].

The q-plate transforms an input light field described by the Jones vector $\psi_{in}(x, y)$ into an emerging light field $\psi_{out}(x, y)$ given by:

$$\psi_{out}(x,y) = \left[cos\left(\frac{\delta}{2}\right) I - i\, sin\left(\frac{\delta}{2}\right) M_q(\alpha) \right] \psi_{in}(x,y) \tag{1}$$

where I is the identity matrix, and $M_q(\alpha)$ is the Jones matrix of a half-wave plate whose axis forms an angle α with respect to the reference x-axis. Equation (1) shows that the optical retardation, δ, acts as a tuning parameter between two limiting states. A "tuned" condition that refers to generation of singular vortex beams with uniform polarization ellipticity and a central vortex singularity with zero intensity [18]. The q-plate is called "untuned" when the field at the exit plane of the q-plate has achieved a partial spin-to-orbital conversion [19]. For the un-tuned condition, $\delta = 2\pi$, the q-plate behaves as a transparent medium leaving unchanged the input beam. Some examples of the q-plate configuration for different optical retardations δ and their corresponding spatial intensity profiles registered by a CCD camera after the q-plate with topological charge of $+1/2$ are shown by JJ Nivas et al. [9]. In the following, we study the features of surface structures induced by focusing the VV beam generated by q-plates, in different tuned and untuned conditions, onto the silicon target. The surface patterns are characterized by a field-emission scanning electron microscope (SEM).

3.3.1   Surface structures generated by optimally tuned q-plate

Irradiating the q-plate with a linearly polarized input beam allows generating a superposition of left and right circularly polarized helical beams carrying opposite values of orbital angular momentum (OAM), $\ell = \pm 2q$. At the optimal tuning, $\delta = \pi$ (or any odd multiple of π), the q-plate converts the input beam into a more complex optical beam capable of carrying an OAM. We performed the present experiment to confirm an important degree of freedom of producing peculiar surface patterns with complex distribution of sub- and supra-wavelength periods (i.e. ripples and grooves) which are achievable by shining a VV beam with complex intensity and SoP spatial distribution onto a target.

Since our laser system delivers a Gaussian beam with horizontal polarization, the input beam in Equation 1 should be considered as $\psi_{in}(x,y) = G_H(x,y)$. Accordingly, for the tuned condition $\delta = \pi$ the electric field of the output VV beam is $V_q(x,y) = M_q(\alpha)G_H(x,y)$. The ablated craters in this case follow the ring-shaped intensity distribution with a central singularity of the VV beam

(Figure 3.2). A general solution of light field for the output beam after the q-plate with untuned optical retardations δ is a superposition state of the Gaussian G_H and the VV beam V_q given by:

$$\psi_{out}(x,y) = cos\left(\frac{\delta}{2}\right)G_H(x,y) - i\,sin\left(\frac{\delta}{2}\right)V_q(x,y) \tag{2}$$

The experimental and theoretical investigations of voltage tuning of the q-plate with topological charge $q = +1/2$ is addressed in Ref. [9]. Here we deal with higher q values.
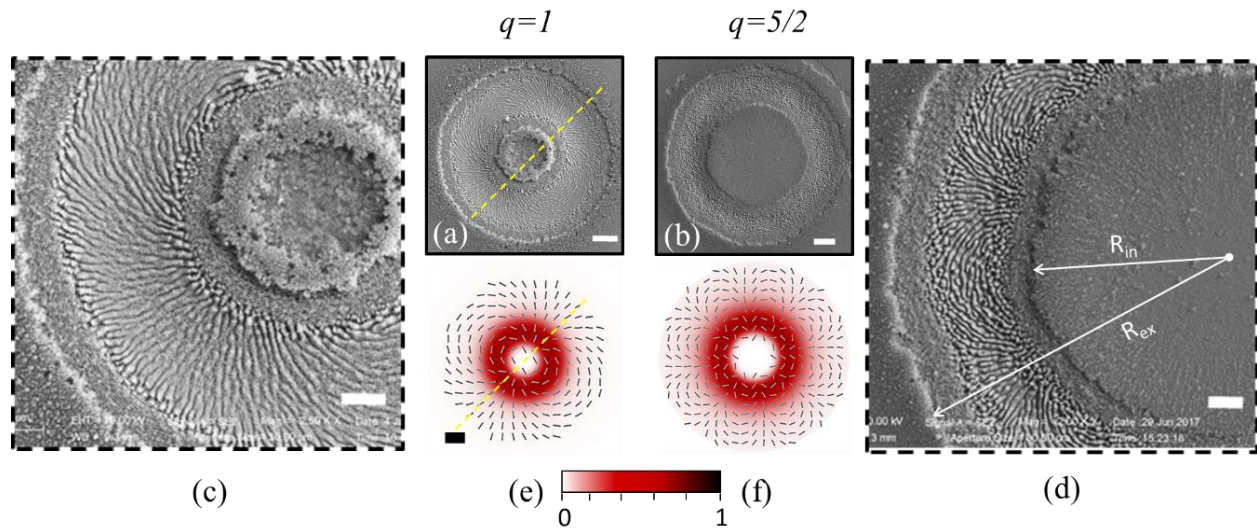

Figure 3.2 Panels (a) and (b): SEM images showing the surface morphologies developed on the silicon target after an irradiation sequence of $N = 200$ pulses in tuned condition of q-plates ($\delta = \pi$), for (a) $q = 1$, and (b) $q = 5/2$, respectively. The pulse energy is $E_0 = 50$ µJ for $q = 1$ and $E_0 = 100$ µJ for $q = 5/2$. Panels (c) and (d) display zoomed views of the SEM image of panels (a) and (b), respectively. The scale bars in SEM images are 20 µm for (a) and (b) and 10 µm for (c) and (d). Panels (e) and (f) report simulation of far-field beam profile with local direction of the beam polarization. In the maps, each beam intensity profile is normalized to its own maximum value and shown in the color bar, while the spatial scale bar for the maps, shown in panel (e), is 20 µm. The yellow dotted line in panel (a) marks a direction along which grooves alignment closely resembles a quasi-radial pattern, while in panel (e) it shows the corresponding line in the SoP of the beam. On either side of this dotted lines, the surface structures and SoP of the beam are arranged as a family of spiral-like patterns.

Figure 3.2 reports examples of SEM images of the target surface and maps of the spatial profiles of both fluence and polarization for two VV beams, namely those produced with $q = 1$ and $q = 5/2$. In particular, panels (a) and (b) of Figure 3.2 illustrate the morphology of the crystalline silicon surface

after irradiation with $N = 200$ pulses at a pulse energy $E_0 = 50$ µJ for $q = 1$ and $E_0 = 100$ µJ for $q = 5/2$. The lateral panels (c) and (d) are zoomed views of the SEM images of panels (a) and (b), respectively, evidencing the LIPSS. Finally, panels (e) and (f) report two-dimensional maps of the laser beam SoP (ellipses) and fluence (intensity, in false colour) spatial distributions. In the maps, each beam intensity profile is normalized to its own maximum value.

The internal and external radii of each ablated annular crater depend on laser pulse energy as well as the topological charge q. It is evident that for any q value the singular region at low fluence in the center of the crater covered with large number of nanoparticles remains as it is. However, the ratio R_{in}/R_{ex} (indicated in Figure 3.2 (d)) clearly increases with the topological charge q, passing from $\approx 20\%$ at $q = 1/2$ to $\approx 55\%$ at $q = 5/2$ [14].

The SEM analysis of the LIPSSs in Figure 3.2 confirms the presence of three recognizable annular regions: the central ring covered by grooves and two alongside rings covered by ripples. The central ring is the region with highest peak fluence. The different width of the rippled regions is due to the slightly dissimilar variation of the beam intensity spatial profile at the two sides of its peak position. The average period of the ripples and grooves measured in the SEM images of Figure 3.2 (a) are (535 ± 36) nm and (1.7 ± 0.2) µm, respectively [14].

The dependence of the LIPSS period on different laser beam variables, such as laser pulse energy and number of pulses, was discussed by JJ Nivas et al. [10,20]. The dependence of ripples periods on laser pulse energy at a fixed number of pulses is very weak; instead, there is a decreasing trend of the ripples period with the number of pulses, at fixed energy. As for the grooves, both laser energy and number of pulses have direct effect on the grooves spatial period. Here, the variation of the LIPSS period on laser pulse energy and number of pulses follows a similar behavior. Moreover, our findings do not evidence dependence of the spatial period of surface structures on the topological charge q, but different topological charges produce different surface patterns due to the spatial variation of polarization and intensity distributions.

Spatial maps of the state of polarization (SoP) of the VV beams are shown Figure 3.2 (e and f). Comparison with Figure 3.2 (a and b) proves that the LIPSSs follows the direction of the local polarization. It is worthy to note that employing q-plates with higher values of q produces more complex spatial patterns and their orientation direction does not strictly follow the azimuthal or

radial polarization. It is also observable in Figure 3.2 (a), on the right and left sides of the dashed line, that the grooves disposition resembles the spatial distribution of the in-plane magnetic field lines associated to a bar magnet kept along the direction of the yellow dotted line. To support this picture, Figure 3.3 schematically depicts the expected behaviour for various values of q.
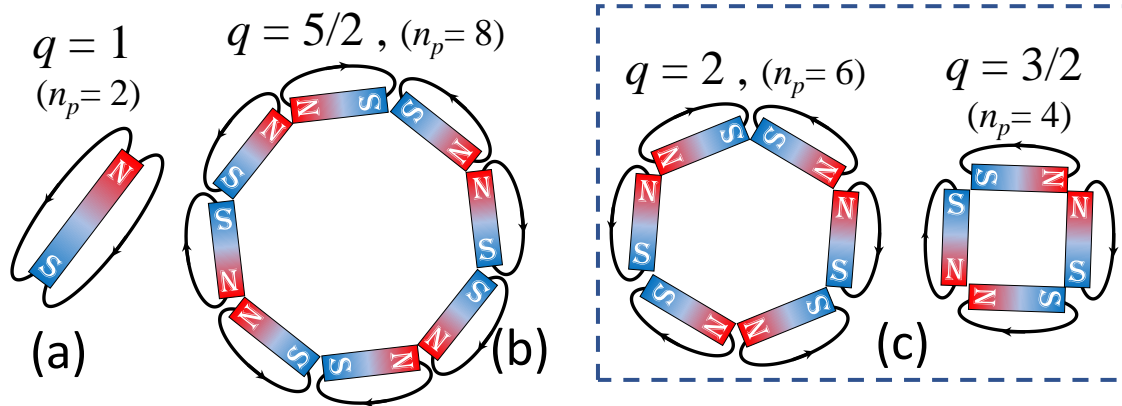

Figure 3.3 Panels (a) and (b) report schematic illustrations of the spatial distribution in-plane magnetic field lines generated by an arrangement of bar magnets graphically resembling the spatial distribution of the grooves formed by the VV beams generated by q-plates in tuned conditions ($\delta = \pi$) and shown in Figure 3.2 (a) and (b). The right inset (panel c) shows the same kind of schematic for the other q-plates used, namely $q = 3/2$ and $q = 2$. Interestingly, the number of independent polar vertices locations n_p corresponds to $n_p = 2(|\ell| - 1) = (4q - 2)$.

The spatial orientation of the grooves' patterns (Figure 3.2 (b)) produced by the VV beam with $q = 5/2$ behaves as the in-plane magnetic field lines generated by eight bar magnets arranged as in Figure 3.3 (b). This is confirmed also for the other q values, for which the representative sketches are shown in Figure 3.3 (c). Finally, the spatial orientation of the grooves' patterns formed by different q-plates evidences that the number of independent polar vertices locations is equal to $n_p = 2(|\ell| - 1)$, with alternating N and S poles.

3.3.2 Effect of variation of optical retardation on surface structures

As indicated by Equation (2), the fractional contribution of the two components depends on the

optical retardation δ, which is easily controlled by the external voltage. Hereafter, we illustrate the effect of the optical retardation tuning on the surface structures imprinted on the silicon target for several δ values, for the case $q = 1$.
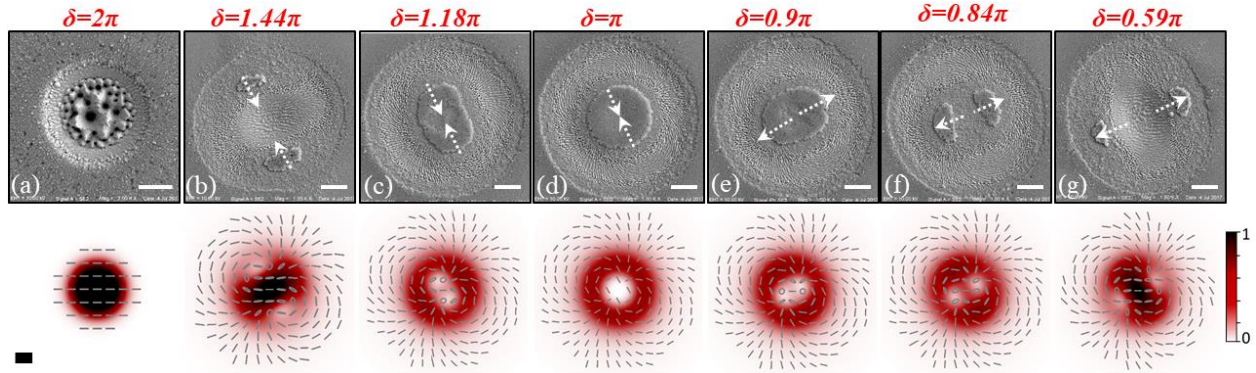

Figure 3.4 Panels (a)-(g) show SEM images of the silicon surface after irradiation with VV beams generated by q-plate with $q = 1$ at different values of the optical retardation δ ranging from $\delta = 2\pi$ (Gaussian beam) to $\delta = 0.59\pi$ (number of laser pulses $N = 200$, pulse energy $E_0 \approx 40$ µJ). For the sake of completeness, panel (d) shows the case of a tuned q-plate ($\delta = \pi$) corresponding to a VV beam with $|\ell| = 2$, discussed in the previous section. In each SEM image, the dotted arrows mark the direction along which the regions of minimum intensity of the VV beam move while varying the optical retardation δ. The scale bar in each SEM image corresponds to 20 µm. For each case, the lower panel displays the corresponding spatial distribution of the VV beam intensity and SoP. The scale bar, shown in lower left map, is 20 µm.

The SEM images shown in upper panels of Figure 3.4 report an experimental survey of surface patterns produced by a VV beam carrying an OAM $l = \pm 2$, in the condition of $N = 200$ laser pulses at an energy $E_0 \approx 40$ µJ, for various optical retardations from $\delta = 2\pi$ to $\delta = 0.59\pi$.

The highest contribution of the VV beam occurs in the case of $\delta = \pi$ (Figure 3.4 (d)), which is the optimal tuned condition discussed in detail in section 3.3.1. In the case of $\delta = 2\pi$, the output beam is completely Gaussian (Figure 3.4 (a)). Comparison between these two extreme cases shows that the size of the crater formed by the Gaussian beam G_H is smaller than that of the optimal tuned condition of the q-plate corresponding to the VV beam V_q. Moreover, while in the case of the VV beam ripples decorate either sides of the grooved central annular region (22 ± 1) µm wide, the

morphology of the crater induced by the Gaussian beam is rather different. This diverse texture is due to the fact that the present analysis is carried out at a fixed energy $E_0 \approx 40$ μJ, which in the case of G_H is spread over a smaller spot than for V_q, thus leading to a higher peak fluence, as also indicated by the intensity maps of Figure 3.4 (lower panels). The peak fluence of the Gaussian beam at the beam centre ($x = 0$, $y = 0$) is $\frac{2E_0}{\pi w_0^2} \approx 1.4$ J/cm^2, which is about 2.7 times larger than that of peak fluence value $2e^{-1}\frac{E}{\pi w_0{}^2} \approx 0.51$ J/cm^2 of the V_q beam with $|\ell| = 1$ occurring at a radial position $r_p \approx 30$ μm [21].

We illustrate the variation of δ for $q = 1$. A slight change from the optimal tuning, $\delta_{\text{opt}} = \pi$, transforms the central circular region into an elliptical area (see panels (c) and (e) of Figure 3.4). Further detuning changes it into two separate ellipses. Interestingly, the major axes of ellipses in conditions of $\delta = 1.44\pi$ and $\delta = 0.84\pi$ (panels (b) and (f)) depend on the sign of $(\delta - \delta_{\text{opt}})$ and are orthogonal to each other.

There is a direct relationship between the number of split regions and the q number of the q-plate. To clarify this, we consider the progressive change in the contributions of the two fields, i.e., G_H and V_q terms of Equation (2). The observed direction along which the region of minimum fluence moves depends on the input polarization direction and on the value of α_0, which in the present case is estimated to be $\alpha_0 \approx -\pi/6$. Splitting of the minimum fluence region in two parts is a consequence of the decay of the central high-order optical VV beam, associated with the two circular components, into elementary ones [22].

3.4   Fabrication of unconventional patterns

This section illustrates how variation of the optical retardation δ for higher values of the topological charge q is able to offer one-step structuring of peculiar patterns. Figure 3.5 reports SEM images of fabricated structures with VV beams generated with q-plates with $q = 3/2$ (panels a, b), 1 (panels e , f), 2 (panels g , h), $5/2$ (panels i and k). Two conditions of optical retardation δ, before and after the optimal tuned condition, are shown for each case. Taking as an example $q = 3/2$, the number of ablated lobes for $\delta = 1.51\pi$ or non-ablated islands for $\delta = 0.59\pi$ of the

constituent helical beams is in agreement with the OAM of the V_q component, i.e. $|\ell| = 3$. These three individual shapes are located on a circular track at $\approx 120°$ from each other, surrounding a triangular central region. This form is consistent with the spatial distribution of the laser fluence of the VV beam, shown in Figure 3.5 (c) and (d).
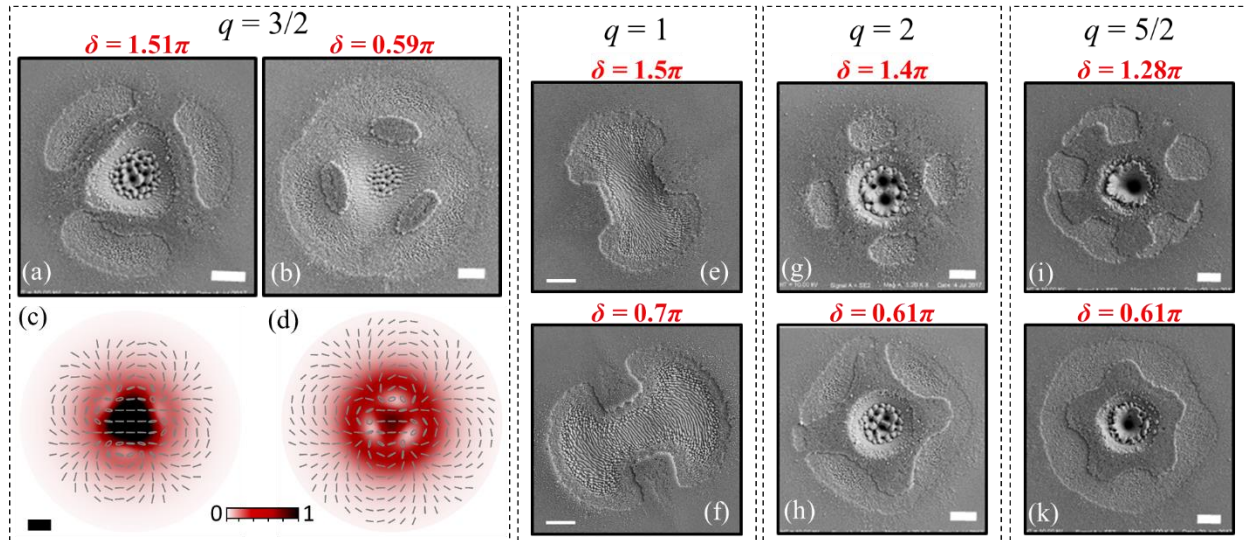

Figure 3.5 SEM images illustrating the structures formed on the silicon surface after irradiation with fs VV beams generated by three different q-plates for two different values of the optical retardation δ. The scale bar in the SEM images corresponds to 20 µm. Panels (a) and (b) show the case of $q = 3/2$ for $\delta = 1.51\pi$ and $\delta = 0.59\pi$ at a pulse energy $E_0 = 65$ µJ. For this case, the lower panels (c) and (d) display the corresponding simulated far field intensity and SoP patterns of the corresponding VV beams. The scale bar, shown in panel (c), is 20 µm. Panels (e) and (f) illustrate the case of $q = 1$ for $\delta = 1.5\pi$ and $\delta = 0.7\pi$ at a pulse energy $E_0 = 20$ µJ and $N = 100$. Panels (g) and (h) show the case of $q = 2$ for $\delta = 1.4\pi$ and $\delta = 0.61\pi$ at a pulse energy $E_0 = 55$ µJ and $N = 200$. Panels (i) and (k) report the case $q = 5/2$ for $\delta = 1.28\pi$ and $\delta = 0.61\pi$ at a pulse energy $E_0 = 100$ µJ and $N = 200$.

Accordingly, two lobes are observed with $q = 1$, (Figure 3.5 (e) and (f)), four lobes for $q = 2$ (Figure 3.5 (g) and (h)) and the morphology consists of five arms in the case of $q = 5/2$ (Figure 3.5 (i) and (k)). All the data confirm a remarkable relationship between the characteristics of the generated patterns and the OAM of the helical beams forming the V_q component, i.e. $|\ell| = 2, 4$ and 5, respectively. Moreover, in both cases, the orientation of the LIPSS imprinted in the ablated

regions is consistent with the SoP of the VV beams [13,14].

Apparently, an appropriate optical retardation tuning can lead to a spatial fluence distribution limiting the ablation in the central area of the crater whose shape results from the spatial modulation of the VV beam fluence, and the existence of a definite threshold for material removal in the laser ablation process. As displayed in Figure 3.4, the singularities are keen to stay apart when δ coefficient is less than one. At values of δ slightly below the optimal tuned condition the distance between the two non-ablated islands is still not enough to lead to their complete separation. For instance, Figure 3.6 shows SEM images of structures produced with VV beams with four different q at selected values of the optical retardation δ. For $q = 1$, in panel (a) of Figure 3.6 an elliptical non ablated area is formed.
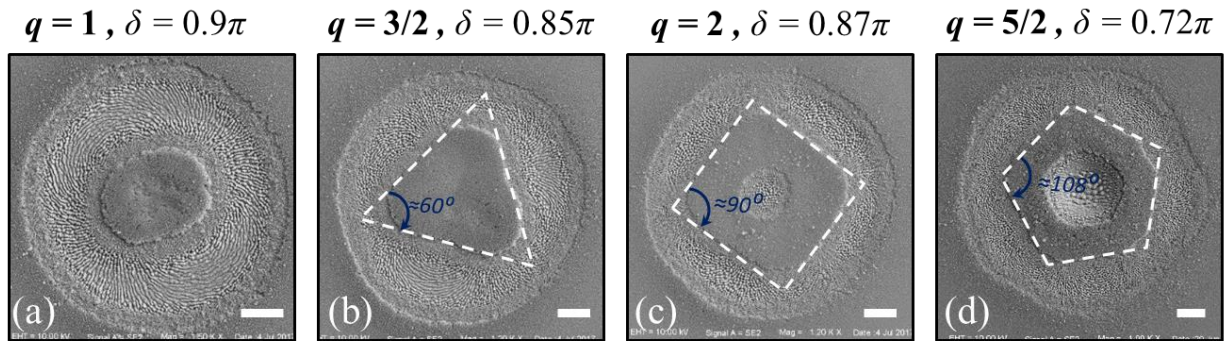

Figure 3.6 SEM images of the silicon surface after irradiation with $N = 200$ fs VV pulses generated by four different q-plates; the topological charge, q, and optical retardation δ indicated on the top of each image. The scale bars in the images correspond to 20 µm. The structures are produced at a laser pulse energy of: (a) 40 µJ, (b) 65 µJ, (c) 55 µJ, and (d) 100 µJ, respectively.

Hence, the other examples for $q = 3/2$, 2 and 5/2 show that with an appropriate tuning non-ablated central area following triangular, square and pentagonal geometry, respectively, can be formed. The white dashed shapes in Figure 3.6 are guides to the eyes. In panel (c) and (d), the formation of a circular ablated area within the central regions is due to the gradual increase of the intensity of the G_H component at the spot center. These examples suggest that appropriate optical tuning of the q-plates allows generating VV beams capable of scribing peculiar geometrical shapes on the sample surface that are characterized by a fairly good degree of regularity. The number of sides of the imprinted figure is directly related to the OAM, $|\ell|$, carried by the left and right

circularly polarized helical beams forming the V_q component, going from a segment with rounded extremes at $|\ell| = 2$ to a blunt pentagon at $|\ell| = 5$. In the following, the creation of a variety of surface structures, like laser induced periodic surface structures, multi-spot arrays and shaped ablation craters, is demonstrated by direct laser surface structuring with vector vortex beams at different values of q.

3.4.1 Mask-free insular patterns

In the previous section we investigated how variation of intensity distribution of VV beam profile by means of variation of optical retardation can affect generation of peculiar surface structures through superposition of unconverted part of the input Gaussian beam with an annular VV beam. This can provide a feasible strategy in order to produce mask-free subtractive manufacturing through localized ablation or in material transfer methods.

Here we illustrate an optical shaping of the VV beam intensity producing multiple beam spots at the focal plane. This is achieved by filtering the VV beam in tuned conditions with a linear polarizer, thus obtaining a multi-spot pattern in the focal plane with the number of lobes $n = 4q$.
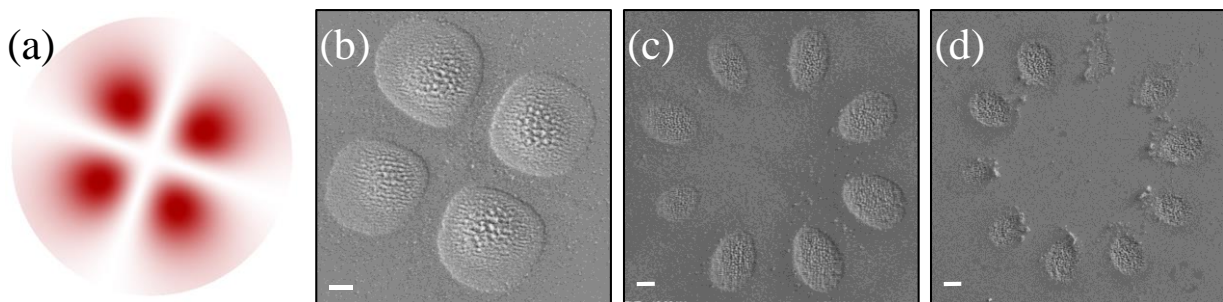

Figure 3.7 Panel (a) reports an example of intensity map of the VV beam for $q = 1$ after filtering with a linear polarizer transmitting the horizontal polarization, which illustrates the formation of a multi-spot pattern at the focal plane. Panel (b) shows a SEM image of the surface pattern produced by the beam reported in (a), for $N = 50$ and $E_0 = 40$ μJ. Panels (c) and (d) report SEM images of surface patterns produced by VV beams filtered by a vertically transmitting linear polarizer for $q = 2$ ($N = 100$ and $E_0 = 70$ μJ) and $q = 5/2$ ($N = 200$ and $E_0 = 50$ μJ). The scale bars in panels (b), (c) and (d) are 20 μm.

Peculiar shapes generated by polarization filtering of VV beams generated by q-plates with a topological charge q in tuned conditions are shown in Figure 3.7. Panel (a) of Figure 3.7 shows an example of the 4 lobes intensity pattern for $q = 1$ after filtering with a linear polarizer transmitting only the parts of the beam that are horizontally polarized. The corresponding SEM image of the sample surface obtained for an irradiation sequence of $N = 50$ pulses at an energy $E_0 = 40$ µJ is reported in Figure 3.7(b), which clearly shows the formation of a tetrameric ablative micro-pattern. Panels (c) and (d) of Figure 3.7 report two further examples obtained by exploiting the VV beams generated by q-plates with $q = 2$ and $q = 5/2$, respectively, that after filtering with a vertically transmitting linear polarizer imprint a pattern composed of 8 and 10 lobes on the target surface.

3.4.2   Fabrication of large area peculiar surfaces

Here we illustrate the possibility of fabricating arrays of surface structures with peculiar shapes as those obtained by fluence spatial profile tuning through a step scanning approach. In this way, direct surface writing of a large area can be achieved with a repetition of an elemental crater shape and its surface structures in a given spatial arrangement. Such an approach has been recently applied to elaborate large area of biomimetic surfaces composed of hierarchical structures on Ni showing super-hydrophobic behavior by using a phase plate capable of producing radially and azimuthally polarized VV beams [23]. In the following, we show some examples of patterns obtained by step scan with VV beams produced by a q-plate with topological charge $q = 1$. The used number of pulses for each elemental crater is $N = 100$ and the pulse energy is $E_0 = 20$ µJ.

Figure 3.8 (upper panels a-c) reports SEM images of patterns fabricated by using a VV beam generated in tuned conditions ($\delta = \pi$). Three examples are reported illustrating how the morphological features of the surface varies as a function of the step size Δ. At $\Delta = 120$ µm, the SEM images reported in panel (a) of Figure 3.8, show an array of well separated annular craters (as indicated by the dashed yellow lines) inscribed within a connected background of the pristine sample surface. Reducing Δ to values smaller than D (the diameter of the elemental crater is $D \approx 110$ µm) the craters partially overlap, as for example shown in panels (b) for $\Delta = 100$ µm. This leads to a surface morphology composed by a periodic array of disks with a diameter of ≈ 45 µm (upper dashed yellow line in panel (b)), corresponding to the central non-ablated area of each

crater, intercalated with a secondary pattern of inclined squares with a side of ≈ 30 μm (lower dashed yellow line in panel (b)). Finally, at still lower value of Δ, e.g. for $\Delta = 80$ μm as reported in panels (c), a regular array of disks separated by a background fully decorated with LIPSS is eventually produced.
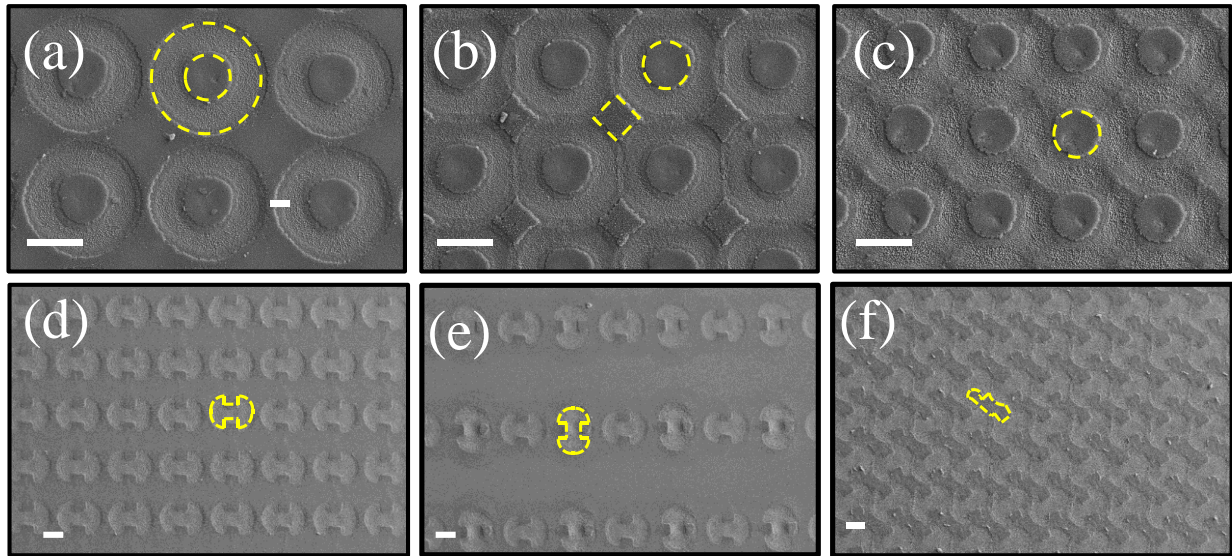

Figure 3.8 SEM images of the patterns obtained by using a VV beam generated by a q-plate with topological charge $q = 1$ in tuned conditions for (a), (b) and (c) and slightly untuned $\delta \approx 0.7\pi$ for (d), (e) and (f). The number of pulses for each elemental crater is $N = 100$ and the pulse energy is $E_0 = 20$ μJ. The nominal step size of the translation stage is $\Delta = 120$ μm for (a), $\Delta = 100$ μm for (b) and $\Delta = 80$ μm for (c). The scale bars are 50 μm for all the panels. The unitary tiles of the pattern are evidenced by dashed yellow lines.

Instead, lower panels of Figure 3.8 (d-f) illustrate the case of patterns fabricated by repeating shaped craters produced by a VV beam in un-tuned conditions. As an example, we selected the case of a bow-tie shape occurring for $\delta \approx 0.7\pi$. Three examples are reported illustrating various arrangements of the periodic arrays and the fairly good reproducibility of the craters. Panel (d) of Figure 3.8 reports a pattern of bow-tie shaped craters with one of the main symmetry axes aligned along the horizontal position. The orientation of the crater shape can be varied by acting on the direction of the input laser linear polarization to the q-plate, as shown for example in panel (e) were two consecutive elemental tiles of the array are rotated by 90° at each scanning step. Finally, panel (f) Figure 3.8 illustrates an example of pattern that can be achieved by writing bow-tie shaped

craters with their longer axis inclined at $\approx 30°$ and a step size (≈ 100 μm) slightly smaller than their major axis length (≈ 110 μm).

A variety of pattern can be possibly achieved by changing the step parameters and the shape and size of the elementary craters by voltage tuning and appropriate selection of the q-plate topological charge. This approach allows producing a variety of surface patterns in form of periodic or aperiodic arrays of shaped non-ablated island decorated with nanoparticles separated by a carpet of LIPSS and surface structures [13].

In brief, the experimental and theoretical investigations confirm that fs surface structuring with twisted like lights generated by q-plates offers more complex structures from both points of view of overall crater shapes and fine structures formation. The pictorial representation suggests that the grooves formed on the silicon target surface provide an easy and direct visualization of the beam SoP also for more complex beams, thanks to their inherent property of orienting along the field polarization. Taking into account the optical retardation δ tuning of a VV beam as another key parameter of surface texturing, it proves novel strategy to manipulate the fluence distribution of the beam, and fabricate specific surface structures, with peculiar shapes. This is achieved by simply tuning the voltage to the q-plate, thus making our approach very useful and advantageous as a beam shaping technique since it allows generating a variety of fields in an easy way and with the use of a flat and compact optical element.

Moreover, we have considered a facile way of obtaining a multi-spot beam pattern in the focal plane by a polarization filtering of the VV beam through a linear polarizer. Finally, the elaboration of surface patterns was illustrated through a spot-by-spot step scan approach that allows covering large area of the target sample.

In conclusion, irradiation with fs complex light beams can offer a valuable route to design unconventional surface structures, which, moreover, can provide basic units that replicated over larger areas allow fabricating complex surfaces with novel or extended functionality.

References

[1]   H. Rubinsztein-Dunlop, A. Forbes, M. V Berry, M.R. Dennis, D.L. Andrews, M. Mansuripur, C. Denz, C. Alpmann, P. Banzer, T. Bauer, E. Karimi, L. Marrucci, M. Padgett, M. Ritsch-Marte, N.M. Litchinitser, N.P. Bigelow, C. Rosales-Guzmán, A. Belmonte, J.P.

Torres, T.W. Neely, M. Baker, R. Gordon, A.B. Stilgoe, J. Romero, A.G. White, R. Fickler, A.E. Willner, G. Xie, B. McMorran, A.M. Weiner, Roadmap on structured light, J Opt. 19 (2017) 013001. https://doi.org/10.1088/2040-8978/19/1/013001.

[2]   J. Secor, R. Alfano, S. Ashrafi, Complex Light, IOP Publishing, 2016. https://doi.org/10.1088/978-0-7503-1371-1.

[3]   K.K. Anoop, A. Rubano, R. Fittipaldi, X. Wang, D. Paparo, A. Vecchione, L. Marrucci, R. Bruzzese, S. Amoruso, Femtosecond laser surface structuring of silicon using optical vortex beams generated by a q-plate, Appl Phys Lett. 104 (2014) 241604. https://doi.org/10.1063/1.4884116.

[4]   C. Hnatovsky, V.G. Shvedov, N. Shostka, A. V. Rode, W. Krolikowski, Polarization-dependent ablation of silicon using tightly focused femtosecond laser vortex pulses, Opt Lett. 37 (2012) 226. https://doi.org/10.1364/OL.37.000226.

[5]   K. Lou, S.-X. Qian, X.-L. Wang, Y. Li, B. Gu, C. Tu, H.-T. Wang, Two-dimensional microstructures induced by femtosecond vector light fields on silicon, Opt Express. 20 (2012) 120. https://doi.org/10.1364/OE.20.000120.

[6]   J.J.J. Nivas, H. Shutong, K.K. Anoop, A. Rubano, R. Fittipaldi, A. Vecchione, D. Paparo, L. Marrucci, R. Bruzzese, S. Amoruso, Laser ablation of silicon induced by a femtosecond optical vortex beam, Opt Lett. 40 (2015) 4611. https://doi.org/10.1364/OL.40.004611.

[7]   K.K. Anoop, R. Fittipaldi, A. Rubano, X. Wang, D. Paparo, A. Vecchione, L. Marrucci, R. Bruzzese, S. Amoruso, Direct femtosecond laser ablation of copper with an optical vortex beam, J Appl Phys. 116 (2014) 113102. https://doi.org/10.1063/1.4896068.

[8]   B. Wetzel, C. Xie, P.-A. Lacourt, J.M. Dudley, F. Courvoisier, Femtosecond laser fabrication of micro and nano-disks in single layer graphene using vortex Bessel beams, Appl Phys Lett. 103 (2013) 241111. https://doi.org/10.1063/1.4846415.

[9]   J.J. Nivas, F. Cardano, Z. Song, A. Rubano, R. Fittipaldi, A. Vecchione, D. Paparo, L. Marrucci, R. Bruzzese, S. Amoruso, Surface Structuring with Polarization-Singular Femtosecond Laser Beams Generated by a q-plate, Sci Rep. 7 (2017) 42142. https://doi.org/10.1038/srep42142.

[10]   J. JJ Nivas, S. He, A. Rubano, A. Vecchione, D. Paparo, L. Marrucci, R. Bruzzese, S. Amoruso, Direct Femtosecond Laser Surface Structuring with Optical Vortex Beams Generated by a q-plate, Sci Rep. 5 (2015) 17929. https://doi.org/10.1038/srep17929.

[11]   J. JJ Nivas, S. He, Z. Song, A. Rubano, A. Vecchione, D. Paparo, L. Marrucci, R. Bruzzese, S. Amoruso, Femtosecond laser surface structuring of silicon with Gaussian and optical vortex beams, Appl Surf Sci. 418 (2017) 565–571. https://doi.org/10.1016/j.apsusc.2016.10.162.

[12]   M. Alameer, A. Jain, M.G. Rahimian, H. Larocque, P.B. Corkum, E. Karimi, V.R. Bhardwaj, Mapping complex polarization states of light on a solid, Opt Lett. 43 (2018)

5757. https://doi.org/10.1364/OL.43.005757.

[13]   J. JJ Nivas, E. Allahyari, F. Cardano, A. Rubano, R. Fittipaldi, A. Vecchione, D. Paparo, L. Marrucci, R. Bruzzese, S. Amoruso, Vector vortex beams generated by q-plates as a versatile route to direct fs laser surface structuring, Appl Surf Sci. 471 (2019) 1028–1033. https://doi.org/10.1016/j.apsusc.2018.12.091.

[14]   J. JJ Nivas, E. Allahyari, F. Cardano, A. Rubano, R. Fittipaldi, A. Vecchione, D. Paparo, L. Marrucci, R. Bruzzese, S. Amoruso, Surface structures with unconventional patterns and shapes generated by femtosecond structured light fields, Sci Rep. 8 (2018) 13613. https://doi.org/10.1038/s41598-018-31768-w.

[15]   S. Slussarenko, A. Murauski, T. Du, V. Chigrinov, L. Marrucci, E. Santamato, Tunable liquid crystal q-plates with arbitrary topological charge, Opt Express. 19 (2011) 4085. https://doi.org/10.1364/OE.19.004085.

[16]   B. Piccirillo, V. D'Ambrosio, S. Slussarenko, L. Marrucci, E. Santamato, Photon spin-to-orbital angular momentum conversion via an electrically tunable q-plate, Appl Phys Lett. 97 (2010) 241104. https://doi.org/10.1063/1.3527083.

[17]   L. Marrucci, C. Manzo, D. Paparo, Optical Spin-to-Orbital Angular Momentum Conversion in Inhomogeneous Anisotropic Media, Phys Rev Lett. 96 (2006) 163905. https://doi.org/10.1103/PhysRevLett.96.163905.

[18]   F. Cardano, E. Karimi, S. Slussarenko, L. Marrucci, C. de Lisio, E. Santamato, Polarization pattern of vector vortex beams generated by q-plates with different topological charges, Appl Opt. 51 (2012) C1. https://doi.org/10.1364/AO.51.0000C1.

[19]   F. Cardano, E. Karimi, L. Marrucci, C. de Lisio, E. Santamato, Generation and dynamics of optical beams with polarization singularities, Opt Express. 21 (2013) 8815. https://doi.org/10.1364/OE.21.008815.

[20]   J.J. Nivas, PhD thesis: Ultrafast laser surface structuring with Gaussian and Optical Vortex beam, Università degli Studi di Napoli Federico II, 2017.

[21]   E. Allahyari, J. JJ Nivas, F. Cardano, R. Bruzzese, R. Fittipaldi, L. Marrucci, D. Paparo, A. Rubano, A. Vecchione, S. Amoruso, Simple method for the characterization of intense Laguerre-Gauss vector vortex beams, Appl Phys Lett. 112 (2018) 211103. https://doi.org/10.1063/1.5027661.

[22]   A. D'Errico, M. Maffei, B. Piccirillo, C. de Lisio, F. Cardano, L. Marrucci, Topological features of vector vortex beams perturbed with uniformly polarized light, Sci Rep. 7 (2016) 1–11. https://doi.org/10.1038/srep40195.

[23]   E. Skoulas, A. Manousaki, C. Fotakis, E. Stratakis, Biomimetic surface structuring using cylindrical vector femtosecond laser beams, Sci Rep. 7 (2017) 45114. https://doi.org/10.1038/srep45114.

4   Effect of various experimental parameters in laser surface structuring of silicon

Abstract – The laser beam parameters influence the characteristics of the surface structures, e.g. shape of crater and fine features. As discussed earlier, number of pulses and energy per pulse have significant role in defining density, arrangement and size of the LIPSSs as well on the decoration of the processed surface with ablated particles. Here, we analyze further how laser beam features like wavelength and pulse repetition rate influence the LIPSS features. The experimental results are compared with some simulation predictions addressing the role of hydrothermal wave character of the grooves formation. In addition, we report on the effect of the ambient pressure.

4.1   Introduction

The most common low spatial frequency LIPSS (LSFL) are ripples with near-wavelength period. Ripples have been very much investigated and their formation mechanisms are generally ascribed to the excitation of surface scattered waves, e.g. surface plasmon polaritons (SPPs), or self-organization of surface instabilities [1–3]. However, for the generation of grooves, the other surface structures with supra-wavelength period and orientation parallel to the laser polarization, there is no general explanation yet. Some prediction models [1] and experimental findings [4] suggest a relevant influence of hydrodynamics of molten material and redeposition of ablated particles [1,4–6]. Grooves typically form at high fluence and number of pulses, hence hereafter we will select experimental conditions that favor their creation in order to clarify the influence of the experimental parameters on this less investigated LIPSS. In particular, in this chapter the influence of ambient and laser beam conditions is discussed. The experiments are carried out with standard beams with a Gaussian intensity profile and homogenous polarization. In section 4.2, the influence of the pulse repetition rate (RR) on fs laser irradiation of silicon, in air, is experimentally investigated in the range 10 Hz – 200 kHz. The analysis considers both the features of the shallow craters and the LIPSSs produced inside the crater evidencing interesting effects of the pulse repetition rate. Section 4.3 reports experimental results on an analysis carried out at two different laser wavelengths λ, namely 513 nm and 1026 nm, at fluences above the grooves formation

threshold. Both static and dynamic irradiations conditions are used and the role of number of pulses N and laser peak fluence F_p for both wavelengths is discussed. In this section, also the results of simulations carried out in a collaboration with Dr. George D. Tsibidis are shown and compared to the experimental findings. In section 4.4, the variation of ambient pressure and its effect on the morphology of ripples and formation of grooves is highlighted. Moreover, the impact of variation of laser beam polarization in vacuum condition is also investigated.

4.2   Effect of laser pulse repetition rate

Direct fs laser surface structuring can be very useful for applications like fast generation of high regular patterns over a large area [7] or for fast laser drilling [8,9]. In such a case high repetition rate laser source are considered and associated to dynamic and static irradiation conditions. Studies on high repetition rate (HRR) ($\geq$ 50 kHz) for both micro-hole drilling and surface texturing show interesting results [10–13], suggesting that repetition rate of pulsed laser beams can open a new degree of freedom to approach the proper temporal separation between pulses during fs laser processing.

In this section, results of an experimental analysis designed to investigate the process of irradiation of a silicon target from low to high repetition rates, in the range 10 Hz – 200 kHz are presented. Features of both crater and fine structures are analyzed as a function of the fs laser pulse repetition rate. The samples were prepared in static irradiation conditions with a fixed number of pulses.

The fs pulses were provided by a chirped pulse amplification Yb:KGW (1030 nm, $\approx$180 fs, maximum pulse energy $\approx$1.5 mJ), capable of delivering pulses from single shot up to a maximum repetition rate of 200 kHz. The beam was focused on an intrinsic, (100) silicon plate using a lens with a nominal focal length of 200 mm, in air. The target was mounted on a XY-translation stage located perpendicular to the laser beam direction. The morphology of the irradiated surfaces was analyzed by field emission scanning electron microscopy (FE-SEM) for the LSFL structures and by a stylus profilometer (Dektak XT) capable of providing a tridimensional (3D) view of the shallow crater profile.

The laser beam has the Gaussian spatial profile. Therefore, the $1/e^2$-beam waist w_0, which was discussed in detail in Chapter 2, is obtained by employing the following relation:

$$r^2 = \frac{w_0}{2} \, ln\left(\frac{E}{E_{th}}\right) \tag{1}$$

where r is the radius of the crater produced on silicon with laser pulse energy E, and E_{th} is the threshold energy for ablation. The size of the craters generated by $N = 200$ number of pulses, using lower RRs of 10 Hz and 1 kHz are well fitted to Equation (1) and gives the values of $w_0 = (35 \pm 1)$ µm, and $E_{th} = (2.6 \pm 0.4)$ µJ. The dependence at high repetition rates of 20 and 200 kHz shows some changes [14], as illustrated later.

Figure 4.1 shows the variation of the crater radius with RR; the values are normalized to the crater size at 10 Hz. We can observe two regimes of low and high RRs with a clear transition occurring for RR around 10 kHz. For HRR irradiation, two effects can influence the process: heat accumulation and ablation plume shielding. Heat accumulation occurs when the fraction of energy released to the target in form of heat cannot diffuse out because the temporal separation between consecutive pulses is too short [11,13,15,16].
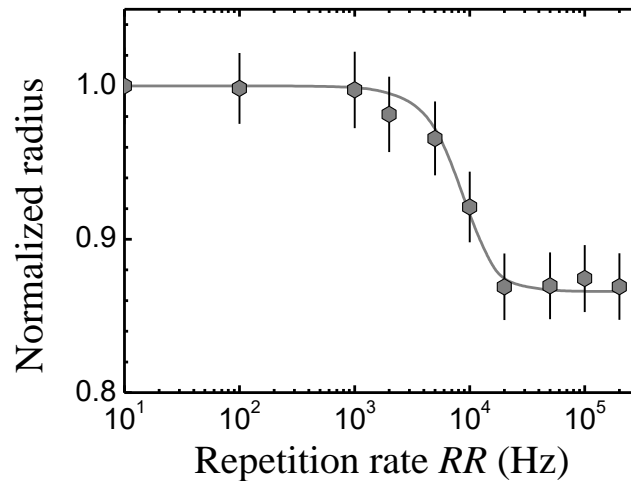

Figure 4.1 Crater radius dependence on the repetition rate RR, at $E = 10$ µJ and $N = 200$ pulses. The data points are normalized to the value of the crater radius at 10 Hz. The line is a guide to the eye [14].

Pulse after pulse, an increase of the target temperature occurs, and transport of energy out of the irradiated region can cause irreversible changes, and surface damage in the surroundings of the irradiated area. This effect has been typically observed for values of several hundred kHz, or MHz, and is expected to become important for silicon at RRs of several MHz or more [17]. In such cases, larger craters with rougher shapes are also observed due to heat diffusion and accumulation [11,16]. Moreover, the effect increases at higher RRs. In our case, however, we observe a similar trend of the crater size for 20 kHz and 200 kHz [14] and a reduction of the crater size with respect to that obtained at low RR. This suggests that heat accumulation should play a minor role in our experimental conditions.

In ablative conditions, the second effect that can influence the process, i.e., plume shielding, takes place when the residence time of the cloud of ablated particles above the target surface is comparable with the pulse separation. Ultrashort laser ablation of a solid target results in the emission of an atomic plasma plume consisting of electrons, atoms and ions followed, on a longer timescale, by a cloud of nanoparticles, which typically accounts for the largest part of the ablated volume [18–21]. The pulse separation in multi-pulse laser irradiation at high repetition rate is large enough and involves the interaction with the ablated material at a longer delay after the pulse. The typical expansion time of a fs laser ablation nanoparticles plume in a vacuum is of several tens of μs, and its residence time over the target surface becomes even larger in a background gas, due to confinement effects [14].

The craters of SEM images in Figure 4.2 are produced by irradiation sequences of $N = 200$ laser pulses at a pulse energy $E = 10$ μJ for different values of the repetition rates. Panels (a) and (e) shows the reduction in size of the ablated crater at 200 kHz compared to that of 10 Hz. The observed reduction of the crater size can be reasonably ascribed to a plume shielding effect that induces a reduction of the effective energy reaching the target surface, due to absorption and scattering of the laser light by the ablated material close to the target surface at these values of the RRs [14]. Plume shielding proposes some possibilities of nonlinear effects on beam propagation such as self-focusing and plasma defocusing due to direct interaction of particle cloud with the laser beam. This effect may make the beam to arrive on the surface in Gaussian deviated spatial profile, consequently, the crater is larger and the shape is not perfectly Gaussian. However, the fact that we observe the formation of smaller crater with a rather circular shape and whose square

radius follows pretty well the predicted dependence for a Gaussian beam profile but with a smaller slope, even at high RR values, seems to suggest that such effects should play a minor role in our experimental conditions [14].
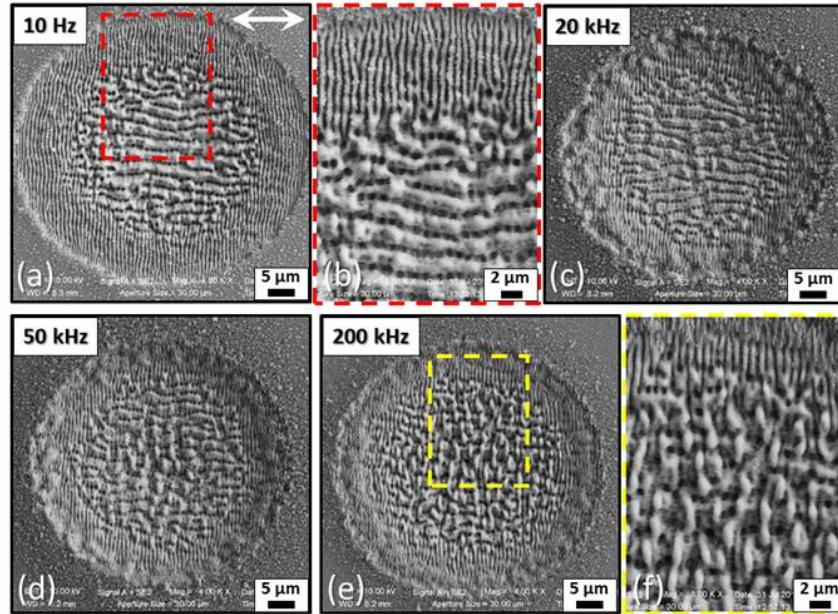

Figure 4.2 SEM images of the irradiated samples at $N = 200$ pulse and $E = 10$ µJ, for different values of the pulse repetition rate. Panel (a) shows the image corresponding to 10 Hz that is exemplificative of the crater morphology in the low repetition rate regime. Panel (b) is a zoomed view corresponding to the red box in panel (a). Panels (c), (d) and (e) report SEM images at RR 20, 50 and 200 kHz, respectively. Panel (f) is a zoomed view of the yellow box in panel (e). The arrow in the upper right corner of panel (a) shows the laser beam polarization direction [22].

The SEM images of panels (a) and (b) of Figure 4.2, corresponding to repetition rate $f_p = 10$ Hz, are representative of the LSFL generated in the low repetition rate regime that consist of sub-wavelength ripples and supra-wavelength grooves oriented along the direction perpendicular and parallel to the laser beam polarization, respectively. The grooves cover a central region with a diameter of ≈32 µm, while the ripples are present over an outer annulus with a thickness of ≈10 µm. The two structured regions are separated by a very thin transitional area of few microns, as evidenced in the zoomed view of panel (b) in Figure 4.2. Panels (c), (d) and (e) of Figure 4.2 show SEM images registered at $f_p = 20, 50$ and 200 kHz, respectively, illustrating changes occurring at high RR. The SEM images evidence a less regular crater edge and a reduction of the crater

diameter. More interestingly, the LSFL texture of the central part of the crater progressively varies with the pulse RR, while the outer ring of ripples is always present. At $f_p = 20$kHz, in panel (c) of Figure 4.2, the LSFL are rather similar to that observed at lower RR, showing an external rippled area surrounding a central grooved region. At $f_p = 50$ kHz, only few remnants of the grooves observed at lower repetition rates can be recognized, while the texture of the central part varies significantly, eventually displaying a well-developed network of crochet-like structures at $f_p = 200$ kHz (see i.e. panel (f) of Figure 4.2).

Figure 4.3 summarizes the experimental conditions for the formation of the different structures in the central region of the crater, symbolizing the type of surface structures observed for any couple of values of the parameters (f_p, F_p). However, as the local value of the fluence degrades from the peak value to the ablation threshold moving towards the periphery, we also consider that ripples are generally formed for values of F_p from the ablation threshold up to $F_p \approx 0.3$ J/cm^2 ($E = 5.5$ µJ), for any value of the repetition rate up to 200 kHz. This is indicated as a reddish-shaded area in Figure 4.3. The other colored areas identify regions of the parameters space in which LSFL can be assigned to grooves (bluish-shaded area) and crochet-like network (yellowish-shaded area), respectively, even if no sharp separation can be precisely defined. Interestingly, for $F_p \approx 0.35$ J/cm^2, we cannot recognize well-formed grooves for 10 Hz$\leq f_p \leq$1 kHz, while they form in the range 2 kHz $\leq f_p \leq$ 20 kHz. At larger values of $F_p \approx 0.45$ J/cm^2 and ≈ 0.5 J/cm^2, grooves are always present unless for the very high RRs, where a crochet-like network is generated. Besides the need for a deeper comprehension of the mechanisms leading to the disappearance of the grooves at the highest values of the parameters (f_p, F_p) here investigated, the plot of Figure 4.3 displays an interesting playground for the generation of a variety of LSFL by appropriate selection of peak fluence and repetition rate, thus confirming the feasibility of laser surface structuring for the generation of a wide range of surface structures.

We turn now to analyze the profile of the craters obtained by a profilometer and SEM. Figure. 4.4 reports the ablated craters produced by $N = 100$ laser pulses at an energy $E = 10$ µJ and repetition rate of $f_p = 50$ kHz. In this figure, panel (a) shows 3D view of the crater height profile in form of a bi-dimensional false color map. The map shows the formation of a circular crater with a diameter $D \approx 40$ µm (dotted blue circle) surrounded by a rim. As evidenced in the one-

dimensional cross section height profile of Figure 4.3(b), the rim reaches maximum height levels of ≈ 1 µm above the pristine surface of the silicon sample ($z = 0$), while the points of maximum depth in the central area of the crater are located at ≈ 1 µm below the original surface level. Therefore, the generated craters are very shallow as maximum depth and rim heights are ≈ 40 times smaller than diameter.
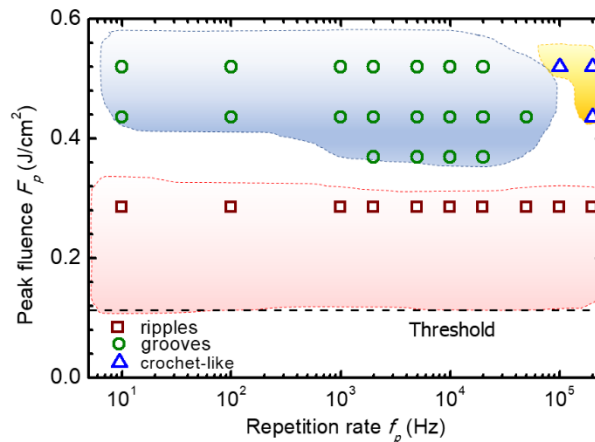

Figure 4.3 Type of LSFL observed for any couple of values of the parameters (f_p, F_p). The data refer to irradiation sequences with $N = 100$ laser pulses. The shaded areas identify regions of the parameters space where the specific LSFL is observed. The reddish-shaded area evidences the region in which ripples are formed considering that they are always present from the edge of the crater corresponding to the ablation fluence threshold up to about 0.3 J/cm², for all the repetition rates investigated.

The SEM image of the same crater is shown in inset of Figure 4.4 (b). The dashed circles in this SEM image correspond to the three arrows with the same colors in the cross-section profile of Figure 4.4 (b). The green shows the position of the zero-level pristine surface, the blue is the boundary of the crater according to what we see from the SEM and the red displays the location of highest position of rim registered by the profilometer. Considering these three locations on the ablated crater claims that the edges of the spots acquired by the SEM neither match with the zero-level nor the highest position of rim. In fact, it is positioned on a place between the zero-level and the rim; this is possibly due to very much shallow crater and also it depends on the focusing and image contrast of the SEM [22].
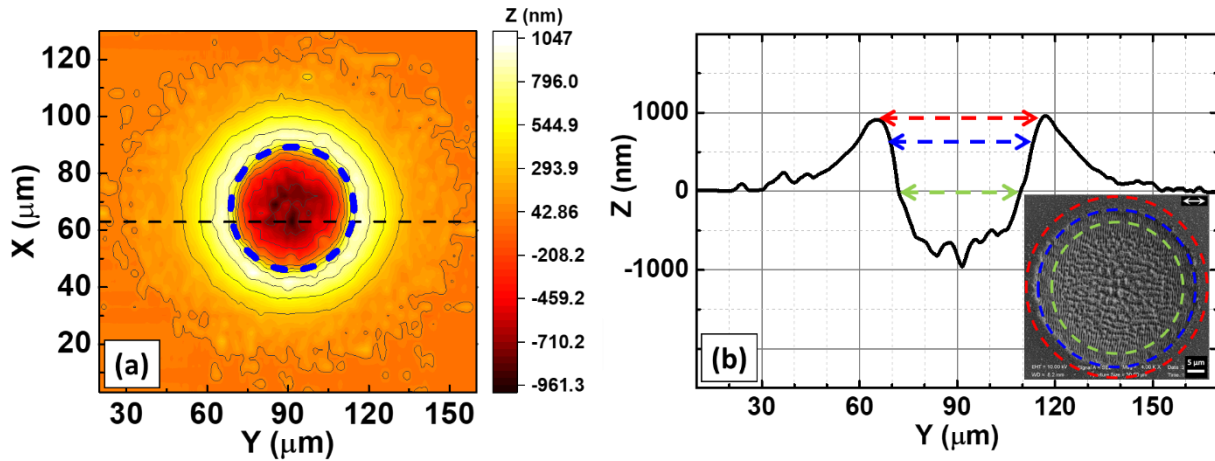
Figure 4.4 Panel (a) displays an example of a profilometer map of the shallow crater produced by a sequence of $N = 100$ pulses with an energy $E = 10$ µJ at a pulse repetition rate $f_p = 50$ kHz. Panel (b) shows a crater cross section profile along the horizontal dashed line reported on the map of panel (a) and crossing the deepest region of the crater. The three double-headed arrows in panel (b) identify the locations of the highest position of the rim (red), of the edge of crater observed by SEM imaging (inset in panel (b)) (blue) and of the locus of the points at height $z = 0$ corresponding to the original level of the pristine surface of the silicon sample (green), respectively. The dashed circle in panel (a) corresponds to the blue double-headed arrow of panel (b).

Figure 4.5 reports the dependence of crater topographic features on the RR. Figure 4.5 (a) shows the variation of the crater volume and average depth considering the regions below the zero-level pristine level (see the 3D view of the crater registered by profilometry in inset of Figure 4.5 (a)) as a function of pulse repetition rate. The dependence of both parameters on f_p is consistent with the presence of two different regimes with a sharp transition around 20 kHz. This reduction evidently is happening simultaneously with the sharp reduction of crater size at the same repetition rate, 20 kHz, as it was discussed in Figure 4.1. The same transition is observed for the volume of rim of crater (see Figure 4.5 (b)), where the redeposited ablated particles above the zero-level are located (see inset of Figure 4.5 (b)), as a function of f_p.

This fact suggests that for the low repetition rate regime ($f_p < 20$ kHz), the small variation is related to the intrinsic fluctuations of the ablation process occurring in the typical experimental conditions used in laser surface structuring. Then, a transition occurs to a high pulse repetition rate regime ($f_p > 20$ kHz) characterized by a progressive reduction of the ablation efficiency. These results confirm the previous explanation of a progressive reduction of the ablation rate as the RR reaches the tens of kHz region [14].
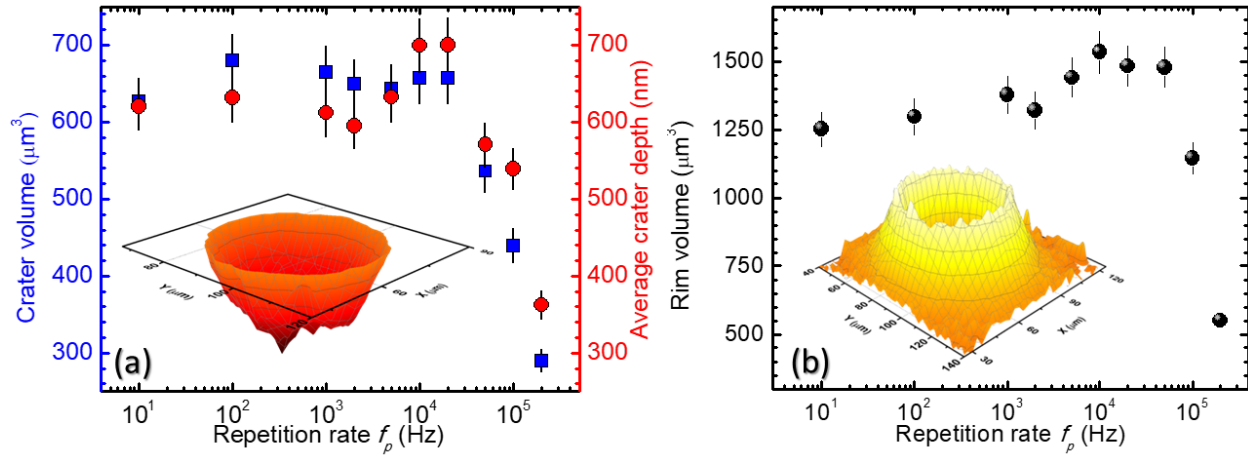
Figure 4.5 Panel (a) reports the variation of the crater volume (circles, left axis) and average crater depth (squares, right axis) on the pulse repetition rate f_p. Panel (b) shows the dependence of the rim volume as a function the pulse repetition rate f_p. The data refer to irradiation sequences with $N = 100$ laser pulses at a pulse energy $E = 10 \, \mu J$.

To conclude, in this section the generation of quasi-periodic surface features on crystalline silicon irradiated by fs laser pulses was investigated experimentally evidencing a variation in the surface morphology with respect to the RR in the range 10 Hz – 200 kHz. It is found that above-wavelength grooves formation is completely hindered as RR reaches 20 kHz, instead another quasi-periodic feature aligned normal to the polarization is identified. Our experimental results evidence a clear dependence of surface features formation when the same number of laser pulses is delivered to the target but at different repetition rate, in static conditions.

4.3   Effect of laser beam wavelength

Most of the experimental investigations on supra-wavelength periodic structures (e.g. grooves) exploit near-infrared Ti:Sa laser sources [5], usually with wavelength λ≈800 nm, and the spatial period of the grooves typically observed is larger than one micron ($\Lambda > 1 \, \mu m$). JJ Nivas et al. observed that the spatial period of the grooves produced by 400 nm fs laser beam shows a value of the order of two times the laser wavelength ($\Lambda_{groove} \approx 2\lambda_{laser}$) [23]. In this section, the results of an experiment carried out at two laser wavelengths to highlight the role of such parameter on the grooves features is reported.

Two set of experiments were carried out using both the fundamental ($\lambda_{1026} = 1026$ nm) and the second harmonic ($\lambda_{513} = 513$ nm), generated by a BBO crystal, provided by a Yb:KGW laser system with a pulse duration of ≈180 fs and a maximum energy of ≈1.5 mJ. The silicon target was exposed to the laser beam focused using a lens with focal length of 200 mm, in air, at a pulse repetition rate of 1 kHz. The sample was positioned on a XY translation stage. For both wavelengths, LIPSSs were generated in static and dynamic conditions. The laser beam with a Gaussian spatial profile hit the sample at normal incidence. The spot diameter D at $1/e^2$ of the maximum laser pulse fluence, F_p (for pulse energy E, $F_p = 8E/\pi D^2$), were estimated to be $D_{1026} \approx 72$ μm and $D_{513} \approx 78$ μm.

4.3.1   Grooves formation at both wavelengths λ_{513} and λ_{1026}

A general proposal for explaining the formation mechanism of LSFL for fs irradiation on metal and semiconductors takes into account the absorption of laser pulse energies by electrons. Electron-photon coupling lead this energy to be transferred to the lattice within few picoseconds [6,24]. Considering the fs laser ablation of silicon in different laser wavelengths, the energy absorption in visible regime is higher than that of NIR due to higher level of energy of photons at such wavelengths [23]. This suggests that, at the same laser fluence, irradiation with shorter wavelength gives higher chance of producing grooves [25].

Prior to the experiments in static and dynamic conditions, a set of single craters was realized with various number of pulses N and laser fluences F_p in order to evaluate the values of the threshold fluence for grooves formation at the two different wavelengths. The ripple and groove formation threshold fluences F_{th} were estimated by measuring the laser energy dependence of the radii of grooves and ripples edges from SEM micrographs of the irradiated spots [5]. The determined dependence of F_{th} of ripples and grooves for λ_{513} and λ_{1026} as a function of number of pulses N is reported in Figure 4.6 and follows the relation [26]:

$$F_{th}(N) = F_{th}(1)\, N^{\xi-1} \tag{1}$$

where ξ is the incubation factor and $F_{th}(1)$ is the fluence threshold for $N = 1$. In Figure 4.6, the solid lines are the fitting curves to the data points. The estimated values of fluence threshold and incubation factors are summarized in the Table 4-1.
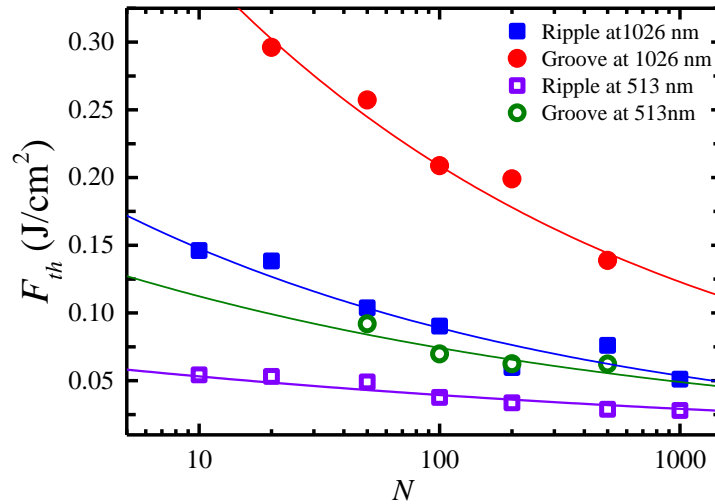

Figure 4.6 Variation of the fluence threshold F_{th} with the number of pulses N for ripples and grooves at both wavelengths λ_{1026} and λ_{513}. The uncertainties on the experimental data points are contained within their respective size. The solid lines are a fit to the dependence of Equation (1). The values of the fitting parameters are listed in Table 4-1.

The threshold fluence values and incubation factors are comparable with those reported in the literature [23,26,27]. We observe that the fluence threshold $F_{th}(1)$ at 513 nm is about 3.5 times lower than that of 1026 nm, confirming the larger effectiveness of ablation and LIPSS formation at the shorter wavelength. This is likely due to a diverse energy coupling efficiency to the silicon target of laser pulses with different wavelengths and to the consequent different level of excitation reached by the irradiated material [23]. In fact, LIPSS features depend on the absorption of laser pulse energies by electrons. Electron-phonon coupling lead this energy to be transferred to the lattice within few picoseconds [6,24]. Considering the properties of silicon for different light wavelengths, absorption in the visible is higher than NIR, thus suggesting that, at the same laser fluence, irradiation with the shorter wavelength gives higher absorbed energy and consequently more chance of producing grooves [25].

Table 4-1 Peak fluence threshold $F_{th}(1)$, in J/cm², for $N = 1$ pulse and incubation factor ξ for the two wavelengths used in the experiments, namely 513 nm and 1026 nm. The subscripts R and G refer to ripples and grooves, respectively. The peak fluence threshold for ripples corresponds to that needed to produce the shallow ablation crater.

λ	$F_{th,R}(1)$	$F_{th,G}(1)$	ξ_R	ξ_G
513 nm	0.07 ± 0.02	0.17 ± 0.03	0.87 ± 0.02	0.82 ± 0.06
1026 nm	0.25 ± 0.03	0.61 ± 0.03	0.78 ± 0.04	0.77 ± 0.03

4.3.2   Static laser irradiation mode

In the static mode the target is irradiated at a fixed position by a sequence of N pulses, at a selected energy E, producing a shallow crater decorated with LIPSS. Here, we illustrate the morphological features of LIPSSs produced in the center of the craters and their dependence on number of pulses N and laser pulse peak fluence F_p. Moreover, the comparison of the observed trends between the two wavelengths is also considered.

Figure 4.7 (a) reports some examples of SEM images of the central region of the irradiated silicon surface registered at various values of N in the range 50 to 1000, at a laser pulse fluence $F_p = 0.4$ J/cm², for both wavelengths. Well-developed grooves are observed at both wavelengths for $50 \leq N \leq 500$. However, from the SEM images of Figure 4.7 (a), which display areas of the irradiated surface with a similar extension, one can also observe that at 1026 nm the grooves cover a smaller central area and are always surrounded by the ripples, meanwhile at 513 nm they extend over all the frame as a consequence of the much smaller threshold fluence for their formation at the visible wavelength.

Figure 4.7 (b) shows the variation of the grooves period Λ_G (symbols are experimental data) as a function of N for both wavelengths at a peak fluence $F_p = 0.4$ J/cm². As the exact value of Λ_G varies with the specific surface location in the grooved area, an average value of the period was estimated, and the observed variability is indicated as an error bar. The data of Figure 4.7(b) show that, at fixed peak fluence, Λ_G progressively increases with N. This observation results in good agreement with previous experimental findings [23,27] and theoretical predictions, as indicated by the solid lines [1]. Another interesting aspect is the dependence of the grooves period on the laser

wavelength [28]; in Figure 4.7 (b) we observe that the period of the grooves produced at 513 nm is always smaller than at 1026 nm, for the same number of pulses [25].
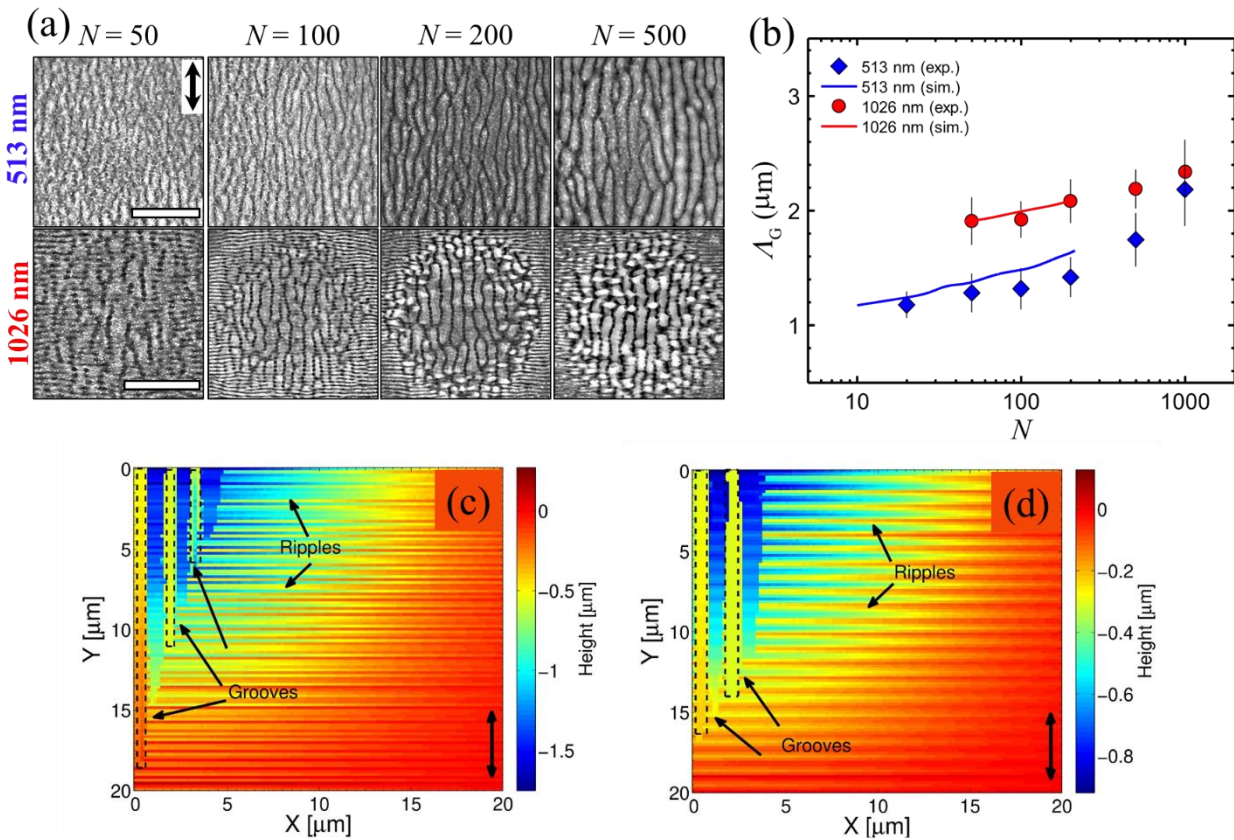

Figure 4.7 Panel (a) reports SEM images of central part of the ablation crater at both λ_{1026} and λ_{513}. for different values of the number of pulses N. The laser peak fluence $F_p = 0.4$ J/cm^2. The scale bars shown in the SEM images are 10 µm. the double headed arrow shows the laser beam polarization direction. Panel (b) shows the dependence of the grooves period Λ_G on the number of pulses N in the range 50÷500, for both λ_{1026} and λ_{513}. The symbols show the experimentally (exp.) and the two solid lines represent the trends predicted by the theoretical simulations (sim.). the simulation results of surface modification for $F_p \approx 0.4$ J/cm^2 for irradiation with $N = 60$ laser pulses are illustrated at (c) 513 nm and (d) 1026 nm.

Some simulations of the groove's formation process were carried out by George D. Tsibidis (Institute of Electronic Structure and Laser, FORTH) for conditions similar to those used in the experiment. Maps of the silicon target surface after irradiation with peak fluence of 0.4 J/cm^2 for $N = 60$ laser pulses for both 513 nm and 1026 nm obtained by the simulations are illustrated in Figure 4.7 (c) and (d). It is evident that ripples are also formed in the periphery of the irradiated area in both cases, but the coverage with grooves is enhanced at the smaller wavelength, in

agreement with the experimental findings of Figure 4.7 (a). Interestingly, the simulations also predict an increasing trend of the grooves period and an approximately similar rate of change on N as shown by solid lines in Figure 4.7(b). At 513 nm, the simulated values of the grooves period are slighlty larger than the experimental one, especially for larger N, whereas at 1026 nm they are within the experimental error. These differences can be likely due to progressive reduction of the experimental values for damage threshold and LIPSS formation with pulse number N due to incubation effects [25]. However, the fairly good agreement between the experimental findings and the simulation predictions at the two wavelengths suggest the significance of the underlying hydrothermal waves considered in the model for the generation of grooves.
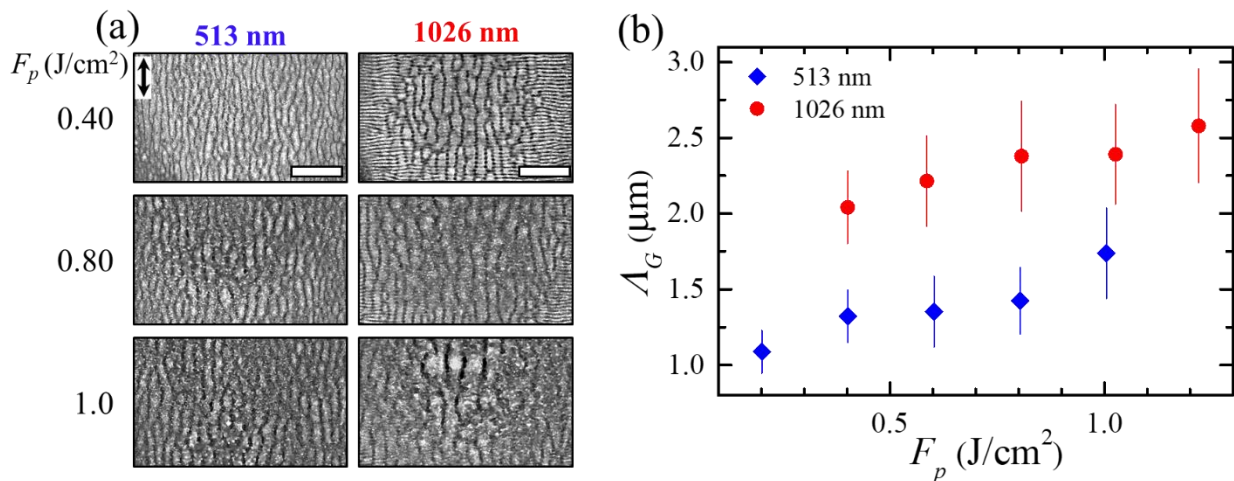

Figure 4.8 Panel (a) reports SEM images exemplifying the variation of the central part of the ablation crater at both λ_{1026} and λ_{513}. for three different values of the peak fluence F_p, as indicated on the left side of each image. The number of pulses is $N = 200$. The scale bars shown in the upper SEM images are 10 µm. The double headed arrow shows the direction of laser beam polarization. Panel (b) shows the variation of the grooves period Λ_G as a function of the peak fluence, for both wavelengths, as measured at $N = 100$ laser pulses, an experimental condition in which clear grooves are recognized at all the values of the laser fluence shown in the plot.

Figure 4.8 illustrates the variation of the grooves with the laser peak fluence F_p. Panel (a) of Figure 4.8 reports typical SEM images of the central part of the ablation crater at both λ_{513} and λ_{1026}. Here, for the sake of simplification, only three different values of the peak fluence F_p, at a pulse number $N = 200$, are shown. Panel (b) of Figure 4.8 shows the dependence of the grooves period Λ_G on the peak fluence F_p, for both wavelengths. The number of pulses $N = 100$ is considered here since it allows displaying more data points for the wavelength λ_{1026}, but a similar trend occurs

at $N = 200$ as well. At both wavelengths, Λ_G increases linearly with the laser peak fluence F_p [25], which seems in agreement with recent theoretical and experimental results on steel [6] but that deserve still theoretical confirmation for the case of silicon.

4.3.3   Scanning laser irradiation mode

The experimental performance for laser irradiation in dynamic mode aims at investigating the possibility of producing grooves by moving the silicon sample at different scan velocities. This achievement is important due to the industrial demands for large area laser processing.

Figure 4.9 shows the SEM images of the silicon surfaces under dynamic laser irradiation mode for both wavelengths. The fabrication of scanned lines was done using the same laser system of the static irradiation mode at a pulse repetition rate $f_p = 1$ kHz and a peak fluence $F_p = 0.4$ J/cm^2. Four different values of the scan speed v_s, namely $v_s = 1, 0.5, 0.25, 0.1$ mm/s, are selected. Due to the slight difference in the values of the laser spot diameter D for the two wavelengths, the number of overlapped pulses $N_O = D\, f_p/v_s$ have slightly different values, namely {78, 156, 312, 780} at 513 nm and {72, 144, 288, 720} at 1026 nm, corresponding to the scan speeds of {1, 0.5, 0.25, 0.1}, respectively.

Presence of supra-wavelength grooves, oriented parallel to the direction of laser polarization, is evident under irradiation with 513 nm for all four values of the scan speed (upper panels of Figure 4.9). From the SEM images we can observe a qualitative trend of increasing spatial period as the surface scan gets slower and the number of overlapped pulses increases. On the other hand, the scanned lines at 1026 nm (lower panels of Figure 4.9) display formation of well-developed grooves in conditions of higher overlapped pulse and lower scan speeds. In particular, presence of grooves at a scan speed of 1 mm/s (Figure 4.9 (a)) is not clearly recognizable as much as ripples. Moreover, slower scans result in thicker grooves (i.e. Figure 4.9 (h)). These observations are coherent with the variation of the surface structures on the pulse number N observed in static irradiation conditions in section 4.3.2.
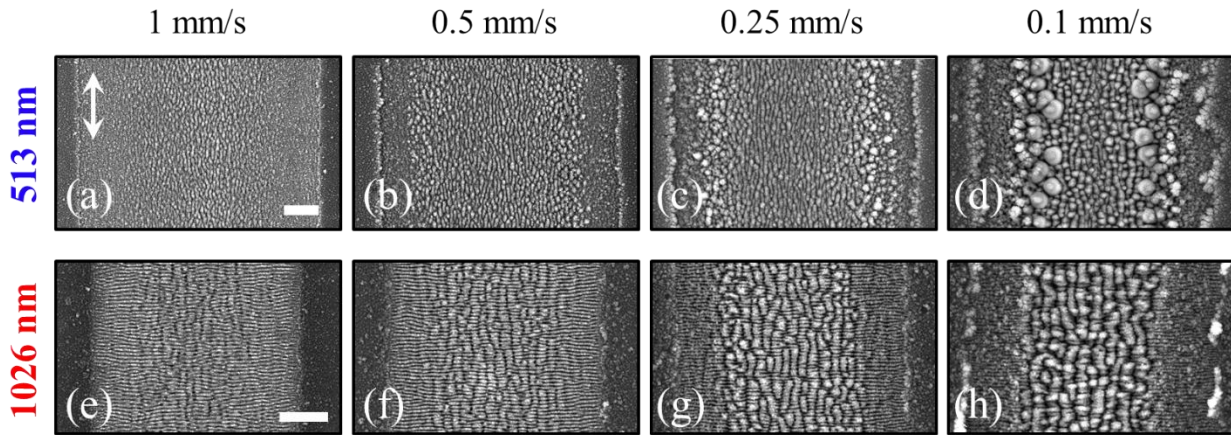
Figure 4.9 SEM images of the silicon surfaces after irradiation with laser peak fluence $F_p \approx 0.4$ J/cm^2 and repetition rate $f_p = 1$ kHz for four values of the scan speed v_s (e.g. $v_s = 1, 0.5, 0.25, 0.1$ mm/s), as indicated above each column. Panels (a-d) correspond to surface structuring with 513 nm, while panels (e-h) with 1026 nm, respectively. The number of overlapped pulses, N_O is: (a) 78; (b) 156; (c) 312; (d) 780; (e) 72; (f) 144; (g) 288; (h) 720. The scale bar is equal to 10 µm. The double-headed arrow in panel (a) shows the laser polarization direction for all panels.

Figure 4.10 reports a direct morphological comparison of fine structures formed in the central region of craters between static and scanning laser irradiation with laser peak fluence of $F_p = 0.4$ J/cm^2 for each laser wavelengths. The upper images in both panels (Fig. 4.10 (a) and (b)) display SEM images of the craters in static condition after irradiation with a sequence of $N = 200$ laser pulses for 513 nm and 1026 nm. While, the lower SEM images show the lines obtained with scan speed of 0.25 mm/s at 513 nm and 1026 nm. For all cases, zoomed views are shown on the sides in dashed boxes. These images confirm that the general characteristics of the irradiated surface are rather similar in the two experimental conditions. In fact, in both modes of irradiation, at 513 nm (see Figure 4.10 (a)) a central grooved region is surrounded by the region covered with rudiment of grooves, while at 1026 nm (see Figure 4.10 (b)) grooves and ripples cover the central and outer regions, respectively. The similarities of morphologies in static and dynamic conditions suggest that a similar formation mechanism for grooves generation: the energy redistribution induced by the electromagnetic mechanisms is related to the generation of surface scattered waves induced by the sample roughness and by the already formed ripples [4,5].

However, the zoomed views of Figure 4.10 show some differences in the finer morphological features of the structures. In particular, the grooves show a larger granularity in the scanning regime at 513 nm and a more evident underlying layer of ripples at 1026 nm. These characteristics

can be likely associated to the fact that while with static irradiation each point of the surface receives the same amount of laser fluence in each shot, in scanning mode the local value of the fluence varies continuously with the laser shot (or time) [25].
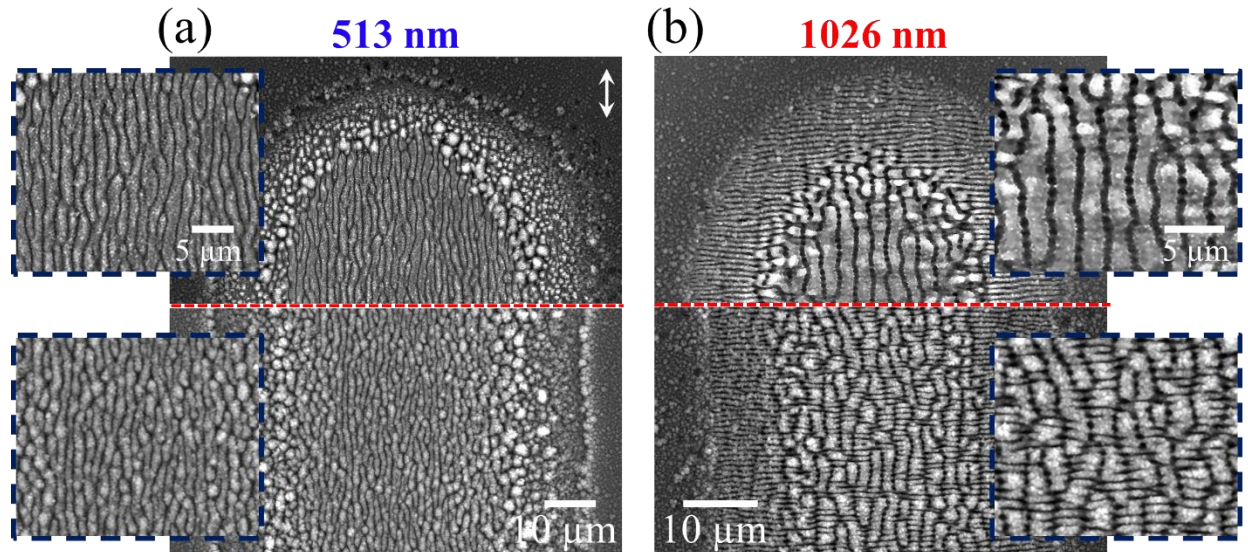

Figure 4.10 Comparison of the surface structures for static and dynamic irradiation conditions at the two wavelengths: (a) 513 nm; (b) 1026 nm. In both cases the laser peak fluence is $F_p = 0.4$ J/cm^2. The upper SEM images refer to static irradiation conditions with a number of pulses $N = 200$. The lower SEM images refer to dynamic irradiation conditions for a scan speed v_s of 0.25 mm/s, corresponding to a number of overlapped pulses N_O of 312 at 513 nm and 288 at 1026 nm, (b) 1026 nm. The images in dashed boxes next to each image shows the zoomed views. The scale bar in full views are 10 µm and in zoomed views 5 µm. The double headed arrow in panel (a) shows the laser polarization direction.

4.4   Effect of ambient pressure on formation of grooves

In previous sections, we have seen that the irradiation conditions play a crucial role on the formation of LIPSSs; however, mechanisms of surface structures formation are still debated. Zayats et al. reported that scattering of surface plasmon polaritons (SPPs) can result from surface roughness [29]. Therefore, the next laser pulses combine with the SPPs of previous produced nanostructures which causes a periodic spatial modulation of energy onto the surface irradiated by a linearly polarized laser beam [3,30]. The surrounding media is another parameter influencing the morphological features of LIPSS. Apart from air which is the most common ambient in which the surface structures are produced, already discussed in previous sections, several studies considered the case of liquid environment [31–33], but very few investigated the development of LIPSS in

high vacuum or at variable ambient air pressure. JJ Nivas et al. [34] performed studies on the formation of LIPSS in high vacuum condition ($\approx 10^{-5}$ mbar) in order to minimize the presence of redeposited nanoparticles on the ablated crater. They have reported the comparison of morphological features of LIPSS in atmospheric and vacuum pressures [34–36].

In this section, the effect of variation of the ambient air pressure on the spatial period of ripples, formation of grooves and shape of the craters is analyzed. Moreover, the effects of various states of polarization in vacuum as well as of circularly polarized pulses in air vs vacuum are also addressed. In these experiments the silicon target is positioned on a XY-translation stage inside a vacuum chamber and irradiated using a Nd: Glass laser system delivering linearly polarized ≈ 900 fs pulses at 1055 nm at a repetition rate of 33 Hz, with a Gaussian spatial profile. An electromechanical shutter provides the selection of the desired number of laser pulses, N, applied to the same spot on the target. Experiments are carried out in the residual air pressure going from atmospheric pressure to high vacuum, at a base pressure of $\approx 10^{-4}$ mbar. The beam focal spot radius on the target is determined by measuring the energy variation of the ablation crater dimensions [37], resulting in $w_0 = (130 \pm 5)$ µm.

4.4.1   Effect of pressure variation

Figure 4.11 reports SEM and AFM images of the ripples on silicon surfaces produced at various pressures p. The sample was irradiated at a peak fluence of ≈ 0.3 J/cm^2.

Figure 4.11 (a) and (b) are exemplificative images of ripples produced in different pressure conditions for $N = 100$. They address a variation of the spatial period Λ and depth δ of ripples with the pressure p. The data are summarized in table 4-2. δ was estimated by evaluating the maximum peak-to-valley height (by using the image processing software Gwyddion). The measured data show a strong dependence of the ripples' period Λ on p with a reduction of Λ and a corresponding increase of δ as p raises to higher values. Moreover, the ripples generated in vacuum present a larger average period, a wider characteristic thickness, and a narrower separation with respect to air [38] .
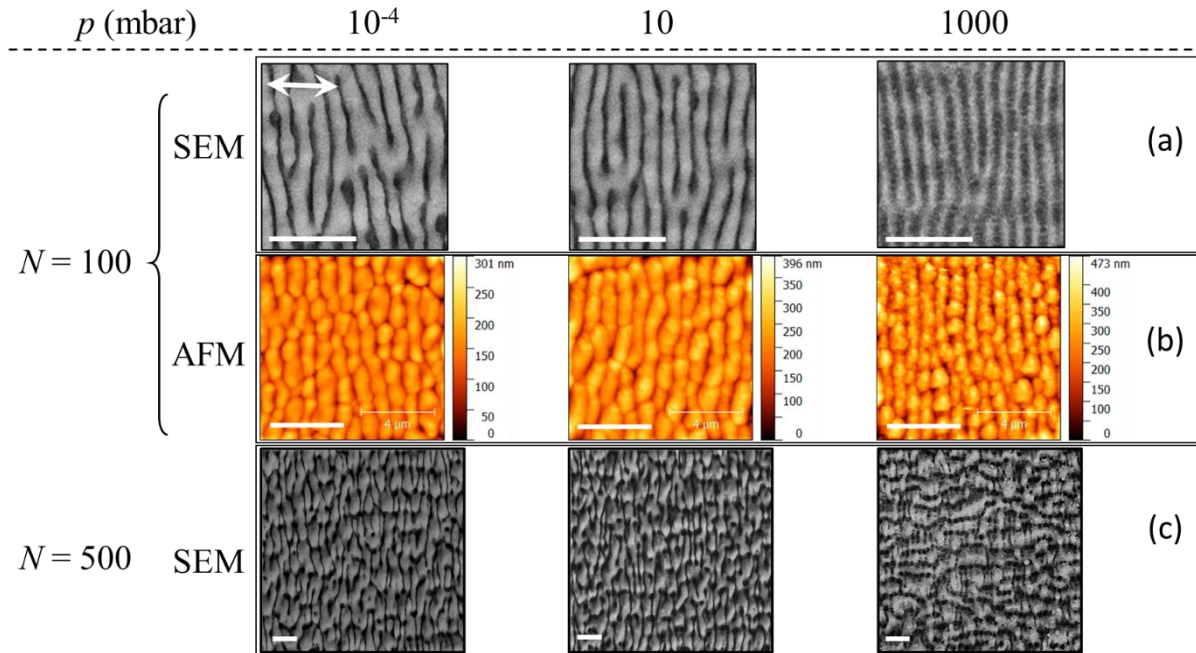
Figure 4.11 Examples of SEM and AFM images for a peak fluence of ≈ 0.3 J/cm^2 and various values of the pressure p of (a) and (b) the ripples generated by irradiation with $N = 100$ laser pulses and (c) the central region of the targets irradiated with $N = 500$ laser pulses. The scale bar in each panel is 4 µm. The double-headed arrow in the upper left panel shows the direction of the laser polarization

Panel (c) of Figure 4.11 illustrates the SEM images of the central region of the crater at $N = 500$ pulses and for various pressure conditions. At atmospheric pressure, $p = 1000$ mbar, the typical grooves with a preferential orientation parallel to the laser polarization are observed. However, at the lower pressures of 10 mbar and 10^{-4} mbar the central region of the irradiated spot presents rather different morphological features with respect to the grooves observed at atmospheric pressure.

Table 4-2 Values of the ripples period Λ obtained by SEM and AFM analyses and depth δ measured by AFM. As the values of the measured parameters varies with spatial location, the data are given as estimated mean value and standard deviation.

p (mbar)	SEM	AFM	
	Λ (nm)	Λ (nm)	δ (nm)
10^{-4}	918 ± 58	964 ± 69	91 ± 4
10	866 ± 45	933 ± 40	139 ± 7
1000	785 ± 38	796 ± 46	216 ± 12

In high vacuum conditions, the surface texture shows a kind of multicellular patterns formed by elemental components with a length varying in the range of few to tens of μm and showing a preferential elongation in the direction normal to the laser polarization. This suggests that their formation should result from a merging of two or more adjacent ripples induced by the higher value of the fluence in the central region of the laser beam spot and the iterated irradiation. The fact that grooves do not form at reduced pressure suggests a possible important role of nanoparticles in the formation of these supra-wavelength surface structures. In fact, at atmospheric pressure the ablated nanoparticles get re-deposited on the sample surface and influence the formation of surface structures. As the pressure is lower, the ablated material is less confined with a reduction of re-deposition of ablated particles that more easily fly away from the target surface [38,39]. As for the ripples under high vacuum pressure, the anti-correlation between period and depth of ripples results from slightly changes in effective refractive index of the surface due to different modification of nanoparticles. This effect is shown in Figure 4.12: in air, a rim of aggregated nanoparticles is visible around the structured area (Figure 4.12 (c) and its zoomed view in Figure 4.12 (d)); in vacuum, such an effect seems almost negligible (Figure 4.12 (a) zoomed view in Figure 4.12 (b)) The disappearance of the grooves at lower pressure and the simultaneous sizeable reduction of the nanoparticles seem in fairly good agreement with Sipe–Drude theory for a rough surface, further addressing the nanoparticulate as a key factor for grooves generation, besides any possible other hydrodynamic mechanism [40,41] or the possible influence of ambient oxygen.

Figures 4.12 (a) and (c) highlight the variation of size and crater shape from circle to elliptic as the pressure goes down from vacuum to air. In vacuum, $p = 10^{-4}$ mbar, the spot turns to more oval shape along the direction of laser beam polarization. The plot in Figure 4.12 (e) which is the ratio between minor and major diameter vs pressure p, clarifies that craters at lower number of pulses N and pressure p are more elliptic. The different size can likely result from an enhanced absorption associated with the rougher developing surface in air. In fact, the dense coverage with nanoparticles and nanostructures generated by multi-pulse fs laser irradiation progressively modifies the surface absorption properties [39].
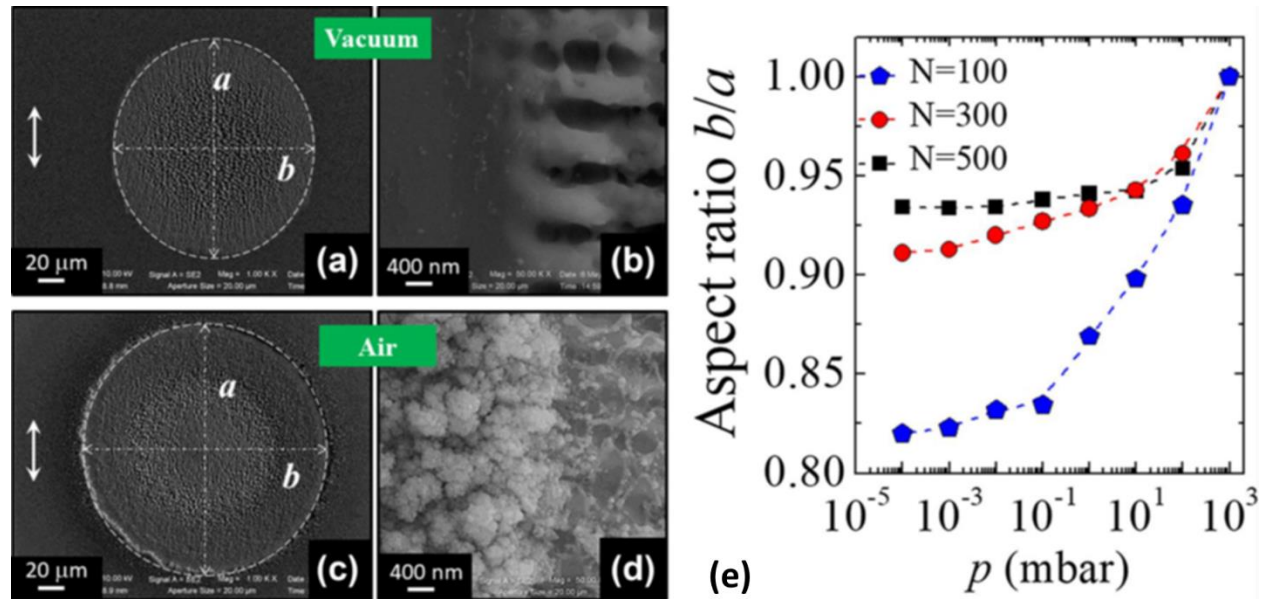
Figure 4.12 Panels (a) and (c) report SEM images of the surface structured area ($N = 300$ laser pulses, peak fluence ≈ 0.3 J/cm^2) in vacuum ($p \approx 10^{-4}$ mbar) and air illustrating the effect of the pressure on its shape and size. Panels (b) and (d) are zoomed views evidencing the different nanoparticles coverage at the edge of the structured area in the two cases. Panel (e) reports the variation of the aspect ratio b/a as a function of the pressure for various number of pulses N. The double headed arrow in the panels (a) and (b) shows the direction of the laser polarization.

4.4.2   Effect of the laser polarization under vacuum condition

Further investigations on the effect of the state of laser polarization on the shape of crater and features of the fine structures have been done. Figure 4.13 reports the SEM images of ablated craters comparing four different states of polarization of the laser beam produced by means of waveplates (half or quarter for linear and circular polarization, respectively) in low pressure of 10^{-4} mbar. Vertical and horizontal linear polarizations result in elliptical craters with the major axes following the laser beam polarization (panels (a) and (b) of Figure 4.13). The zoomed views of panels (a) and (b), in dashed yellow boxes on their sides, display the presence of ripples on the edges of the craters. In case of vertical laser polarization (panel (b)), it is evident that the formation of ripples ends abruptly, and this side of the crater is parallel to the polarization. On the other hand, in panel (a), the rippled regions protruding outwards along the polarization direction can be due to generation of surface-scattered electromagnetic waves (SSW) favoured by ripples grating and surface roughness. The interference of the SSW with the low-energy tail of the laser beam can favor the formation of the rippled protrusions also in peripheral areas in which the laser beam alone

would not exceed the threshold fluence for the creation of surface structures at that number of pulses. This, in turn, should explain the development of the elliptically shaped spot with major axis directed along the laser polarization, as observed experimentally [35,39].
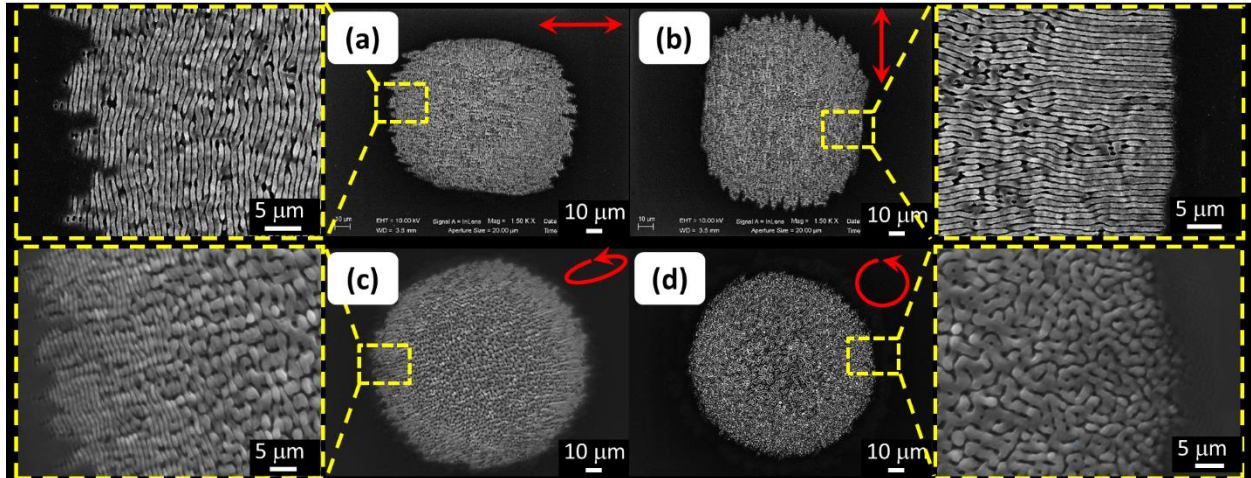

Figure 4.13 SEM images of the surface structures produced in vacuum ($p \sim 10^{-4}\ mbar$) with various state of polarizations. Panels (a) and (b) show images of the spot produced with (a) horizontal and (b) vertical linear polarization ($N = 200$ pulse at a fluence of ≈ 0.25 J/cm^2). Panels (c) and (d) report images of the spot produced with (c) elliptical and (d) circular polarizations ($N = 300$ pulse at a fluence of ≈ 0.3 J/cm^2), respectively. The images in the yellow dashed boxes show zoomed views of the spot edge illustrating the surface structures formed by the different states of polarization.

Elliptical polarization (Figure 4.13 (c)) results in a nearly-circular spot only slightly longer in the direction of the prevailing axis of the polarization ellipse. Moreover, ripples directed along the normal to the prevailing linear component of the elliptically polarized beam are formed at the periphery of the spot. Instead, the circular polarization (Figure 4.13 (d)) produces an almost circular spot with a texture resembling a tangle of randomly oriented elements. Moreover, the central region of the spots is characterized by a pattern composed of coarser elemental constituents with respect to those present at the edges. This can likely result from thermal fusion processes (coalescence) of two or more elemental structures in the region of higher laser fluence.

The outputs of the above-mentioned experiments suggest a crucial role of the ambient pressure on the development of surface structures. The results highlight that as the pressure raises the ablated nanoparticles produced during the fs laser ablation process of the target get deposited more and

more on the sample surface covering the irradiated spot area and influencing the structuring process and possibly the formation of grooves.

References

[1]   G.D. Tsibidis, C. Fotakis, E. Stratakis, From ripples to spikes: A hydrodynamical mechanism to interpret femtosecond laser-induced self-assembled structures, Phys Rev B - Condens Matter Mater Phys. 92 (2015) 1–6. https://doi.org/10.1103/PhysRevB.92.041405.

[2]   J. Bonse, S. Hohm, S. V. Kirner, A. Rosenfeld, J. Kruger, Laser-Induced Periodic Surface Structures-A Scientific Evergreen, IEEE J Sel Top Quantum Electron. 23 (2017). https://doi.org/10.1109/JSTQE.2016.2614183.

[3]   A.Y. Vorobye, C. Guo, Direct femtosecond laser surface nano/microstructuring and its applications, Laser Photon Rev. 7 (2012) 385–407. https://doi.org/10.1002/lpor.201200017.

[4]   S. He, J.J. Nivas, K.K. Anoop, A. Vecchione, M. Hu, R. Bruzzese, S. Amoruso, Surface structures induced by ultrashort laser pulses: Formation mechanisms of ripples and grooves, Appl Surf Sci. 353 (2015) 1214–1222. https://doi.org/10.1016/j.apsusc.2015.07.016.

[5]   S. He, J. JJ Nivas, A. Vecchione, M. Hu, S. Amoruso, On the generation of grooves on crystalline silicon irradiated by femtosecond laser pulses, Opt Express. 24 (2016) 3238–3247. https://doi.org/10.1364/OE.24.003238.

[6]   G.D. Tsibidis, A. Mimidis, E. Skoulas, S. V. Kirner, J. Krüger, J. Bonse, E. Stratakis, Modelling periodic structure formation on 100Cr6 steel after irradiation with femtosecond-pulsed laser beams, Appl Phys A Mater Sci Process. 124 (2018). https://doi.org/10.1007/s00339-017-1443-y.

[7]   R. Le Harzic, D. Dörr, D. Sauer, M. Neumeier, M. Epple, H. Zimmermann, F. Stracke, Large-area, uniform, high-spatial-frequency ripples generated on silicon using a nanojoule-femtosecond laser at high repetition rate, Opt Lett. 36 (2011) 229. https://doi.org/10.1364/ol.36.000229.

[8]   A. Gruner, J. Schille, U. Loeschner, Experimental study on micro hole drilling using ultrashort pulse laser radiation, Phys Procedia. 83 (2016) 157–166. https://doi.org/10.1016/j.phpro.2016.08.030.

[9]   G. Kamlage, T. Bauer, A. Ostendorf, B.N. Chichkov, Deep drilling of metals by femtosecond laser pulses, Appl Phys A Mater Sci Process. 77 (2003) 307–310. https://doi.org/10.1117/12.482108.

[10]   X. Sedao, M. Lenci, A. Rudenko, A. Pascale-Hamri, J.P. Colombier, C. Mauclair, Additive and substractive surface structuring by femtosecond laser induced material ejection and redistribution, Materials (Basel). 11 (2018) 2456. https://doi.org/10.3390/ma11122456.

[11] R. Weber, T. Graf, P. Berger, V. Onuseit, M. Wiedenmann, C. Freitag, A. Feuer, Heat accumulation during pulsed laser materials processing: erratum, Opt Express. 22 (2014). https://doi.org/10.1364/OE.22.011312.

[12] X. Sedao, M. Lenci, A. Rudenko, N. Faure, A. Pascale-Hamri, J.P. Colombier, C. Mauclair, Influence of pulse repetition rate on morphology and material removal rate of ultrafast laser ablated metallic surfaces, Opt Lasers Eng. 116 (2019) 68–74. https://doi.org/10.1016/j.optlaseng.2018.12.009.

[13] G. Raciukaitis, M. Brikas, P. Gecys, M. Gedvilas, Accumulation effects in laser ablation of metals with high-repetition-rate lasers, SPIE Proceedings, High-Power Laser Ablation VII. 7005 (2008) 70052L. https://doi.org/10.1117/12.782937.

[14] E. Allahyari, J.J.J. Nivas, M. Valadan, R. Fittipaldi, A. Vecchione, L. Parlato, R. Bruzzese, C. Altucci, S. Amoruso, Plume shielding effects in ultrafast laser surface texturing of silicon at high repetition rate in air, Appl Surf Sci. 488 (2019) 128–133. https://doi.org/10.1016/j.apsusc.2019.05.219.

[15] A. Ancona, K. Rademaker, F. Röser, J. Limpert, S. Nolte, A. Tünnermann, Laser drilling using a high repetition rate and high average power femtosecond fiber CPA system, Opt InfoBase Conf Pap. 16 (2008) 593–596. https://doi.org/10.1109/CLEO.2008.4551313.

[16] S.M. Eaton, H. Zhang, P.R. Herman, F. Yoshino, L. Shah, J. Bovatsek, A.Y. Arai, Heat accumulation effects in femtosecond laser-written waveguides with variable repetition rate, Opt Express. 13 (2005) 4708. https://doi.org/10.1364/opex.13.004708.

[17] I. Gnilitskyi, V. Gruzdev, N.M. Bulgakova, T. Mocek, L. Orazi, Mechanisms of high-regularity periodic structuring of silicon surface by sub-MHz repetition rate ultrashort laser pulses, Appl Phys Lett. 109 (2016) 143101. https://doi.org/10.1063/1.4963784.

[18] M.E. Povarnitsyn, T.E. Itina, M. Sentis, K. V. Khishchenko, P.R. Levashov, Material decomposition mechanisms in femtosecond laser interactions with metals, Phys Rev B. 75 (2007) 235414. https://doi.org/10.1103/PhysRevB.75.235414.

[19] P. Lorazo, L.J. Lewis, M. Meunier, Thermodynamic pathways to melting, ablation, and solidification in absorbing solids under pulsed laser irradiation, Phys Rev B. 73 (2006) 134108. https://doi.org/10.1103/PhysRevB.73.134108.

[20] S. Amoruso, R. Bruzzese, N. Spinelli, R. Velotta, M. Vitiello, X. Wang, G. Ausanio, V. Iannotti, L. Lanotte, Generation of silicon nanoparticles via femtosecond laser ablation in vacuum, Appl Phys Lett. 84 (2004) 4502–4504. https://doi.org/10.1063/1.1757014.

[21] N. Tsakiris, K.K. Anoop, G. Ausanio, M. Gill-Comeau, R. Bruzzese, S. Amoruso, L.J. Lewis, Ultrashort laser ablation of bulk copper targets: Dynamics and size distribution of the generated nanoparticles, J Appl Phys. 115 (2014). https://doi.org/10.1063/1.4885196.

[22] E. Allahyari, J.J. Nivas, G. Avallone, M. Valadan, M. Singh, V. Granata, C. Cirillo, A. Vecchione, R. Bruzzese, C. Altucci, S. Amoruso, Femtosecond laser surface irradiation of

silicon in air: pulse repetition rate influence on removal efficiency and surface texture, Submitted. (n.d.).

[23]   J.J. Nivas, K.K. Anoop, R. Bruzzese, R. Philip, S. Amoruso, Direct femtosecond laser surface structuring of crystalline silicon at 400 nm, Appl Phys Lett. 112 (2018) 121601. https://doi.org/10.1063/1.5011134.

[24]   F. Fraggelakis, G. Mincuzzi, J. Lopez, I. Manek-Hönninger, R. Kling, Controlling 2D laser nano structuring over large area with double femtosecond pulses, Appl Surf Sci. 470 (2019) 677–686. https://doi.org/10.1016/j.apsusc.2018.11.106.

[25]   E. Allahyari, J.J. Nivas, E. Skoulas, R. Bruzzese, G.D. Tsibidis, E. Stratakis, S. Amoruso, On the formation and features of the supra-wavelength grooves generated during femtosecond laser surface structuring of silicon, Manuscr under Prep to Submit J Appl Surf Sci. (2020).

[26]   J. Bonse, S. Baudach, J. Krüger, W. Kautek, M. Lenzner, Femtosecond laser ablation of silicon-modification thresholds and morphology, Appl Phys A. 74 (2002) 19–25. https://doi.org/10.1007/s003390100893.

[27]   J.J.J. Nivas, S. He, A. Rubano, A. Vecchione, D. Paparo, L. Marrucci, R. Bruzzese, S. Amoruso, Direct Femtosecond Laser Surface Structuring with Optical Vortex Beams Generated by a q-plate, Sci Rep. 5 (2015) 17929. https://doi.org/10.1038/srep17929.

[28]   G.D. Tsibidis, E. Skoulas, A. Papadopoulos, E. Stratakis, Convection roll-driven generation of supra-wavelength periodic surface structures on dielectrics upon irradiation with femtosecond pulsed lasers, Phys Rev B. 94 (2016) 081305(R). https://doi.org/10.1103/PhysRevB.94.081305.

[29]   A. V. Zayats, I.I. Smolyaninov, Near-field photonics: Surface plasmon polaritons and localized surface plasmons, J Opt A Pure Appl Opt. 5 (2003). https://doi.org/10.1088/1464-4258/5/4/353.

[30]   A.Y. Vorobyev, V.S. Makin, C. Guo, Periodic ordering of random surface nanostructures induced by femtosecond laser pulses on metals, J Appl Phys. 101 (2007). https://doi.org/10.1063/1.2432288.

[31]   S. Bashir, M.S. Rafique, C.S. Nathala, A.A. Ajami, W. Husinsky, Femtosecond laser fluence based nanostructuring of W and Mo in ethanol, Phys B Condens Matter. 513 (2017) 48–57. https://doi.org/10.1016/j.physb.2017.03.008.

[32]   R. Kuladeep, M.H. Dar, K.L.N. Deepak, D.N. Rao, Ultrafast laser induced periodic sub-wavelength aluminum surface structures and nanoparticles in air and liquids, J Appl Phys. 116 (2014). https://doi.org/10.1063/1.4896190.

[33]   C. Albu, A. Dinescu, M. Filipescu, M. Ulmeanu, M. Zamfirescu, Periodical structures induced by femtosecond laser on metals in air and liquid environments, Appl Surf Sci. 278 (2013) 347–351. https://doi.org/10.1016/j.apsusc.2012.11.075.

[34] J.J.J. Nivas, Z. Song, R. Fittipaldi, A. Vecchione, R. Bruzzese, S. Amoruso, Direct ultrashort laser surface structuring of silicon in air and vacuum at 1055 nm, Appl Surf Sci. 417 (2017) 149–154. https://doi.org/10.1016/j.apsusc.2017.03.158.

[35] F. Gesuele, J. JJ Nivas, R. Fittipaldi, C. Altucci, R. Bruzzese, P. Maddalena, S. Amoruso, Analysis of nascent silicon phase-change gratings induced by femtosecond laser irradiation in vacuum, Sci Rep. 8 (2018) 0–10. https://doi.org/10.1038/s41598-018-30269-0.

[36] F. Gesuele, J.J.J. Nivas, R. Fittipaldi, C. Altucci, R. Bruzzese, P. Maddalena, S. Amoruso, Multi-imaging analysis of nascent surface structures generated during femtosecond laser irradiation of silicon in high vacuum, Appl Phys A Mater Sci Process. 124 (2018). https://doi.org/10.1007/s00339-018-1633-2.

[37] J.M. Liu, Simple technique for measurements of pulsed Gaussian-beam spot sizes, Opt Lett. 7 (1982) 196. https://doi.org/10.1364/OL.7.000196.

[38] J. JJ Nivas, F. Gesuele, E. Allahyari, S.L. Oscurato, R. Fittipaldi, A. Vecchione, R. Bruzzese, S. Amoruso, Effects of ambient air pressure on surface structures produced by ultrashort laser pulse irradiation, Opt Lett. 42 (2017) 2710. https://doi.org/10.1364/ol.42.002710.

[39] J. JJ Nivas, E. Allahyari, F. Gesuele, P. Maddalena, R. Fittipaldi, A. Vecchione, R. Bruzzese, S. Amoruso, Influence of ambient pressure on surface structures generated by ultrashort laser pulse irradiation, Appl Phys A. 124 (2018) 198. https://doi.org/10.1007/s00339-018-1621-6.

[40] J. Bonse, M. Munz, H. Sturm, Structure formation on the surface of indium phosphide irradiated by femtosecond laser pulses Structure formation on the surface of indium phosphide irradiated by femtosecond laser pulses, J Appl Phys. 97 (2005) 013538. https://doi.org/10.1063/1.1827919.

[41] J.E. Sipe, J.F. Young, J.S. Preston, H.M. van Driel, Laser-induced periodic surface structure. I. Theory, Phys Rev 8. 27 (1983). https://doi.org/https://doi.org/10.1117/12.950633.

5 Laser surface texturing on different target materials

Abstract – Examples of surface pattering, by means of target scanning mode, aiming at using fs laser irradiation to add functional response to the sample are presented. In the previous chapters, the experiments were carried out on silicon, which offers a crystalline substrate, whereas here metallic, thin films and wide band-gap semiconductor samples are used as target. The first example concerns large area laser scanned surfaces of copper showing interesting capability of controlling the wetting behavior. The second one makes use of thin gold films over a silicon substrate to fabricate patterned samples as suitable candidates as metasurfaces for THz radiation. The third one, CdZnTe, shows the presence of cracks as well as the formation of both LSFL and HSFL and can be interesting for optoelectronics applications.

5.1 Introduction

This thesis is principally focused on irradiation of solid surfaces with fs laser pulses. So far, the previous chapters dealt with the effects of laser irradiation of silicon and formation of LSFL. This last chapter reports few examples of preliminary work carried out in the frame of the present thesis on surface structuring with laser beam scanning approaches to pattern various target materials, such as pure metal and thin films, with a glance towards applications. Direct fs laser structuring can offer advantages for industries being non-contact, applicable to a wide range of materials (metals, semiconductors, polymers, etc.) and without processing environment limitation, like high-vacuum or clean room facilities. Applications can be found in the possibility of changing surface roughness or even surface topography that can impart or modify the functional response of the samples.

In the first example (Section 5.2), pure copper plate is considered as target. The investigation regards a study of the relationship between surface structures induced by changing the laser beam fluence and the wetting response to water of the produced surfaces. It is shown that the combination of the microscale trenches, written by laser line scanning, ripples and random nanoparticles decoration, formed on the surface, allow developing highly hydrophobic copper samples with contact angles reaching values around 160°.

In the second case (Section 5.3), a gold thin film deposited on a silicon substrate is used as target. An array of periodic patterns is fabricated by means of direct fs laser ablation and their response in the THz spectral range is analyzed with the aim to clarify if the approach can be suitable for the fabrication of THz metasurfaces. The unit cells of these patterns are composed of through-holes or metallic islands in this proof of principle experiments. The response of the resulting structures is characterized using THZ Time-Domain Spectrometry in the frequency range (0.3-1.5) THz.

In the third case (Section 5.4), a wide band-gap semiconductor, namely CdZnTe, was considered. The preliminary investigation involves the static laser irradiation with a sequence of fs laser pulses and the observation of the surface modifications induced. The results showed different types of surface structures depending on the experimental conditions (pulse number and fluence). These structures can be cracks, LSFL and HSFL.

5.2   Copper and wettability

The control of surface roughness is a useful method to regulate the degree of wetting. Depending on the applications, the surface response can vary from hydrophobic to hydrophilic, when water is used as a measuring liquid. Direct interaction of linearly polarized laser beam with a metallic surface generally leads to formation of subwavelength ripples and decoration with nanoparticles [1–4]. Larger scales ordering can be also added by appropriate laser beam scanning procedures.

Here, large area surface patterns composed by micro-trenches were generated on copper foils (thickness 1 mm) by means of bidirectional laser scanning. The line width of each micro-trench is ≈50 µm and the depth is varied by using different laser peak fluence. The laser irradiation also causes the formation of sub-wavelength ripples and the redeposition of ablated nanoparticles. Measurements of the contact angle of water droplet is carried out to highlight the correlation between the wetting degree and the morphological features of the treated copper surfaces.

Linearly polarized pulses with a pulse duration of ≈35 fs were provided by a Ti:Sa laser source operating at central wavelength of 800 nm and repetition rate of 1 kHz. The laser beam was focused by a plano-convex lens with a focal length of 75 mm. The target was positioned at the laser beam

focal plane and held on a high-precision XYZ translation stage (PPS-20, Micronix USA) allowing its scanning. The resulting focal spot diameter, at $1/e^2$ of the maximum laser pulse fluence, was estimated to be $D \approx 50$ μm. The copper plates were first polished by micro-grit finishing papers with a mechanical polishing machine and then made mirror-like by means of an ultra-fine 0.5 μm diamond powder. AFM analysis of the target surface indicated a RMS roughness of ≈10 nm.

The large area scanned surfaces were prepared by bidirectional continuous line scanning at scan speed of 1 mm/s, in air. The vertical step between lines was selected to be comparable to the laser beam diameter D, i.e. $\Delta y = 50$ μm (see inset in Figure 5.1(a)). The number of overlapping pulses was $N_O = 50$. Several samples were fabricated for different values of the laser beam energy,E_L, in the range (10–100) μJ, with corresponding values of the peak fluence $F_p = (8E_L)/(\pi D^2)$ ranging from ≈ 0.8 J/cm^2 to ≈ 8 J/cm^2. The current experiment [5] is designed not only to evaluate the wettability of the structured substrates but also to study decoration of redeposited nanoparticles and features of ripples, which are known to be conditioned by the target properties, laser characteristics and scanning speed [6–8]. Instead, it is seen that the period of ripples formed on copper target does not change significantly as the number of pulses and laser fluence changes, in our experimental conditions [9].

The topographic measurements were registered by AFM and profilometry over the full area of structured copper samples. Figure 5.1 reports a typical example of a micro-scale surface pattern for a sample elaborated at a laser peak fluence of $F_p = 2.4$ J/cm^2 as registered by an optical microscope (panel (a)) and by AFM (panel (b)), respectively. Horizontal parallel lines with a period of about 50 μm are clearly visible. The height profiles along a single AFM line and averaged over several AFM lines are registered along the dotted line of panel (b). The AFM and profilometry analyses confirm that the long-range height variation approximately follows a sinusoidal dependence [5]. Panel (c) of Figure 5.1 displays the dependence of the micro-trenches' height h on the laser peak fluence F_p. At each laser fluence, h is estimated by averaging values of the peak-to-valley distance of successive micro-trenches registered by a profilometer over a length of about 500 μm. One can observe that the height of the micro-trench h shows a double logarithmic dependence of the type $h = h_0 ln\left(F_p/F_{p,th}\right)$ with two different regimes, similarly to that typically

observed for ablation depth variation on pulse fluence of copper samples in static irradiation conditions [10–12].
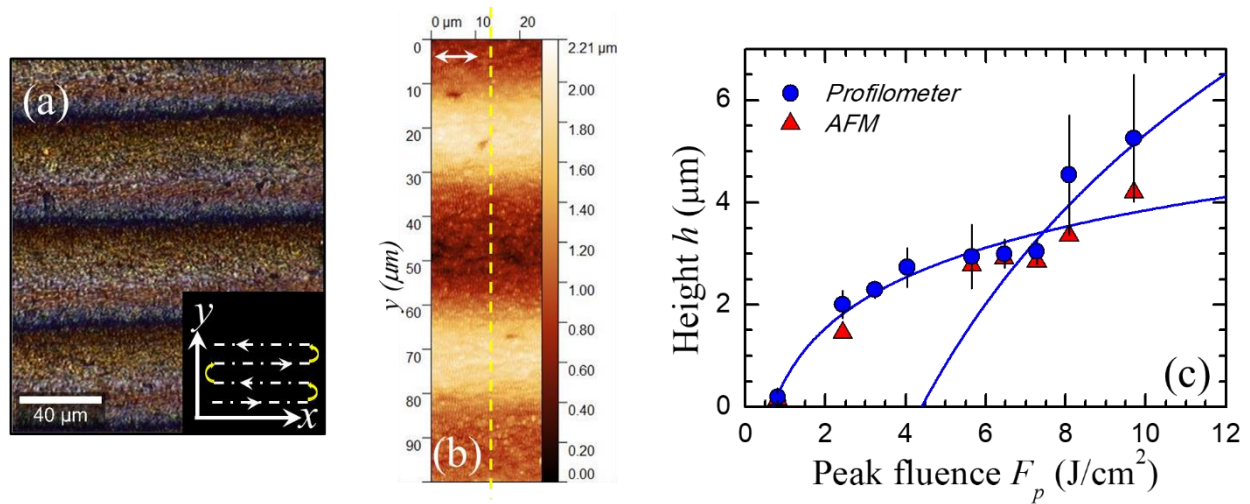

Figure 5.1 Panel (a) reports a typical optical microscope image of the copper sample surface showing the parallel micro-trenches inscribed on the target surface by the bidirectional scanning of the laser beam, as depicted in the right-corner inset. Panel (b) reports an example of AFM image of the sample surface. The double-headed arrow in panel (b) indicates the laser beam polarization. Panel (c) shows the variation of the micro-trenches height (full dots) as a function of the laser peak fluence F_p as registered by a profilometer. The solid curves are logarithmic dependences of the type $h = h_0 ln(F_p/F_{p,th})$ addressing the two different ablation regimes of fs laser ablation of a metallic target. The triangles are estimates of the micro-trenches heights obtained by AFM analysis. The AFM height profile registered along the dotted line in panel (a).

Figure 5.2 reports an exemplificative SEM image of the sample obtained at a laser peak fluence of $F_p = 2.4$ J/cm^2. Panel (a) shows the substrate surface with micro-trenches. An image at higher magnification is shown in panel (b) with zoomed views on two regions, *inside* (panels (c) and (e)), and *outside* (panels (d) and (f)) the trench. The two regions have thicknesses of ≈24 μm and ≈27 μm, respectively. In both regions, the presence of sub-wavelength ripples can be clearly recognized. Inside, the trenches are covered by ripples with a period of (660 ± 70) nm and nanoparticles with diameters in the range of couple of hundreds nm. The ripples formed outside of the trenches seem to be mainly composed by assemblies of nanoparticles organized along a direction normal to the laser polarization. This is likely due to the effect of the Gaussian beam wings that are not intense enough to induce ablation but are capable of influencing the spatial arrangement of the nanoparticles deposited out of the main ablated region during the laser scanning process.
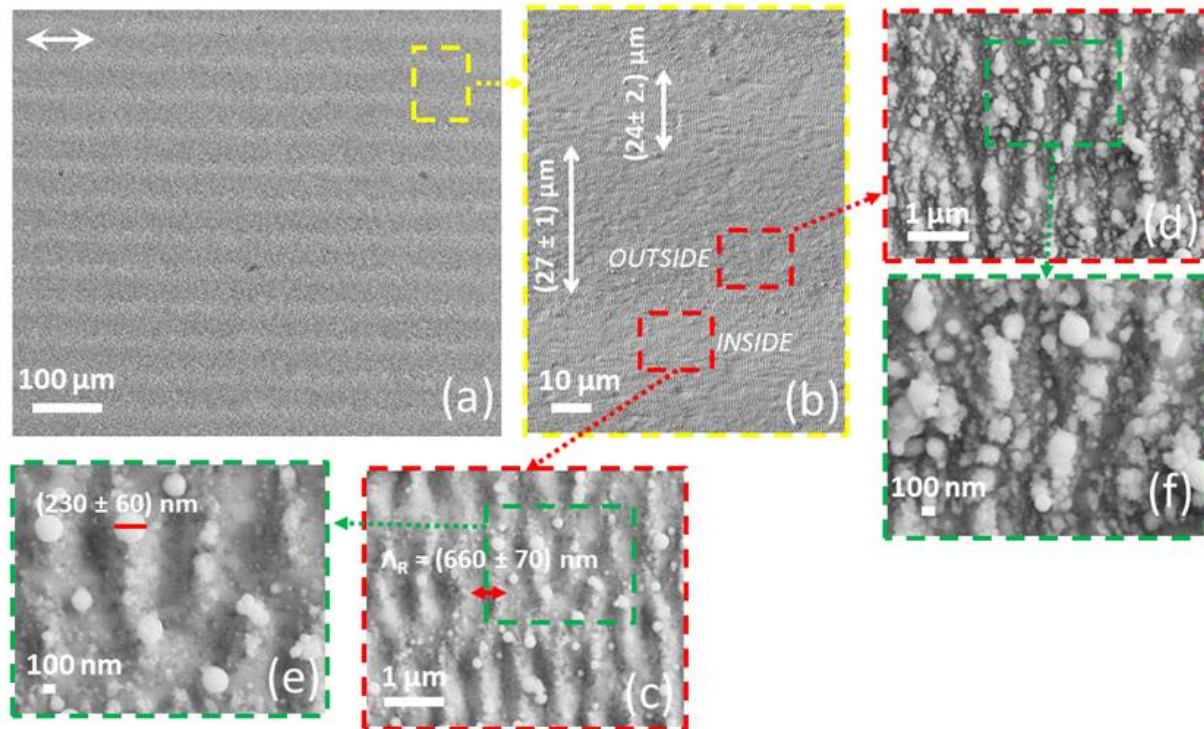
Figure 5.2 SEM images of the surface for the sample elaborated at a laser peak fluence of $F_p = 2.4$ J/cm². Panel (a) reports a SEM image of the sample surface addressing the parallel micro-trenches pattern. The double-headed arrow in panel (a) indicates the laser beam polarization. Panel (b) is a zoomed view registered at higher magnification. Panels (c) and (d) show SEM images of the surface structure inside and outside a micro-trench written by the laser patterning process, respectively. Panels (e) and (f) are zoomed views of the SEM images of panels (c) and (d), respectively.

The degree of wetting was evaluated by standard method of static contact angle (CA) of a water drop. Figure 5.3 (a) shows two examples of photographs of water droplets on surfaces patterned at the minimum and maximum values of peak fluence used. CA measurements are carried out for both the parallel and orthogonal views of the droplets, as sketched in Figure 5.3 (b). The corresponding CA values as a function of F_p are reported in Figure 5.3 (c). The dotted horizontal line in Figure 5.3 (c) represents the CA measured on the copper sample surface without laser texturing, which is ($\approx 100°$), in fairly good agreement with a previous measurement of CA on bare copper of 101.7° [13]. One can observe a step increase of the CA, with respect to the un-treated copper surface, already for the smaller value of $F_p = 0.8$ J/cm².

As the fluence increases, the surface progressively changes to the more complex hierarchical topography illustrated above. Consequently, a rise of the CA with the fluence is generally

observed, both in the orthogonal and parallel imaging configurations (see Figure 5.3 (c)), eventually reaching values of the order of 160° at $F_p \approx 8$ J/cm^2 [5]. This suggests a clear effect of the progressive changes induced by surface texturing on the wetting response of the copper samples. The increase of surface hydrophobicity is likely due to concurrent contributions to the surface morphology occurring over different length scales, like micro-trenches deepening, ripples formation and nanoparticles decoration.
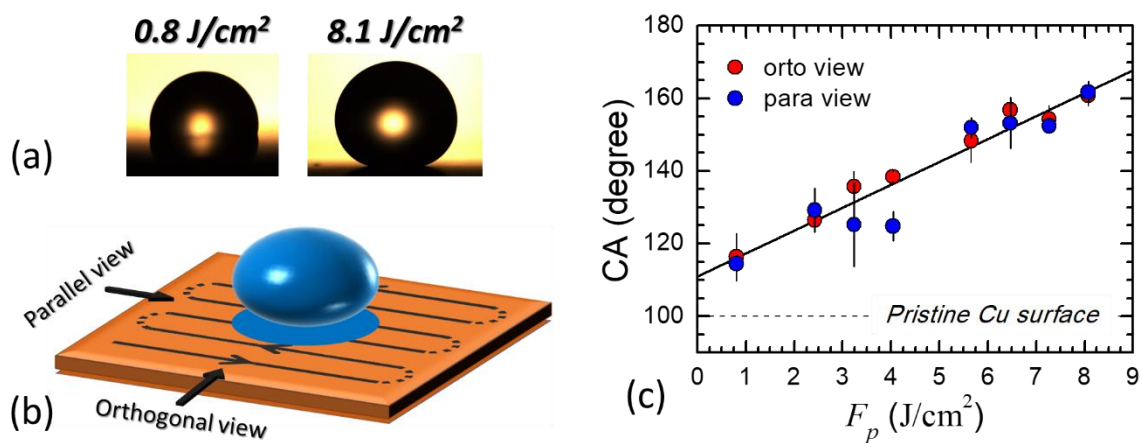

Figure 5.3 (a) Photographs of water droplets on the copper surfaces for samples fabricated at two different values of the peak fluence F_p: 0.8 J/cm^2 – CA≈115° ; 8.1 J/cm^2 – CA≈160°. (b) Sketch of the orthogonal and parallel views used in the water droplet image analysis. (c) Variation of the CA with the laser peak fluence F_p for orthogonal (orto) and parallel (para) views. The dotted horizontal line represents the CA measured on the pristine Copper samples surface. The solid line shows a best fit to a linear dependence.

Our experimental findings show that the formation of micro-trenches decorated with finer morphological features intrinsic to the fs laser surface texturing can be usefully exploited for the modification of the wetting properties of copper samples. More investigations are anyway necessary to further clarify the role of the different length-scales, going from nanoparticle to sub-wavelength ripples to regular patterns of micro-trenches with pitches of several tens of μm, on the different factors affecting the wetting response of a hierarchically structured metallic surface.

5.3   Gold thin-film and THz metasurfaces

In this section, we present a preliminary investigation aiming at producing metasurfaces active in the THz electromagnetic (EM) spectral range by means of fs laser surface patterning. Metasurfaces are a class of metamaterials, i.e. artificial materials with features that do not exist in nature displaying different optical response compared to the transmission theoretical models [14,15]. This is due to the fact that a metamaterial gains its EM properties from its structure rather than inheriting them directly from the materials it is composed of [16,17]. In the visible spectral range, metamaterials are composed of metal-dielectric elements, with micro or nano-scale size, that during the passage of EM waves with relatively larger wavelength act as an array of artificial atoms showing unusual EM properties [15,18]. The geometry of metamaterials can be either volumetric (3D) or two-dimensional (2D), the latter being called metasurfaces (or flat optics). Metasurfaces (MS) consists of a structured dielectric, semiconducting or conducting layer deposited on a low loss insulating substrate. The MS are made by individual elements named unit cells. In the limit of large wavelengths, a MS behaves as a homogeneous material with engineered electrodynamic properties. Thus, a MS can be designed to manipulate the impinging light to realize, for instance, elements showing selective absorption, beam steering, super focusing properties, polarization converters, or to control the overall dielectric function of a sample [19–24].

As for the fabrication techniques of MS for visible light, generally UV [25], soft lithography [26], etc. are employed. However, fs laser ablation can be used as a mask-free manufacturing technique of one and two dimensional MS [27–30] for long wavelength EM radiation, e.g. THz, thanks to the possibility of selective patterning of the original target.

Here we investigated the production of THz MS by means of fs laser surface patterning using as target a thin metallic film over a dielectric substrate. Two approaches were considered fabricating an array of subwavelength holes (static irradiation mode) of substrate dielectric and generating metallic islands through removal of channels of the metal (dynamic irradiation mode) [31]. The fabrication process was carried out by using a Ti: Sapphire system delivering pulses with a duration of ≈35 fs at 800 nm wavelength. The beam was used with a Gaussian spatial intensity distribution to test the feasibility of the approach.

The sample used was a thin gold film over a 400 µm thick silicon (100, intrinsic) substrate. The thickness of the gold film was around 180 nm. Between the Au film and the Si substrate an intermediate sacrificial layer of CrNi with thickness 20 nm was present in order to improve adhesion of gold over the silicon substrate (see Fig. 5.4 (a)).
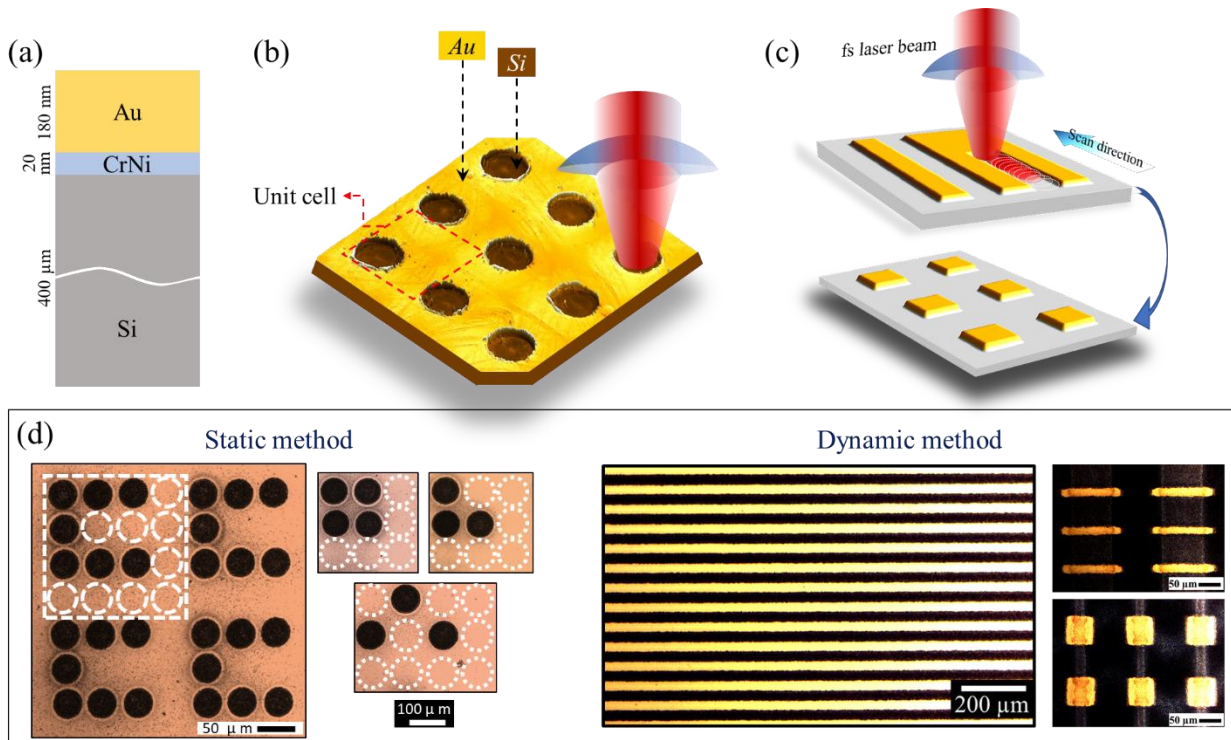

Figure 5.4 Panel (a) displays a schematic cross section of the Au-Si composite sample used as target for the fabrication of the structures. The 3-dimensional schematic view of the procedure used to fabricate the metasurfaces are shown in: panel (b) step scan laser method and (c) upper panel is continuous laser scanning fabrication mode. Lower panel (c) displays a schematic 3-dimensional view of a regular array of the gold. Panel (d) shows images of optical microscopy of the patterned surfaces in static and dynamic irradiation. The red dashed square in panel (b) identifies a basic unit cell.

The sample was mounted on a high precision three-axis stage, electronically controlled by a custom software, and was irradiated at normal incidence. In the static irradiation mode (see i.e. Figure 5.4 (b)), the laser repetition rate was set at 100 Hz, whereas in the dynamic irradiation mode (see i.e. Figure 5.4 (c)) the repetition rate was 500 Hz. In the static mode, circular polarization was used in order to avoid any deformation in the circularity of the hole formed in the metallic film. Instead, linear polarized laser pulses are employed for the dynamic mode. In panel (d) of Figure

5.4, some different examples of the gold thin film surfaces with laser induced patterns suitable for MS applications taken by optical microscopy are shown.

Figure 5.5 (a) reports a SEM image of the sample with a basic unit cell of the MS showed in a red dashed box. Only two fs pulses ($N = 2$) at an energy of 70 µJ were used to remove the metallic film.
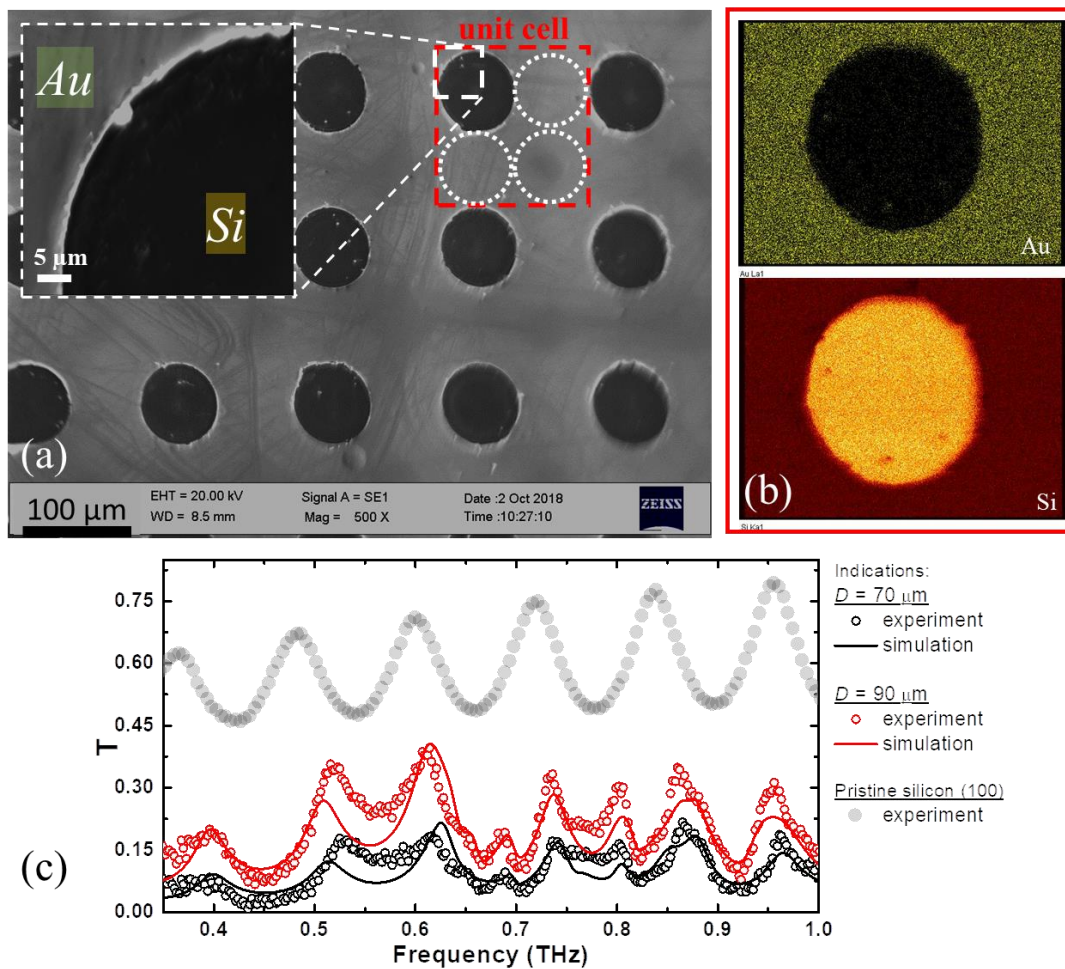

Figure 5.5 Panel (a) SEM image of the metasurfaces with a circular pixel diameter of 70 µm and a unit cell (red dashed box) size of 140 µm × 140 µm. The inset shows a zoomed image of the unit cell. Panel (b) shows EDX images of the sample surface confirming a complete removal of the metallic film in the circular pixel region. Panel (c) reports the transmission response (data points) of the fabricated metasurfaces in the range of (0.2 – 1.0) THz for two different pixel diameters $D = 70$ µm (black) and $D = 90$ µm (red), while keeping the unit cell size fixed at 140 µm. The solid lines show the simulation of the corresponding features. The gray data points represent the measured transmission spectra of the pristine silicon substrate.

The beam was focused on the sample by a lens of focal length f = 70 mm generating a circular hole with a diameter $D = 70$ μm. A zoomed view of the ablated hole is given in the inset of Figure 5.5 (a) showing a good quality of the circular hole edge. Moreover, a complete and clear perforation of the metallic film is confirmed by the good contrast of the energy dispersive X-ray (EDX) images reported in Figure 5.5 (b).

The THz response was analyzed though THz Time Domain Spectroscopy (TDS) exploiting a standard setup (Tera-K15, Menlo Systems) by the group working on Material spectroscopy and devices at high frequencies led by Prof. Andreone at the Department of Physics of University of Napoles "Federico II" within a collaborative work. The TDS system is based on photo-conducting antennas (PCA) made of low temperature gallium arsenide (LT-GaAs), generating a transient electric field pulse of 1-2 ps when excited by a 90-fs pulsed laser at 1560 nm. Signals were acquired over a time scale of about 220 ps guaranteeing a frequency resolution of about 2.5 GHz. Experiments were performed in dry nitrogen environment to reduce unwanted water vapor peaks in the frequency spectrum. The linearly polarized beam was collimated using TPX lenses before impinging on the MS, so that one can safely assume an incident plane wave approximation.

Various MSs were fabricated by static or dynamic mode and their THz response was analyzed in the frame of a collaborative project thorough illustration of the THz measurements carried out and the achieved results can be found in reference [31]. Here we only illustrate the THz response of two MSs, fabricated by replicating a square unit cell like that of Figure 5. 5 (a) over a square sample of 8×8 mm^2. The unit cell size is 140 μm both in the vertical and horizontal directions, and the diameter of the circles is $D = 70$ μm and $D = 90$ μm. The THz transmission coefficient of the two MS in the region of 0.2–1.3 THz is reported in Figure 5. 5 (c). In Figure 5. 5 (c), the data points are the experimentally measured signals while the solid lines are the simulation results obtained by modelling the corresponding unit cell. The full-wave simulations were carried out using a commercial software for EM simulations (CST Microwave Studio) by Gian Paolo Papari. Further, the response of the bare silicon substrate is reported as well (in gray color) for comparison. The Si substrate transmission signal shows an oscillating behavior due to the etalon effect induced on the THz radiation from the 400 μm thick silicon plate. Such an effect should be taken into account while assessing the frequency response of the resonant surfaces. The experimental results for the two different hole diameters (red and black circles in Figure 5.5 (c)) show the presence of

specific transmission resonances in the frequency spectrum with many peaks and troughs associated with the surface resonator geometry and size. In fact, the general spectral features for the two metasurfaces are very similar with a slight shift of the peak positions by changing the pixel diameter and an increase of transmission for the one with the larger value of D. The frequency variation of the transmission is fairly well described by the simulated profiles. The experimental findings address the feasibility of the approach and the possibility to design specific geometries to tailor the THz response of the sample.

5.4 Structuring of CdZnTe

CdZnTe is a direct and wide band gap ternary semiconductor alloy, formed by substituting Cd by Zn. The band gap of CdZnTe comes in the range of 1.45-2.26 eV depending on the Zn concentration. High atomic number, high density, wide bandgap, low chemical reactivity, and long-term stability makes CdZnTe an ideal material for various important applications that include solar cells, electro-optical modulator, photoconductors, light emitting diode, X-ray and gamma ray detectors [32,33]. Laser surface processing on this material was reported by [34–38], however, mostly nanosecond (ns) pulsed lasers were used. Here, we report preliminary outcomes on fs laser induced surface processing of CdZnTe that, to the best of our knowledge, has not been investigated yet. Irradiation with fs pulses results in modification of CdZnTe surface with decoration by periodic structures, formation of cracks and columnar features [39].

The fs laser pulses were provided by a Ti:Sapphire laser (Legend, Coherent Inc.) delivering linearly polarized ≈ 35 fs pulses at a central wavelength around 800 nm. The target was a (211) $Cd_{1-x}Zn_xTe$ sample, with $x = 0.04$ prepared by Bridgeman-Stockbarge method (in collaboration with Prof. Q. Hao of North China Research Institute of Electro-optics and Prof. X. Wang of Wuhan University). In the experiments, the target is irradiated at normal incidence by the fundamental Gaussian beam with a beam waist $w_0 = 22$ μm, in ambient air. A progressive reduction of the threshold fluence F_{th} with N was observed, indicating an incubation effect for which the threshold fluence varies with pulse number as shown in Chapter 2, Equation (16). The incubation factor was estimated to be $\xi = 0.80 \pm 0.05$, which similar with that observed for silicon [40], with single shot fluence threshold $F_{th}(1) = (0.014 \pm 0.001)$ J/cm^2.

To analyze the induced surface structures, we considered two categories of experimental conditions; low energy – low number of pulses (N) and high energy – high number of pulses. In the former case, the peak fluence is 0.64 J/cm^2, much higher than single shot ablation threshold, hence in an ablation regime. SEM images of the sample surface at different values of N are shown in Figure 5.6. Panel (a) shows that after $N = 20$ pulses the surface is covered with well-defined cracks oriented in various directions. From the zoomed views in the lower panel, one can recognize that cracks are in form of straight lines with lengths of several μm. Moreover, the high-resolution image in the inset, indicates that these cracks are characterized by a width in the range of few tens of nm, namely ≈20 nm. The presence of similar cracks was clear at low number of laser pulses (e.g., $5 \leq N \leq 50$) for all investigated laser peak fluences ($0.64 \leq F_p \leq 7.0$ J/cm^2). Panel (b) shows the surface after an irradiation sequence with $N = 30$ and addresses the formation of nano-holes arrays with a period of (698 ± 60) nm along the crack's direction. Panel (c) displays the morphology of the crater for $N = 50$ laser pulses. Here the crater shows a more complex pattern, lend rhombus shaped micro bumps form on the target surface, as shown in the zoomed view. Apart from this, randomly distributed surface defects in the form of nano-holes can be found all over the crater area. Panel (d) illustrates the sample surface after irradiation with $N = 100$ laser pulses. At this pulse number a deeper crater is formed, and well-developed micro-columnar surface features appear over the central region corresponding to the most intense part of the beam. Finally, it is worth noticing that, the SEM images show only a very minimal trace of nanoparticles around the ablation spot in this experimental condition.

Before passing to the analysis of the effects of higher pulse energy and larger number of shots, we make an attempt to discuss about the possible mechanisms leading to the formation of cracks. The particular alignment of the cracks suggests a connection of their formation mechanism with the structural properties of the sample material. The cracks likely form after melting and re-solidification of the irradiated material surface and their generation could result from different thermal coefficients of the sample components or structural defects already present in the original material. Structural imperfections in CdZnTe have been extensively investigated and dispersed Te inclusions are reported as one of the main bulk defects [41,42]. The detailed explanation of these preliminary results can be found in [39].
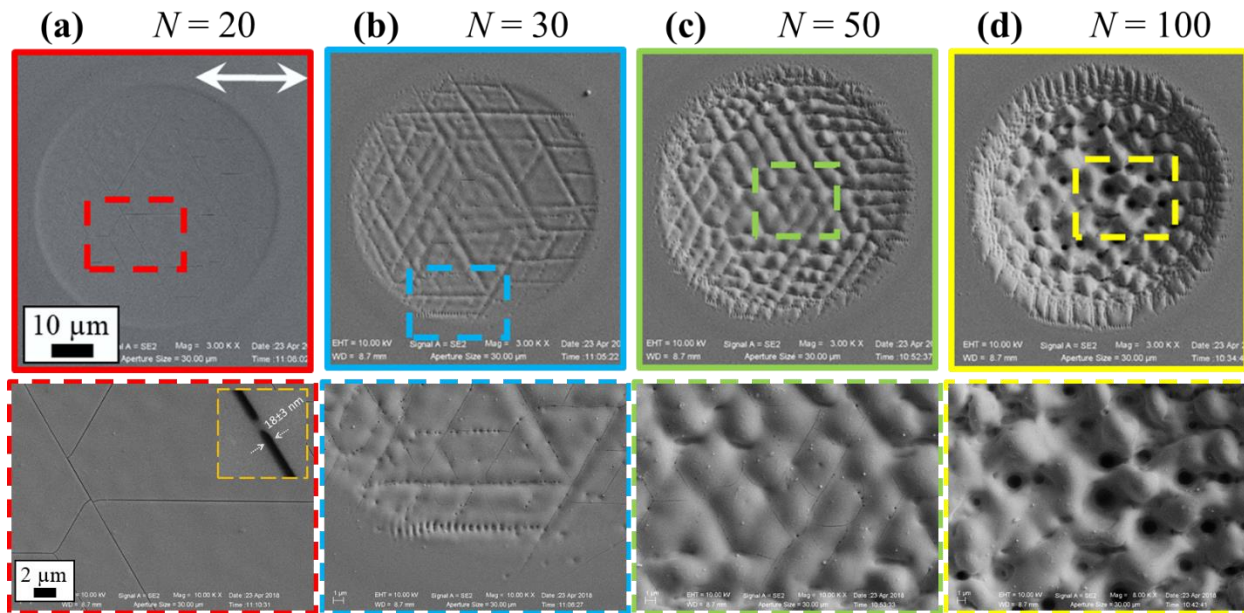
Figure 5.6 SEM images of CdZnTe after irradiation with a sequence of various number of pulses N, at $F_p = 0.64$ J/cm^2 and corresponding zoomed views in lower panels. Panel (a) displays the surface after the irradiation with $N = 20$. The white arrow represents the laser polarization direction. (b) $N = 30$, (c) $N = 50$, (d) $N = 100$.

Figure 5.7 shows two examples of structured surfaces under the condition of high pulse fluence (peak fluence $F_p \approx 7.0$ J/cm^2) and large number of pulses ($N = 500$ and $N = 1000$). These conditions typically lead to the formation of a deep crater surrounded by a significant debris of nanoparticles resulting from the backward deposition of the ablated material around the crater due to the confining effect of the atmospheric air pressure, as we discussed in Section 4.4. Interestingly, in such a situation one can also observe the generation of well-ordered ripples in the region outside the main crater, where the local fluence is very much lower to that of peak fluence of the irradiating laser beam, as displayed for example in Figure 5.7.

As shown in the insets of panels (a, b) of Figure 5.7, the periodic LIPSS perpendicular to the laser polarization are formed over an annular area surrounding the deep crater (indicated by arrows pointing outside). For instance, at $N = 1000$ the ripples are found over a ring characterized by an average radial distance of ≈ 60 μm from the center of the crater spot and with a thickness of the annular disk of ≈ 20 μm. The spatial period of the surface ripples shown in panel (a), $N=500$, suggests the presence of both LSFL and HSFL over the same area which can be due to the fact that both type of ripples might be generated starting from nanoparticles arrays [39].
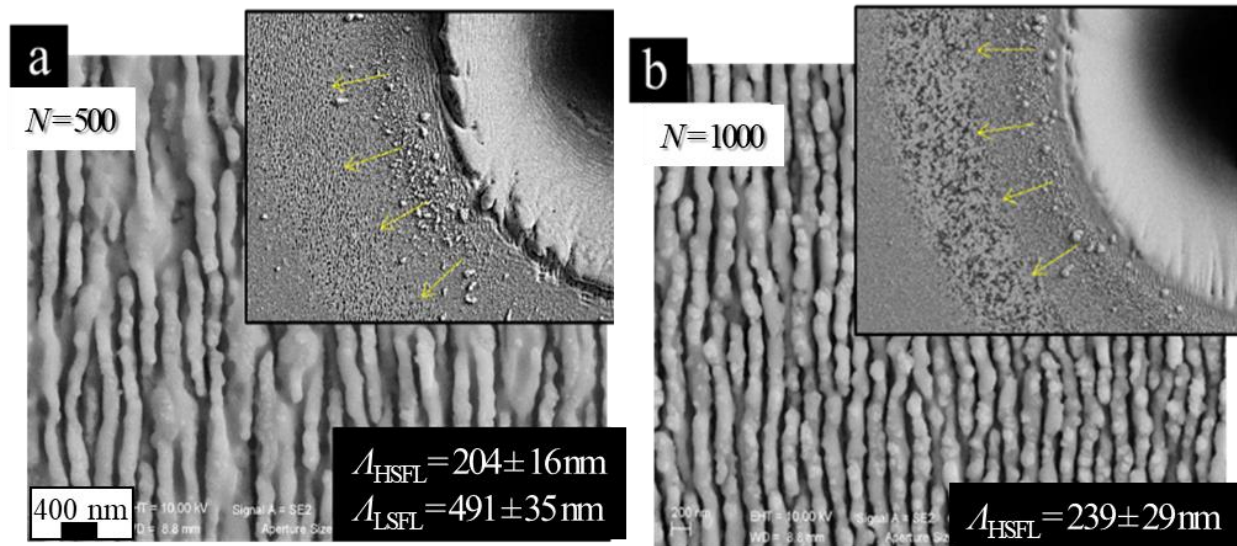
Figure 5.7 Low frequency and high frequency periodic surface structures formed on CdZnTe sample a peak fluence $F_p \approx 7.0$ J/cm^2 for high pulse number N, namely (a) $N = 500$ and (b) $N = 1000$.

Our experimental finding evidences a variety of effects related to laser irradiation of CdZnTe with energetic fs pulses that can be of interest in laser processing, ablation and structuring of these materials. However, further investigations and surface characterizations are needed to fully understand the formation mechanism and physical processes involved in laser surface structuring of this material.

References

[1]   D. Huerta-Murillo, A. García-Girón, J.M. Romano, J.T. Cardoso, F. Cordovilla, M. Walker, S.S. Dimov, J.L. Ocaña, Wettability modification of laser-fabricated hierarchical surface structures in Ti-6Al-4V titanium alloy, Appl Surf Sci. 463 (2019) 838–846. https://doi.org/10.1016/j.apsusc.2018.09.012.

[2]   J. Long, P. Fan, M. Zhong, H. Zhang, Y. Xie, C. Lin, Superhydrophobic and colorful copper surfaces fabricated by picosecond laser induced periodic nanostructures, Appl Surf Sci. 311 (2014) 461–467. https://doi.org/10.1016/j.apsusc.2014.05.090.

[3]   A.Y. Vorobyev, C. Guo, Multifunctional surfaces produced by femtosecond laser pulses, J Appl Phys. 117 (2015) 033103. https://doi.org/10.1063/1.4905616.

[4]   A.-M. Kietzig, S.G. Hatzikiriakos, P. Englezos, Ice friction: The effects of surface roughness, structure, and hydrophobicity, J Appl Phys. 106 (2009) 024303. https://doi.org/10.1063/1.3173346.

[5]   E. Allahyari, J. JJ Nivas, S.L. Oscurato, M. Salvatore, G. Ausanio, A. Vecchione, R. Fittipaldi, P. Maddalena, R. Bruzzese, S. Amoruso, Laser surface texturing of copper and variation of the wetting response with the laser pulse fluence, Appl Surf Sci. 470 (2019) 817–824. https://doi.org/10.1016/j.apsusc.2018.11.202.

[6]   R. Buividas, M. Mikutis, S. Juodkazis, Surface and bulk structuring of materials by ripples with long and short laser pulses: Recent advances, Prog Quantum Electron. 38 (2014) 119–156. https://doi.org/10.1016/j.pquantelec.2014.03.002.

[7]   M. Gedvilas, J. Mikšys, G. Račiukaitis, Flexible periodical micro- and nano-structuring of a stainless steel surface using dual-wavelength double-pulse picosecond laser irradiation, RSC Adv. 5 (2015) 75075–75080. https://doi.org/10.1039/C5RA14210E.

[8]   M.S. Sidhu, P. Munjal, K.P. Singh, High-fidelity large area nano-patterning of silicon with femtosecond light sheet, Appl Phys A. 124 (2018) 46. https://doi.org/10.1007/s00339-017-1459-3.

[9]   C.A. Zuhlke, G.D. Tsibidis, T. Anderson, E. Stratakis, G. Gogos, D.R. Alexander, Investigation of femtosecond laser induced ripple formation on copper for varying incident angle, AIP Adv. 8 (2018) 015212. https://doi.org/10.1063/1.5020029.

[10]   M. Hashida, A.. Semerok, O. Gobert, G. Petite, Y. Izawa, J..- Wagner, Ablation threshold dependence on pulse duration for copper, Appl Surf Sci. 197–198 (2002) 862–867. https://doi.org/10.1016/S0169-4332(02)00463-4.

[11]   S. Tani, Y. Kobayashi, Pulse-by-pulse depth profile measurement of femtosecond laser ablation on copper, Appl Phys A. 124 (2018) 265. https://doi.org/10.1007/s00339-018-1694-2.

[12]   S. Nolte, C. Momma, H. Jacobs, A. Tünnermann, B.N. Chichkov, B. Wellegehausen, H. Welling, Ablation of metals by ultrashort laser pulses, J Opt Soc Am B. 14 (1997) 2716. https://doi.org/10.1364/JOSAB.14.002716.

[13]   X. Wang, L. Wang, Dynamic Contact Angle on a Surface with Gradient in Wettability, in: Int Refrig AIR Cond Conf, 2016: p. 1806.

[14]   A. Sytchkova, Complex materials with subwavelength inclusions for optical thin film applications, in: Opt Thin Film Coatings, Elsevier, 2018: pp. 143–186. https://doi.org/10.1016/B978-0-08-102073-9.00005-9.

[15]   A. Selimis, M. Farsari, 3.8 Laser-Based 3D Printing and Surface Texturing, in: Compr Mater Finish, Elsevier, 2017: pp. 111–136. https://doi.org/10.1016/B978-0-12-803581-8.09171-2.

[16] M. Mehdizadeh, The Impact of Fields on Materials at RF/Microwave Frequencies, in: Microwave/RF Appl Probes Mater Heating, Sensing, Plasma Gener, Elsevier, 2010: pp. 1–34. https://doi.org/10.1016/B978-0-8155-1592-0.00001-6.

[17] K. Parveen, Metamaterials: Types, applications, development, and future scope, 2018.

[18] A. Argyros, A. Tuniz, S.C. Fleming, B.T. Kuhlmey, Drawn metamaterials, in: Optofluidics, Sensors Actuators Microstruct Opt Fibers, Elsevier, 2015: pp. 29–54. https://doi.org/10.1016/B978-1-78242-329-4.00002-3.

[19] J.B. Pendry, Negative Refraction Makes a Perfect Lens, Phys Rev Lett. 85 (2000) 3966–3969. https://doi.org/10.1103/PhysRevLett.85.3966.

[20] S.-C. Jiang, X. Xiong, Y.-S. Hu, Y.-H. Hu, G.-B. Ma, R.-W. Peng, C. Sun, M. Wang, Controlling the Polarization State of Light with a Dispersion-Free Metastructure, Phys Rev X. 4 (2014) 021026. https://doi.org/10.1103/PhysRevX.4.021026.

[21] A. Alù, M.G. Silveirinha, A. Salandrino, N. Engheta, Epsilon-near-zero metamaterials and electromagnetic sources: Tailoring the radiation phase pattern, Phys Rev B. 75 (2007) 155410. https://doi.org/10.1103/PhysRevB.75.155410.

[22] G.P. Papari, C. Koral, A. Andreone, Geometrical Dependence on the Onset of Surface Plasmon Polaritons in THz Grid Metasurfaces, Sci Rep. 9 (2019) 924. https://doi.org/10.1038/s41598-018-36648-x.

[23] R. Singh, W. Cao, I. Al-Naib, L. Cong, W. Withayachumnankul, W. Zhang, Ultrasensitive terahertz sensing with high- Q Fano resonances in metasurfaces, Appl Phys Lett. 105 (2014) 171101. https://doi.org/10.1063/1.4895595.

[24] M.R.M. Hashemi, S.-H. Yang, T. Wang, N. Sepúlveda, M. Jarrahi, Electronically-Controlled Beam-Steering through Vanadium Dioxide Metasurfaces, Sci Rep. 6 (2016) 35439. https://doi.org/10.1038/srep35439.

[25] J.E. Heyes, W. Withayachumnankul, N.K. Grady, D.R. Chowdhury, A.K. Azad, H.-T. Chen, Hybrid metasurface for ultra-broadband terahertz modulation, Appl Phys Lett. 105 (2014) 181108. https://doi.org/10.1063/1.4901050.

[26] S. Walia, C.M. Shah, P. Gutruf, H. Nili, D.R. Chowdhury, W. Withayachumnankul, M. Bhaskaran, S. Sriram, Flexible metasurfaces and metamaterials: A review of materials and fabrication processes at micro- and nano-scales, Appl Phys Rev. 2 (2015) 011303. https://doi.org/10.1063/1.4913751.

[27] M.L. Tseng, P.C. Wu, S. Sun, C.M. Chang, W.T. Chen, C.H. Chu, P.L. Chen, L. Zhou, D.W. Huang, T.J. Yen, D.P. Tsai, Fabrication of multilayer metamaterials by femtosecond laser-induced forward-transfer technique, Laser Photon Rev. 6 (2012) 702–707. https://doi.org/10.1002/lpor.201200029.

[28] B. Voisiat, A. Bičiūnas, I. Kašalynas, G. Račiukaitis, Band-pass filters for THz spectral

range fabricated by laser ablation, Appl Phys A. 104 (2011) 953–958. https://doi.org/10.1007/s00339-011-6456-3.

[29]   M. Zamfirescu, Femtosecond Laser Fabrication of Metamaterials for High Frequency Microwave Devices, J Laser Micro/Nanoengineering. 3 (2008) 5–8. https://doi.org/10.2961/jlmn.2008.01.0002.

[30]   R. Gente, I. Al-Naib, M. Koch, N. Born, Laser beam machined free-standing terahertz metamaterials, Electron Lett. 51 (2015) 1012–1014. https://doi.org/10.1049/el.2015.0655.

[31]   G.P. Papari, J.J.J. Nivas, C. Koral, E. Allahyari, S. Amoruso, A. Andreone, Engineering of High Quality Factor THz Metasurfaces by Femtosecond Laser Ablation, Opt Laser Technol. Revision s (2020).

[32]   S. Komarov, Y. Yin, H. Wu, J. Wen, H. Krawczynski, L.-J. Meng, Y.-C. Tai, Investigation of the limitations of the highly pixilated CdZnTe detector for PET applications, Phys Med Biol. 57 (2012) 7355–7380. https://doi.org/10.1088/0031-9155/57/22/7355.

[33]   C. Szeles, CdZnTe and CdTe materials for X-ray and gamma ray radiation detector applications, Phys Status Solidi. 241 (2004) 783–790. https://doi.org/10.1002/pssb.200304296.

[34]   A. Medvid', N. Litovchenko, A. Mychko, Y. Naseka, Exciton quantum confinement in nanocones formed on a surface of CdZnTe solid solution by laser radiation, Nanoscale Res Lett. 7 (2012) 514. https://doi.org/10.1186/1556-276X-7-514.

[35]   V.A. Gnatyuk, O.I. Vlasenko, S.N. Levytskyi, T. Aoki, Laser-Induced Modification of Properties of CdZnTe Crystals, Adv Mater Res. 1117 (2015) 15–18. https://doi.org/10.4028/www.scientific.net/AMR.1117.15.

[36]   A. Medvid', A. Mychko, E. Dauksta, V. Kosyak, L. Grase, Laser ablation in CdZnTe crystal due to thermal self-focusing: Secondary phase hydrodynamic expansion, Appl Surf Sci. 374 (2016) 77–80. https://doi.org/10.1016/j.apsusc.2015.09.225.

[37]   A. Medvid, A. Mychko, O. Strilchyk, N. Litovchenko, Y. Naseka, P. Onufrijevs, A. Pludonis, Exciton quantum confinement effect in nanostructures formed by laser radiation on the surface of CdZnTe ternary compound, Phys Status Solidi. 6 (2009) 209–212. https://doi.org/10.1002/pssc.200879869.

[38]   A. Mychko, A. Medvid', J. Barloti, Y. Naseka, Influence of Laser Radiation on Optical Properties and Surface Structure of CdZnTe Crystal, Adv Mater Res. 222 (2011) 130–133. https://doi.org/10.4028/www.scientific.net/AMR.222.130.

[39]   J.J. Nivas, E. Allahyari, A. Vecchione, Q. Hao, S. Amoruso, X. Wang, Laser ablation and structuring of CdZnTe with femtosecond laser pulses, J Mater Sci Technol. Revision s (2020).

[40]   J. Bonse, S. Baudach, J. Krüger, W. Kautek, M. Lenzner, Femtosecond laser ablation of

silicon–modification thresholds and morphology, Appl Phys A. 74 (2002) 19–25. https://doi.org/10.1007/s003390100893.

[41]   P. Rudolph, Non-stoichiometry related defects at the melt growth of semiconductor compound crystals – a review, Cryst Res Technol. 38 (2003) 542–554. https://doi.org/10.1002/crat.200310069.

[42]   A.E. Bolotnikov, G.S. Camarda, G.A. Carini, Y. Cui, L. Li, R.B. James, Cumulative effects of Te precipitates in CdZnTe radiation detectors, Nucl Instruments Methods Phys Res Sect A Accel Spectrometers, Detect Assoc Equip. 571 (2007) 687–698. https://doi.org/10.1016/j.nima.2006.11.023.

Conclusions

This thesis reports detailed investigations on direct fs laser surface structuring. Within the framework of the thesis, various surface structures have been considered going from single craters covered with self-organized laser induced (quasi-)periodic surface structures (LIPSSs), surface patterns realized by laser scanning and elaboration of atypical arrays of holes or islands. Moreover, the influence of some experimental parameters, like laser pulse repetition rate and wavelength or ambient pressure, have been also addressed with particular emphasis on supra-wavelength LIPSS, named as grooves.

The experiments were designed basically with the following aims: i) gather further indications on the physical processes involved in the formation of the surface structures; ii) search for possibilities to control the morphological characteristics of the laser-generated structures; iii) take a preliminary glance towards scientific applications or materials of possible technological and industrial interest. The thesis consists of five chapters in addition to the current one that presents the overall summary of the work.

The first chapter gave a concise, general introduction to the field of laser surface structuring. Direct laser micromachining methods are interesting for a number of advantages like the characteristics of being contactless and very flexible, applicable to almost any material and for the capability to deposit very precisely the laser energy on the material, to quote a few. After illustrating the pioneering original works leading to laser induced surface structures soon after the invention of the laser with long pulses, the advent of ultrashort laser sources was highlighted. Introduction of ultrashort pulse lasers compared to the conventional nanosecond ones brought many advantages that in Chapter 1 were explained in detail. The classifications and specification of the LIPSSs were given as well. There are some models which predict the formation of LIPSS, in particular, low spatial frequency LIPSS (ripples), i.e. capillary wave excitation, solid surface defects, excitation of surface plasmon polaritons with fs laser pulses, etc. As for the supra-wavelength structures, especially grooves, there are few proposed theories and mainly based on hybrid models. Therefore, lack of information on the clear formation mechanisms of the grooves motivated part of the experiments carried out in the frame of this work and along with this idea also other approaches were discussed.

The second chapter illustrated the experimental setups (laser sources, optical component and target materials). An introduction to Gaussian and optical vector vortex beams was also considered together with methods of threshold fluence estimation and spot size measurement for both cases. Finally, the characterization techniques for the analysis of the fabricated surfaces were provided.

In Chapter 3 the fabrication of LIPSSs using optical vector vortex beams was addressed. The vector vortex beams were generated by means of an optical device, the q-plate, and focused onto a silicon target surface, in air. The observation of the orientation of the LIPSS following the complex state of polarization of vector vortex beams generated by q-plates with different order of q was illustrated in detail as a simple method to produce complex and unconventional LIPSS patterns. Regulation of the input parameters of the q-plate, like the external applied voltage, affects the optical retardation and the properties of the generated light beams. In this chapter, it is explained how this can be used as an additional strategy getting a maskless approach to the fabrication of unique surface structures with unconventional surface patterns in a facile way.

The fourth chapter was dedicated to the investigation of role of experimental parameters (laser pulse repetition rate, wavelength and ambient pressure) on crater shape and fine morphologies.

i. The experimental analysis of silicon laser surface structuring for laser pulse repetition rates in the range 10 Hz-200 kHz showed clear reduction of the crater volume and size at high repetition rate ($f_p > 20$ kHz), which was associated to a possible shielding by the ablation plume confined in front of the target surface. Then we observed the presence of a network of asymmetric globular micro-structures replacing the typical supra-wavelength grooves in the central region of the crater, besides sub-wavelength ripples decorating the outer region. Further, our findings suggest that the ablated material formed above the target surface can influence the feedback mechanisms involved in the development of the final surface texture during multi-pulse fs laser surface processing of solid samples, in air, at high repetition rates.

ii. Two different laser wavelengths, 513 nm and 1026 nm were employed to investigate the formation of supra-wavelength grooves on silicon, in air, in static and dynamic irradiation conditions. There is an increasing trend of grooves' period with number of pulses and the values are dependent on wavelength. A comparison between the structures formed in static and dynamic conditions evidenced that they are rather similar. However, comparing results

achieved at similar laser peak fluence for the two wavelengths, we observed that different structures are achieved possibly as a result of the different state of excitation induced in silicon by the absorbed photons at the two different laser wavelengths. Additionally, some simulations of grooves formation carried out in conditions similar to the experimental ones addressed an important role of hydrothermal waves in their formation.

iii. Fabrication of surface structures on silicon target was experimentally analyzed at different surrounding ambient pressure. We have shown the effect of ambient pressure on the LIPSSs features. 1) The spatial period of the ripples reduced as a function of the pressure. 2) The absence of grooves under high vacuum conditions was observed. 3) The shape of the crater deformed from elliptical to circular by increasing the pressure from vacuum to atmospheric one. The obtained results from these experiments suggested the possible involvement of ablated nanoparticles in the grooves formation mechanisms.

Finally, Chapter 5 was devoted to illustrating some cases of laser surface texturing on metal, metallic thin film and wide band-gap semiconductor pursued during the thesis work. The objective of this chapter not only was to perform different types of structuring on different materials but also to introduce the possibilities of this technique in practical applications. In the first case, large area laser surface texturing on copper was realized creating microtrenches by continuous laser scanning, in air. The laser processing, generated ripples decorated with nanoparticles inside and outside of the formed channels. How the changes in roughness affected the degree of water wetting was investigated. The second example dealt with laser processing of a gold thin film over a silicon substrate. Arrays of holes or arrays of islands were imprinted on the sample creating simple metasurfaces and testing their THz transmission response. The interesting preliminary results indicates good perspectives for the development of more complex THz metasurfaces by exploiting laser surface processing with structured light beams like vector vortex. In fact, the step scan and vector vortex can allow patterning over large area structures with peculiar shapes that could be of interest for applications like THz optical components as the preliminary results on simpler structures seem to indicate. Also, the very peculiar ripples and grooves patterns produced with complex light beams as well as the new LIPSS observed in high vacuum might offer new surfaces with functional properties not yet investigated. Finally, fs laser surface structuring of a wide bandgap material, such as CdZnTe, was characterized under different static irradiation conditions. Depending on the laser beam parameters, different types of structures including cracks, high spatial

frequency LIPSS (HSFL) and low spatial frequency LIPSS (LSFS) were observed. The preliminary experiments showed a very interesting behavior for such scarcely investigated material that will deserve further investigations.

Acknowledgements

Since I remember I had the desire of earning the highest level of academic degrees. I am happy that I could reach the milestone of my childhood and I am happier that I am not anymore officially "student"! But I wish to remain as a researcher, having a thirst for knowledge.

During all my education, I have had the assist of several people. I am thankful to all my teachers at schools and universities who kept me motivated. In the same way, it's my pleasure to be grateful for everybody's support in the time of my PhD that without their supports this process was not possible.

I spent three years in a small, but unique family: one of "Laser Ablation – lab 1H28". It was special because we were in a seriousness work atmosphere and in our free time, we were full of humor. Firstly, I would deeply admire my supervisor, Prof. Salvatore Amoruso, for his guiding influence. I was surprised of how he was generous with his time and knowledge. His office always welcomed me. Anytime that I knocked the door, "Professor, sorry, do you have time?"; his answer was: "I always have time for you"! Sometimes, I was even embarrassed of his availability despite of his busy schedule, especially on a tight timeline of thesis revision! I am so much thankful to him, for all his scientific supports and his care when I just arrived in Naples. Secondly, I would like to thank a senior postdoc, a colleague, and a friend, Dr. Jijil JJ Nivas. We have shared the laboratory and we performed all the experiments together. We had very good time, with all agreements and disagreements on doing the experiments. I thank him also for all his lab experiences that he passed them to me. Finally, it's my pleasure to express my thanks to Prof. Riccardo Bruzzese, the "father" of our small family! I will always remember his guiding presence, his attention towards my PhD progress and all our pizza time.

When I arrived in Naples, due to lack of experiences and not being fluent in Italian language, it was impossible to survive in Napoli without constant support of Mr. Guido Celentano. Listing out the occasions that Guido helped me would need several pages! I am extremely thankful to him for everything and for the hours he spent accompanying me in immigration office and other offices.

Before continuing acknowledging the professional assistances, I have to thank to my parents, Bahman and Ferdows, my brother, Aref, my cousin, Sara, who is closer to me than a sister and all

my extended family. My parents, apart from their parental responsibilities, bravely watched me while I was flying with my wishes even if sometimes my wishes were above their emotional threshold. I cannot imagine myself as a parent making the same sacrifice as they did to me, in future. دستانشان را میبوسم و تا ابد برای دیدن لبخندشان تلاش میکنم . I am also grateful to my partner, Danilo, who always encouraged me when I was disappointed and understood me when I was full of tired, particularly, during the past couple of weeks of last step of thesis writing, I have to confess that I was so weird! I am thankful to his family, as well, they never let me feel homesick and alone in Napoli; Li ringrazio, sono gentilissimi.

Motivation and creating idea were not enough to obtain the matured results. Many groups and people had a contribution to make this thesis as it stands. I apologize for not writing their honorific titles. First and foremost, I extend my gratitude to Rosalba (Tatiana) Fittipaldi, Veronica Granata and Antonio Vecchione for their patience in taking SEM images and EDX mapping. Thanks also to the SEM instruments, Diego and Armando… Forza Napoli sempre! Then, I express my appreciation to Giovanni Ausanio who taught me how to use AFM and he helped me in acquiring the images. Furthermore, I would like to thank Xuan Wang for providing the CdZnTe sample and all his scientific supports; Filippo Cardano, Andrea Rubano, Domenico Paparo and Lorenzo Marrucci for the q-plates and theoretical supports of optical vector vortex beam; Mohammadhassan (Ehsan) Valadan and Carlo Altucci, for sharing the laser and their helpful cooperation during the experiments; Marcella Salvatore, Stefano Oscurato and Pasquale Maddalena for the AFM, Micro Raman and wetting measurements; Guerino Avallone and Carla Cirillo for the profilometry analysis; Gian Paolo Papari and Antonello Andreone for their collaboration in THz theoretical and experimental measurements. Eventually, I would like to thank Evangelos Skoulas, George D. Tsibidis and Emmanuel Stratakis for their warm hospitality, sharing ideas and experiences during our unforgettable trip to Heraklion (Greece).

At this point, I would like also to thank the team of Promete; my former supervisors and their valuable roles while I was applying for the PhD position, Dr. Shahrooz Saviz, Dr. Nandakumar Kalarikkal and Prof. Oluwatobi Oluwafemi; my friends, from near and far who always made me strong. In fact, the list of names would be too long and as a way of expressing my thanks to them, I would like to share our memorable moments in a photo towards the end.

From my heart, I truly appreciate whoever, directly and indirectly, helped me on my way.

Elaheh
Napoli – 14/Jan/2020.

Vitae

The author was born in Tehran, Iran on May 26, 1990. She received a Bachelor of Science degree in Engineering Physics – Plasma Physics in 2012 and a Master of Science (MSc) degree in Physics – Atomic and Molecular in 2014, both from Plasma Physics Research Center, Science and Research, I. Azad University, Tehran, Iran. After obtaining the MSc degree she started a voluntary internship visit on the topic of laser ablation in liquid during the years of 2015 and 2016 in Mahatma Gandhi University, Kerala, India. She then came to the University of Naples Federico II, Naples, Italy and began her research doctorate program in Physics in February 2017 and completed in January 2020. She pursued her PhD in "surface micro-structuring with ultrashort laser pulses" under the guidance of Prof. Salvatore Amoruso. Her research was supported by the Ministry of Education, University and Research of Italy.

Published articles related to my thesis

1. E. Allahyari, J. JJ Nivas, E. Skoulas, R. Bruzzese, G. D. Tsibidis, E. Stratakis and S. Amoruso, "On the formation and features of the supra-wavelength grooves generated during femtosecond laser surface structuring of silicon", "submitted to Journal of Applied Surface Science"

2. Gian Paolo Papari, Jijil JJ Nivas, Can Koral, Elaheh Allahyari, Salvatore Amoruso, and Antonello Andreone,"Engineering of High Quality Factor THz Metasurfaces by Femtosecond Laser Ablation", Optics and Laser Technology, (2020) Accepted.

3. J. JJ Nivas, E. Allahyari, A. Vecchione, Q. Hao, S. Amoruso, X. Wang, "Laser ablation and structuring of CdZnTe with femtosecond laser pulses.", Journal of Materials Science & Technology, (2020) Accepted.

4. Jijil JJ Nivas, Elaheh Allahyari, Salvatore Amoruso, "Direct femtosecond laser surface structuring with complex light beams generated by q-plates – invited review article", Advanced Optical Technologies (AOT), 0.0 (2020).

5. E. Allahyari, J. JJ Nivas, G. Avallone, M. Valadan, M. Singh, V. Granata, C. Cirillo, A. Vecchione, R. Bruzzese, C. Altucci and S. Amoruso, "Femtosecond laser surface irradiation of silicon in air: pulse repetition rate influence on crater features and surface texture", Optics and Laser Technology 126 (2020) 106073.

6. E. Allahyari, J. JJ Nivas, M. Valadan, R. Fittipaldi, A. Vecchione, L. Parlato, R. Bruzzese, C. Altucci and S. Amoruso, "Plume shielding effects in ultrafast laser surface texturing of silicon at high repetition rate in air", Applied Surface Science 488 (2019) 128–133.

7. Jijil JJ Nivas, Elaheh Allahyari, Filippo Cardano, Andrea Rubano, Rosalba Fittipaldi, Antonio Vecchione, Domenico Paparo, Lorenzo Marrucci, Riccardo Bruzzese, Salvatore Amoruso, "Vector vortex beams generated by q-plates as a versatile route to direct fs laser surface structuring", Applied Surface Science 471 (2019) 1028–1033

8. Elaheh Allahyari, Jijil JJ Nivas, Stefano L. Oscurato, Marcella Salvatore, Giovanni Ausanio, Antonio Vecchione, Rosalba Fittipaldi, Pasqualino Maddalena, Riccardo Bruzzese, Salvatore Amoruso, "Laser surface texturing of copper and variation of the wetting response with the laser pulse fluence", Applied Surface Science 470 (2019) 817–824

9. Jijil JJ Nivas, Elaheh Allahyari, Filippo Cardano, Andrea Rubano, Rosalba Fittipaldi, Antonio Vecchione, Domenico Paparo, Lorenzo Marrucci, Riccardo Bruzzese & Salvatore Amoruso, "Surface structures with unconventional patterns and shapes generated by femtosecond structured light fields", Scientific Reports (2018) 8:13613

10. E. Allahyari, J. JJ Nivas, F. Cardano, R. Bruzzese, R. Fittipaldi, L. Marrucci, D. Paparo, A. Rubano, A. Vecchione, and S. Amoruso, "Simple method for the characterization of intense Laguerre-Gauss vector vortex beams", Appl. Phys. Lett. 112, 211103 (2018)

11. Jijil JJ Nivas, Elaheh Allahyari, Felice Gesuele, Pasqualino Maddalena, Rosalba Fittipaldi, Antonio Vecchione, Riccardo Bruzzese, Salvatore Amoruso, "Influence of ambient pressure on surface structures generated by ultrashort laser pulse irradiation", Appl. Phys. A (2018) 124: 198

12. J. JJ Nivas, F. Gesuele, E. Allahyari, S. L. Oscurato, R. Fittipaldi, A. Vecchione, R. Bruzzese, and S. Amoruso, "Effects of ambient air pressure on surface structures produced by ultrashort laser pulse irradiation", Optics Letters, Vol. 42, Issue 14, pp. 2710-2713 (2017)